PHYSICAL MODELING OF DRUG DELIVERY IN SOLID TUMORS

by

Deniz Öztürk

B.S., Civil Engineering, Boğaziçi University, 2010

Submitted to the Institute for Graduate Studies in
Science and Engineering in partial fulfillment of
the requirements for the degree of
Master of Science

Graduate Program in Physics

Boğaziçi University

2013

To my loving mother.

ACKNOWLEDGEMENTS

I would like to thank my thesis supervisor, Burcin Ünlü. His vision, generosity and kindness have created the most productive and enjoyable research environment one could find. I also thank my professors, Osman Borekçi and Teoman Turgut, for the valuable, enjoyable discussions.

Thanks to my friends, Sirin Yonucu and Nehir Banaz, for their warm friendship and for the very inspiring discussions.

This research is supported in part by Marie Curie Reintegration Grant 268287, Boğaziçi University Research funding BAP 6033, BAP 7126 and TUBITAK Grant 112T253.

ABSTRACT

PHYSICAL MODELING OF DRUG DELIVERY IN SOLID TUMORS

Effective delivery of drugs is a major concern in cancer treatment. For a good treatment response, systemically administrated drugs must reach cancer cells in sufficient amounts, and not induce intolerable toxicity in healthy tissues. Toxic side-effects are the major dose-limiting factors in cancer treatment, and they often lead to the suspension of the treatment. Anti-cancer drugs that are effective in the laboratory models may lose potency when systemically administrated in humans. The reason is that, drug particles have to overcome several barriers during their journey to reach cancer cells. Impaired and heterogeneous blood supply, elevated interstitial pressure, and diffusional barriers in tumors, all limit the amount of drug that reaches the cancer cells. A good understanding of drug transport in tumors is necessary to improve the efficiency of drugs and design tumor-targeted delivery strategies. In this thesis, we study this problem through biophysically-founded mathematical models of drug delivery. We focus on blood flow and interstitial fluid flow in tumors, and study how they influence the delivery of drug particles. Interestingly, the hyper-permeability of tumor vessels, inhibits the delivery of drug particles. We study this seemingly paradoxical phenomenon, and also evaluate the potential benefits of the "vascular normalization" treatment, which aims to improve drug delivery by normalizing the tumor vessels. We also study how blood flow patterns are impaired in tumors, and how this influences the distribution of drug particles. In our simulations, instead of the conventional cytotoxic drugs, we focus on the delivery of nanoparticles as they form the basis of "intelligent" treatments in cancer.

ÖZET

TÜMÖRLERE İLAÇ İLETİMİNİN FİZİKSEL MODELLENMESİ

İlaç iletiminin verimliliği kanser tedavisinde büyük önem taşımaktadır. Sistemik tedavilerde, hastanın tedaviye iyi cevap vermesi ilaçların kanserli hücrelere yeterli konsantrasyonlarda ulaşmasına ve sağlıklı dokulardaki toksisitenin tolere edilebilir düzeyde kalmasına bağlıdır. Kanser tedavisinde başta gelen doz kısıtlayıcı faktörler toksik yan etkilerdir, ve çoğunlukla tedavinin kesilmesine sebep olmaktadır. Laboratuvar modellerinde etkili olan kanser ilaçları, sistemik olarak uygulandığında etkileri kaybolabilmektedir. Bunun sebebi, ilaç parçacıklarının, kanserli hücrelere ulaşana kadar bazı iletim bariyerlerine maruz kalmalarındandır. Kanser hücrelerine ulaşan ilaç miktarı, tümörlerde genellikle gözlenen düzensiz ve kısıtlanmış kan akışı, yüksek dokulararası sıvı basıncı, ve difüzyon engelleri gibi olgular tarafından kısıtlanır. Tümörlerde ilaç iletim süreçlerinin anlaşılması ilaç verimliliğini geliştirmek ve tümör-hedefli iletim stratejileri geliştirmek için gereklidir. Bu tezde, biyofiziksel esaslara dayanan matematiksel modeller geliştirerek bu problemi ele almaktayız. Tümörlerde kan akışı ve dokulararası sıvı akışına odaklanacağız, ve bunların ilaç iletimini nasıl etkilediğini inceleyeceğiz. İlginç bir şekilde, tümör damarlarının sızdırgan oluşu (damar duvarının aşırı geçirgenliği) ilaç iletimini kötü etkilemektedir. Tezde, bu paradokssal olguyu yakından inceleyeceğiz ve "damar normalleştirme" tedavisinin ilaç iletimini nasıl geliştirebileceğini teorik bir yaklaşımla göstereceğiz. Ayrıca tümörlerdeki kan akışı dağılımının nası bozulduğunu, ve bu bozukluğun ilaç dağılımını nasıl etkilediğini inceleyeceğiz. Yapacağımız simülasyonlarda geleneksel sitotoksik ilaçlardansa, "akıllı" kanser tedavilerinin temelini oluşturan nanoparçacıkları ele alacağız.

TABLE OF CONTENTS

LIST OF FIGURES

LIST OF TABLES

LIST OF SYMBOLS

$\mathbf{A}$	Matrix of finite difference coefficients for the blood-interstitial fluid transport problem
c	Solute concentration (mg/ml)
c_i	Drug concentration in the interstitium (mg/ml)
c_p	Drug concentration in the blood plasma (mg/ml)
C	Vessel wall circumference (mm)
d_{v}	Vessel inner diameter (μm)
d_{art}	Arteriole diameter (μm)
d_{cap}	Capillary diameter (μm)
d_{met}	Metarteriole diameter (μm)
d_{ven}	Venule diameter (μm)
f	Rate of fluid loss from the vessel to the interstitial space, measured per length of vessel (ml/mm·s)
J_{s}	Total solute flux across the vessel wall (mg/s)
j_{s}	Solute flux in tissue (mg/mm^2·s)
J_{v}	Total fluid flux across the vessel wall (ml/s)
K, K_{IF}	Hydraulic conductivity of the tissue (cm^2/mmHg·s)
K_i^{IF}	Hydraulic conductivity of the tissue on a mesh point (cm^2/mmHg·s)
K_{v}	Blood flow conductivity of the vessel (mm^4/mmHg·s)
K_s^{v}	Blood flow conductivity of the vessel on a mesh point (mm^4/mmHg·s)
L	Length density of intercellular clefts on the vessel wall (mm/mm^2)
$\mathrm{L}_{\mathrm{met}}$	Arteriolar-venular path length, i.e., metarteriole length.
$\mathrm{L}_{\mathrm{tumor}}$	Tumor dimension (mm)
L_{p}	Hydraulic conductivity of the blood vessel wall (cm/mmHg·s)
$L_{\mathrm{p,art}}$	Hydraulic conductivity of the arteriole wall (cm/mmHg·s)
$L_{\mathrm{p,cap}}$	Hydraulic conductivity of the capillary wall (cm/mmHg·s)

$L_{\mathrm{p,ven}}$	Hydraulic conductivity of the venule wall (cm/mmHg·s)
$L_{\mathrm{p,l}}$	Hydraulic conductivity of the lymph vessel wall (cm/mmHg·s)
M_r	Molecular weight (kDa)
P_{d}	Diffusional permeability of the vessel wall for a particular solute (cm/s)
P, $\mathrm{P_{IF}}$	Interstitial fluid pressure (mmHg)
$\mathrm{P}_i^{\mathrm{IF}}$	Interstitial fluid pressure on a mesh point (mmHg)
$\mathrm{P_l}$	Lymphatic pressure (mmHg)
$\mathrm{P_v}$	Vascular fluid pressure (mmHg)
$\mathrm{P}_s^{\mathrm{v}}$	Vascular fluid pressure on a mesh point (mmHg)
$\Delta\mathrm{P}$	Transvascular pressure difference, $\mathrm{P_v} - \mathrm{P_{IF}}$.
$\mathrm{P}_{\mathrm{art}}^{+}$	Upstream arterial blood pressure used in the discrete model (mmHg)
$\mathrm{P}_{\mathrm{art}}^{-}$	Downstream arterial blood pressure used in the discrete model (mmHg)
$\mathrm{P}_{\mathrm{ven}}^{+}$	Upstream venous blood pressure used in the discrete model (mmHg)
$\mathrm{P}_{\mathrm{ven}}^{-}$	Downstream venous blood pressure used in the discrete model (mmHg)
$\mathbf{q}_{\mathrm{IF}}$	Interstitial fluid flow (mm/s)
$\mathbf{q}_{\mathrm{v}}$	Blood flow rate (mm^3/s)
$\mathrm{r_f}$	Retardation factor, i.e., ratio of solute velocity to interstitial fluid velocity
r_{H}	Solute hydrodynamic radius
r_{s}	Solute radius
r_{p}	Pore radius
r_{v}	Vessel inner radius (μm)
S	Vessel surface area (mm^2)
W	Hindrance factor for transvascular convection
W	Intercellular cleft width (nm)
V	Tissue volume (mm^3)
Z	geometric resistance of the vascular network

Γ_{Fb}	Rate of fluid extravasation from blood vessels to interstitial space (ml/ml·s)
Γ_{Fl}	Rate of fluid drainage to the lymphatics (ml/ml·s)
θ_{B}	Mean vessel branching angle
λ_{c}	Tissue clearance rate of drug molecules
λ_{d}	Vascular diffusion rate of drug molecules
λ_{r}	Biological decay rate of drug molecules (1/s)
λ_{Fb}	Blood capillary filtration coefficient (cm/mmHg·s)
λ_{Fl}	Lymphatic filtration coefficient (cm/mmHg·s)
μ	Fluid viscosity
π_i	Oncotic pressure in the interstitial space
π_p	Oncotic pressure in the blood plasma
$\Delta\pi$	Oncotic pressure difference between the blood and the interstitium, $\pi_p - \pi_i$.
σ_{f}	Solvent drag reflection coefficient
σ, σ_{d}	Osmotic reflection coefficient
ϕ	Partition coefficient of the solute
ϕ_{F}	Volume fraction of the interstitial space

LIST OF ACRONYMS/ABBREVIATIONS

CD	Capillary density
CSA	Capillary surface area density
CW	Cranial window tumor model
DC	Dorsal chamber tumor model
ECM	Extracellular matrix
EPR	Enhanced permeability and retention
HA	Hyaluronic acid
IBD	Interbranch distance
ICD	Intercapillary distance
IFF	Interstitial fluid flow
IFP	Interstitial fluid pressure
IV	Intravenous
Mu89	A human melanoma cell line
MVD	Microvascular density
PBS	Phosphate buffered saline solution
RBC	Red blood cell
SEM	Scanning electron micrograph
U87	A human glioblastoma cell line

1. INTRODUCTION

1.1. Overview of the Thesis

In Chapter 1, we will review the problems encountered in delivery of drugs into solid tumors. We will focus on a particular problem among these, the barrier of elevated interstitial fluid pressure, for several reasons. First, the fact that the hyperpermeability of tumor vessels results in poor drug delivery is counter-intuitive, and we desired to study the mechanisms beyond this via mathematical modeling. Second, overcoming the barrier of elevated interstitial fluid pressure could dramatically increase the efficiency of novel cancer therapies based on nanoparticles, such as drug carrying liposomes, thermal nanospheres and active tumor targeting complexes. Third, handling this problem involves the calculation of blood flow inside the vessel network, coupled to the interstitial flow within the 3-dimensional tissue, which is by itself an interesting problem in terms of computational modeling.

In Chapter 2, we discuss the biophysical laws that govern the transport of fluid and drugs within the body. Following a brief discussion of the blood circulation within the body; the biophysics of blood flow, transvascular flow, interstitial flow and lymphatic drainage is described. In the second half of this chapter, we discuss in detail the biophysics of drug transport across the vessel walls and within the tissue. The drug delivery models presented in the chapters following are based on the biophysical principles laid out in this chapter.

Chapter 3 consists of a recent article from our research group. Here, we present a continuum model of drug delivery, and study how interstitial fluid flow and fluid pressure influence the tumor exposure and spatial distribution of blood-injected nanoparticles. In addition, we evaluate the influence of vascular normalization treatment on the delivery of nanoparticles.

Chapter 4 presents a discrete model of drug delivery, which is an improvement

on the continuum model presented in the Chapter 3. Here, in order to obtain a more accurate picture of drug delivery, blood flow within individual vessels is calculated in coupling with the 3-dimensional interstitial flow problem. Once the flow fields are calculated; we determine the tissue distribution of blood-borne nanoparticles by simulating their vascular, transvascular and interstitial transport, as well as lymphatic clearance and biological decay.

Chapter 5 presents some analyses conducted using the discrete model. Here we compare the transvascular convection rates on the individual capillaries in tumors and normal tissues. We finally study the blood flow patterns in tumors, and examine how these patterns influence the spatial distribution of drug particles. We conclude the thesis with some remarks.

1.2. Drug Delivery in Solid Tumors

Effective delivery of anti-cancer drugs in solid tumors is one of the major concerns in cancer treatment. Systemically-administrated cytotoxic[1] drugs affect healthy tissues as well as tumors, and therefore result in termination of the treatment, side-effects that decrease the quality of life, and sometimes death of the patient. Improving the efficiency of drug delivery, has been a major focus of cancer research besides development of new cancer drugs.

Following an intravenous bolus injection[2] (IV), drugs are distributed within the entire body via the circulatory system. They reach the tissues through capillaries, then cross the vessel wall (extravasation) and enter the intercellular space. The intercellular space, or "interstitium", is the space between the cells. The intercellular space is saturated with interstitial fluid and contains polysaccharides and fibrous proteins that form a matrix structure called the extracellular matrix (ECM). After extravasation, drug molecules travel through this biochemically active, heterogeneous and geometrically tortuous medium. In this stage, they either bind to the matrix proteins, become

[1] a substance that is toxic to cells, e.g., chemotherapy drugs such as doxurubicin, cisplatin, paclitaxel, etc.

[2] injection of a drug into a vein in a short period of time

biologically metabolized, drain into the lymph vessels to be removed from the tissue, or bind to or penetrate a cell surface to start its mechanism of action. The objective in drug delivery is increasing the amount of drug that reaches the cancer cells, and reducing the the amount that reaches the healthy tissues.

Several physiological barriers in the above process have been identified to result in ineffective drug delivery. Due to abnormal structure of tumor vessels, blood flow in tumors is impaired and heterogeneous [15], resulting in low-concentration and uneven drug distribution in the well vascularized regions. In addition, tumors have large avascular regions [6, 16, 17]. Compression of proliferating tumor cells might collapse blood vessels and further impair the blood supply into the central regions of tumors [15, 18]. In these cases, drug particles have to travel large distances by diffusion to reach the cells in poorly perfused regions (diffusion length barrier). This may be major problem for delivery of large molecular weight therapeutics because of their slow diffusion rates. Specifically, particles larger than 60 nm in diameter can not penetrate the ECM in many tumors [10]. Non-specific binding of drugs to interstitial matrix proteins further reduces their effective diffusion coefficient and the distance they could penetrate into the tissue beyond the vessel wall [15] (binding site barrier). Transport of drug particles in tumor interstitium will be discussed in more detail in Section 2.6.

1.2.1. The Barrier of Elevated Interstitial Fluid Pressure

In normal tissues, fluid continually leaks from blood vessels into the interstitium, and then drains into lymph vessels. This interstitial fluid flow (IFF) is driven by the pressure difference between the blood and lymph vessels, and controlled by the hydraulic resistance of the interstitium and the vessel walls, and osmotic pressure differences between the vessel, tissue and lymph compartments (See Figure 1.1 for an illustration, and Sections 2.3, 2.4 and 2.7 for an extensive discussion of IFF).

Due to the hyper-permeability (leakiness) of tumor vessels and the lack of functional lymphatics in tumors, interstitial fluid pressure (IFP) is elevated [2]. Typical values of IFP at the centers of various tumors are given in Table 1.2. Elevated IFP is

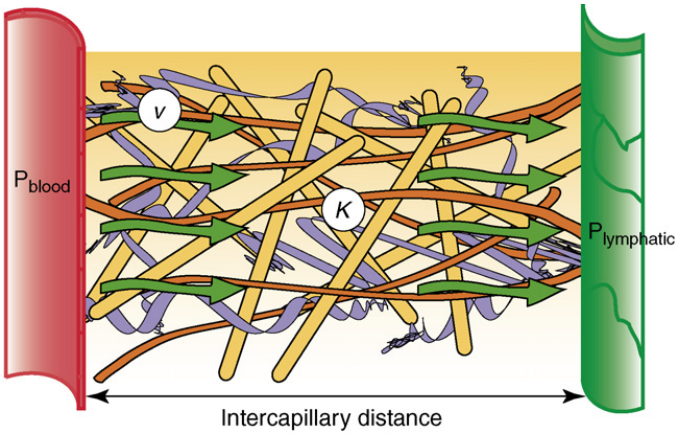

Figure 1.1. Interstitial flow is driven by the pressure difference between blood and lymph vessels ($P_{blood} - P_{lymphatic}$), and controlled by the hydraulic conductivity of the interstitium (K). Reprinted from Rutkowski and Swartz [1].

accompanied by the reduction of the hydrostatic pressure gradients across the vessel walls (transvascular pressure difference). This impairs the convective extravasation[3] of blood-borne drugs. Because IFP is uniformly elevated inside tumors, convective transport within the interstitial space is also reduced [2,19]. As their transport is dominated by convection, the large molecular weight agents (e.g., drug carrier liposomes, macromolecule-bound drugs, gold nanospheres, quantum dots) are especially prone to the barrier of elevated IFP. In addition, due to lack of functional lymphatics, the excess interstitial fluid exits the tumor through its boundary, to be drained by the surrounding functional lymph vessels [14]. This outward fluid flow (0.1–4.0 μm/s) may sweep the drug molecules towards the surrounding healthy tissue [13,20], and resists the diffusional transport of drugs from the outer vascular parts towards the central, avascular parts of tumors. In relation to the outward fluid flow, IFP sharply decreases to its normal tissue level (near zero) towards the tumor boundary (See Figure 1.2). Therefore transvascular pressure difference is not lacking near the tumor boundary, leading to rapid extravasation of interstitial fluid and drug molecules in this region [13, 14]. In conclusion, elevated interstitial fluid pressure results in heterogeneous delivery of blood-borne agents in solid tumors [21]. In Chapter 3, using a continuum model of drug delivery, we are going to investigate the influence of elevated IFP and IFF on the spatial distribution and tumor exposure of nanoparticles.

[3]extravasation: escaping from the vessel to the surrounding tissue

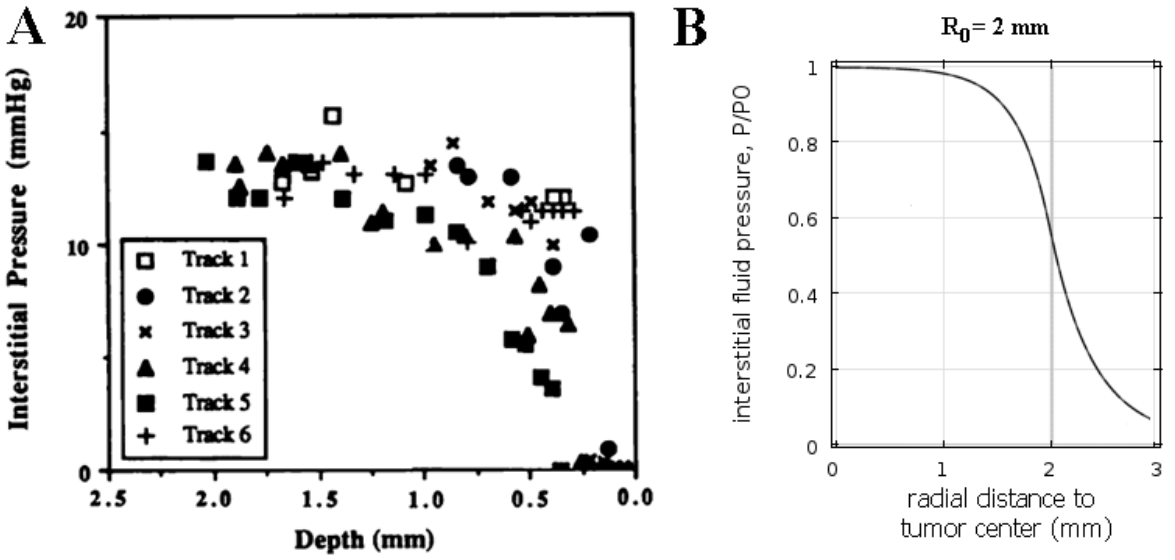

Figure 1.2. Interstitial fluid pressure (IFP) is elevated in solid tumors. A: IFP measurements by Boucher *et al.* [2] in a carcinoma. B: IFP (P) in a tumor of 2 mm radius, calculated using a continuum model of interstitial fluid flow (See Chapter 3).

In the recent years, treatment of tumors with several anti-angiogenic agents[4] was shown to reduce vascular permeability and IFP, and therefore restore transvascular pressure gradients, in a transient manner after administration [22–24]. See Table 1.1 for comparison of tumor central IFPs in various tumors before and after treatment with anti-angiogenic agents. In addition to these effects, vascular normalization treatment decreased vessel diameters and lengths, and increased blood flow and oxygenation in tumors [24–26]. Normalization therapy have been shown to improve the delivery of low molecular weight drugs, such as doxorubicin and cisplatin, in some types of cancer [22]. In a study by Tong *et al.*, vascular normalization decreased vascular permeability, restored transvascular gradients and convection, and increased the tumor penetration of albumin[5] [23]. In xenograft models, Dickson *et al.* have shown that treatment with bevacizumab decreases tumor microvessel density, tumor vascular permeability and IFP, whereas improves drug delivery, resulting in significantly greater tumor growth inhibition [24]. Using anti-angiogenic treatments in combination with chemotherapy have been approved for several types of cancers [22]. However, very few studies have been made on the effects of vascular normalization on delivery of large molecular weight agents, such as nanoparticles. In experiments by Chauhan *et al.*, transvascular flux of

[4] a substance that inhibits the growth of new blood vessels

[5] Albumin is a protein with a molecular weight of 68 kDa and a hydrodynamic radius of 3.5 nm.

Table 1.1. IFP values in tumors, before and after anti-angiogenic treatment. Data taken from Jain *et al.*, 2007 [14].

Tumor type, model, anti-angiogenic factor	**IFP** (mmHg)	**IFP after treatment** (mmHg)
rectal carcinoma, human, 5 mg/kg bevacizumab	15	4
rectal carcinoma, human, 10 mg/kg bevacizumab	16	5.4
spontaneous tumor, C3H mice, DC101	11.4	4.63
murine mammary carcinoma, DC101	6.13	3.10
human small cell lung carcinoma, xenograft, DC101	12.03	6.2
human glioblastoma, xenograft, DC101	11.52	5.95
human colon adenocarcinoma, xenograft, bevacizumab	13.5	3.5
human glioblastoma, xenograft, bevacizumab	12.0	3.0

12 nm nanoparticles were increased for several days after treatment with DC101 [9].

It is non-intuitive that decreasing vascular permeability improves drug delivery. Using mathematical models in Chapters 3 and 4, we will try to shed light on this apparent contradiction, and also try to answer whether and in what conditions vascular normalization could improve the delivery of nanoparticles. The advantages of using nanoparticles in cancer therapy will be discussed in the next section.

1.2.2. Nanoparticles in Cancer Treatment and the EPR Effect

The significantly higher permeability of the tumor vasculature could be taken advantage of, in targeting of tumors. Most of the organs feature capillaries that have pore cut-off sizes between 6-12 nm [27], which restrain the passage of larger molecules to healthy tissues. As tumor vessels have much larger pore cut-off sizes (100–780 nm), therapeutical agents that are larger than 12 nm extravasate selectively in tumors, causing lower toxicities and side effects. In addition, due to absence of functional lymphatics in tumors, they remain in the tissue for longer periods. Such selective accumulation of macromolecules in tumors is called the Enhanced Permeability and Retention (EPR) effect.

Traditional cytotoxic drugs such as doxorubicin, paclitaxel and cisplatin, being

Table 1.2. Measured values of IFP in healthy tissues and in the centers of various tumors. Reproduced from Jain *et al.*, 2007 [14].

Study, tissue	**N**	**IFP** (mmHg)	**Range** (mmHg)
Normal skin	5	0.4	-1.0 to 3.0
Normal breast	8	0.0	-0.5 to 3.0
Head and neck carcinomas	27	19.0	1.5 to 79.0
Cervical carcinomas	127	20.5	-2.8 to 94.0
Lung carcinomas	26	9.5	1.0 to 27.0
Metastatic melanomas	26	18.0	0.0 to 60.0
Breast carcinomas	21	23.7	4.0 to 53.0
Brain tumors	28	4.6	-0.5 to 15.0
Rectal carcinoma	8	15.3	12.1 to 15.8
Colorectal liver metastasis	8	21.0	6.0 to 45.0
Lymphomas	7	4.5	1.0 to 12.5
Renal cell carcinoma	1	38.0	-

small molecules (M_r: 0.3–0.5 kDa, $r_{\mathrm{H}} < 1$ nm) are distributed in the healthy as well as tumor tissues. In contrast, novel cancer therapies based on nanoparticles could take advantage of the EPR effect. Some examples to these agents are drug carrying liposomes, protein drug carriers, gold nanospheres and ultra-small quantum dots. In addition to passive tumor targeting via the EPR effect, nanoparticles could achieve active tumor targeting via the target-specific binding ligands attached to their surfaces (See Figure 1.3).

In relation to tumor vascular permeability, lymphatic clearance and blood circulation half-life, optimal nanoparticle sizes for maximal tumor accumulation are in the range of 10-100 nm [28, 29]. However, transport of particles in this size range is dominated by convection, and therefore elevated IFP is an important barrier for their delivery. Overcoming the elevated IFP might significantly improve the efficiency of these therapeuticals, which currently have limited potency. In Chapters 3 and 4, by developing models of drug delivery, we will study how blood flow, IFP and IFF influence the delivery of nanoparticles in solid tumors.

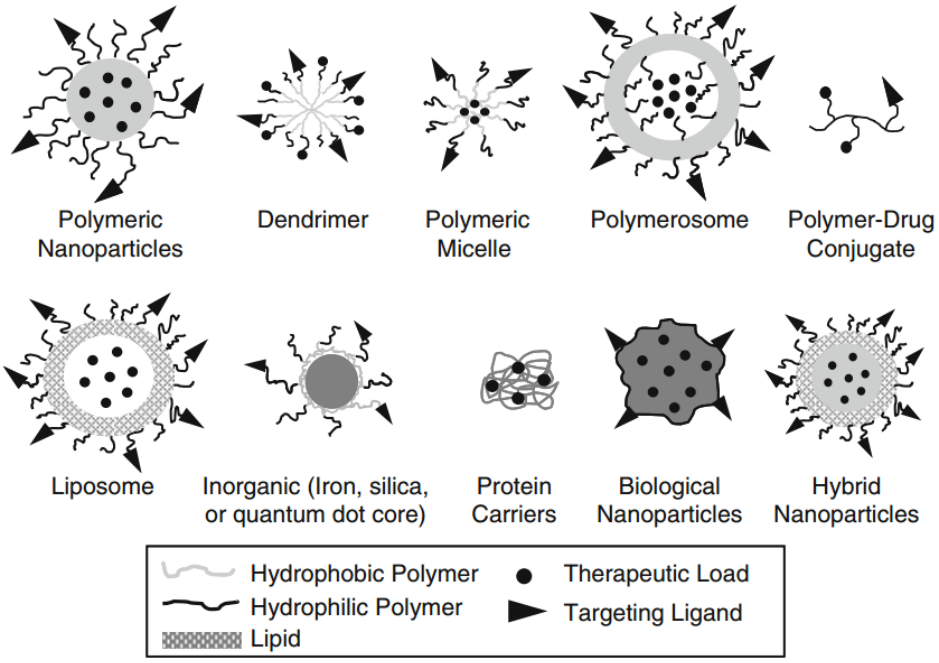

Figure 1.3. Nanoparticle platforms for drug delivery. Reprinted from Alexis *et al.* [3]

It must be noted that besides elevated IFP, heterogeneous vascularization (Section 2.1), heterogeneous tumor vascular permeability and pore size [10], and reduced interstitial diffusion rates due to particle size (See Section 2.6) lead to heterogeneous distribution of nanoparticles [10, 28, 30].

2. BIOPHYSICS OF DRUG DELIVERY

2.1. Vascular Network Structure and Tumor Angiogenesis

Circulatory system has evolved into an organized network of branching vessels that efficiently delivers oxygen, nutrients and removes wastes and CO_2 to and from the tissues in whole body. Within this network, vessels are classified as arteries, arterioles, capillaries, post-capillary venules, venules and veins, respectively, in the direction of blood flow. Capillaries are the tiniest of these vessels, and they are responsible for mass exchange between blood and tissues. 10 to 40 billion capillaries penetrate and populate the tissues, with an estimated total exchange surface area of 600 m^2 [31]. Figure 2.1 displays the organization of the circulatory system. Vessels possess different mechanical, hydraulic and permeability properties according to their function within the specific tissue, or within the circulatory system. For instance, arteries are covered with elastic muscle cells. During systole[1], they expand in response to the increasing blood pressure and dissipate the pulse, providing a non-pulsating, steady blood flow to capillaries. Capillaries of the intestines, renal glomerulus and endocrine glands, for instance, have highly-permeable, fenestrated walls that allow easy exchange of nutrients, hormones and water, which are necessary for the functions of these tissues.

Structure of the capillary wall regulates the rate of water and solute exchange, as will be discussed in detail in Sections 2.3 and 2.5. The capillary wall consists of a layer of endothelial cells, covered with the basement membrane on the outer side, and the glycocalyx[2] on the luminal side, which acts as a molecular sieve in transvascular transport and limits the passage of large molecules. There are three types of capillaries: continuous, fenestrated, and sinusoidal (See Figure 2.2). Endothelial cells of the continuous capillaries are tightly connected to each other via the tight junctions, with a 1-20 nm gap width [27,43], forming an uninterrupted vascular wall. Endothelial cells of fenestrated capillaries have fenestrations (i.e., pores that are 60-80 nm in diam-

[1] contraction of the left ventricle that drives the blood circulation

[2] a layer of heparan sulfate proteoglycans and hyaluronan secreted by and coating endothelial cells [1].

Table 2.1. Comparison of capillary densities in several tissues.

Tissue, study	**CD** (mm/mm^3)	**CSA or MVD** (cm^2/cm^3)	**ICD** (μm)	**Vessel diameter** (μm)
rat cerebral cortex				
healthy tissue [32]	160–810			
healthy tissue [33]		294–308	34–24	5
glioma [33]		225–250		15–20
Konerding *et al.* [6]				
HEC-1B[a]			76	17
CaX[b]			112	24
SAS[c]			181	24
CaNT[b]			214	32
estimated from [34]				
mammary carcinoma		120-260		
mammary adenocarcinoma		150-570		
hepatoma		50-200		
human healthy tissues				
skeletal muscle [35]	459–1468			
skeletal muscle [36]	161–426			
gut, muscle [6]			63, 35	8, 9
human tumors				
various types [14, 37, 38]		50–250		
mammary adenocarcinoma [17]			49.4±9.8	10.3±1.4
lung carcinoma [39]	202[d], 49[e]		72[d], 155[e]	
melanoma [40]	32–80	16–38		
mammary adenocarcinoma [41]	190–1340	140–460		
cervix uteri carcinoma [42]			304±9.8	

[a] human endometrial adenocarcinoma
[b] murine carcinoma
[c] slow growing murine carcinoma
[d] tumor periphery
[e] tumor center

eter and covered with the glycocalyx) on them that serve as transvascular transport channels. The endothelial cell lining and the basement membrane cover of sinusoidal capillaries are discontinuous. Gaps between the endothelial cells of sinusoidal capillaries are 100-1000 nm, which is permeable to water, large molecules, and even to some cells [44]. In tumor vessels, the structure of capillary walls is altered towards fenestrated or sinusoidal phenotypes.

The vessel network penetrates and distributes within tissues at the microcirculatory level, i.e., via arterioles, capillaries, post-venules and venules. Arterioles are small arteries with a diameter between 10 μm and 0.3 mm. Capillaries are the main exchange vessels, with a diameter of 5-10 μm, and they form networks between arterioles and post-capillary venules (See Figure 2.1). Within the capillary network there are vessels of 10–20 μm diameter that directly link arterioles and venules, called metarterioles. Acting as "preference channels", metarterioles can contract and expand to regulate the blood flow into the capillaries [45]. Exchange of water, nutrients, drugs and cellular waste products between the blood and tissue predominantly occur through the capillaries, and at a lower rate, through the post-capillary venules. Level of vascularization of a tissue could be characterized by quantities such as capillary density (CD), capillary surface area density (CSA), microvascular density (MVD)[3], and intercapillary distance (ICD). See Table 2.1 for measured values of CD, CSA or MVD , ICD and vessel diameter in several types of tissues.

2.1.1. Tumor Angiogenesis

Angiogenesis is the formation of new blood vessels from existing vasculature. Angiogenesis is triggered and governed predominantly by the members of the vascular endothelial growth factor (VEGF) and angiopoietin (Ang) family, which are produced by the cells in the avascular region. Angiogenic factors diffuse within the tissue and initiate the growth of new vessels from the neighboring vasculature. Directionality of vessel growth is controlled by the angiogenic factor gradients. In healthy tissues, ves-

[3]vessel surface area density (mm^2/mm^3) measured over all microvessels, i.e. arterioles, capillaries, venules.

Table 2.2. Quantitative information on the topology of vasculatures in several tissues.

Study, tissue type	**Inter-vessel distance** (μm)	**Inter-branch distance** (μm)	**Branching angle** (°)	**Vessel diameter** (μm)	**Tortuosity** (rad/μm)[a]
Lang *et al.* [46]					
healthy tissue	50	20	116±29	8.0	0.18
murine colon carcinoma	53	17	117±28	3.9	0.24
Konerding *et al.* [6]					
HEC-1B[b]	76±12	82±13	80±12	18±4.9	
CaX[c]	112±14	70±12	68±10	24±6.7	
SAS[d]	181±19	125±16	67±11	24±6.4	
CaNT[c]	214±19	148±16	68±10	32±7.4	
Folarin *et al.* [47][e]					
healthy colon epithelium	98±1.3	45±1.7	87±9.5	13±1.7	0.28
colon adenocarcinoma (tumor periphery)	46±1.7	43±1.7	72±2.7	18±1.4	0.44[f]
colon adenocarcinoma (tumor center)	135±2	100±2	76±4.3	23±2.2	0.44[f]
Ackermann *et al.* [48]					
Ewing's sarcoma	92±30	94±27		40±12	
Less *et al.* [17]					
mammary adenocarcinoma	45±9.8	1125±200, 80, 67±34, 180, 1020±780[g]		150±30, 20, 10±1.4, 33, 400±100[g]	

[a] In SOAM metric: integral of vessel path curvature divided by vessel length
[b] human endometrial adenocarcinoma
[c] murine carcinoma
[d] slow growing murine carcinoma
[e] surgically removed human tissue
[f] whole tumor average (periphery and center)
[g] measurements for: arterioles, higher order arterioles, capillaries, post-capillary venules, venules

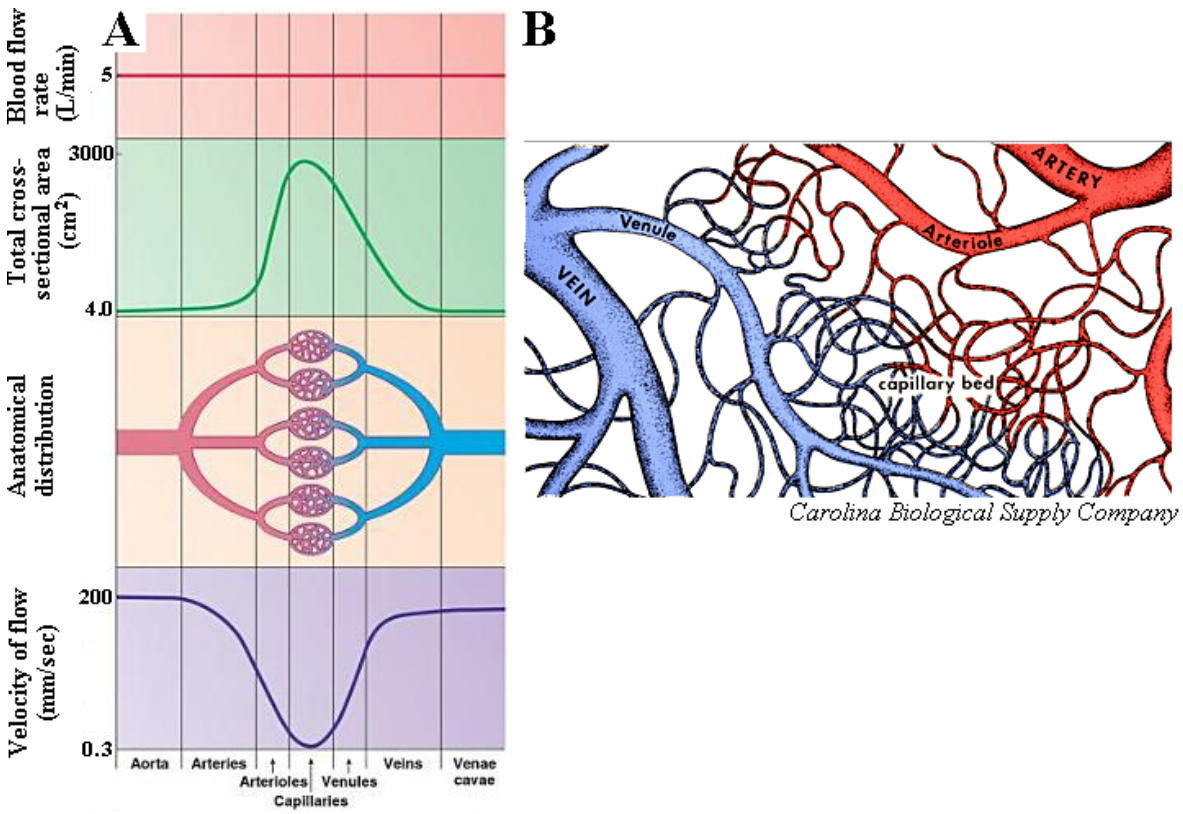

Figure 2.1. The organization of the circulatory system (A) and the microcirculatory network. (B): arterioles, capillaries, and post-capillary venules.

sel growth is toward the angiogenic source in an organized manner. Angiogenesis is predominantly observed in healthy physiological processes such as wound healing and embryogenesis. Angiogenesis in health tissues occurs in an orchestrated and tightly-controlled manner, unlike in tumors.

Until a tumor spheroid reaches a size of 1-2 mm (10^5–10^6cells), it depends on the supply of oxygen and nutrients from the preexisting capillaries of the host tissue [49]. Beyond this size, due to metabolic stress (i.e., low oxygen concentration, low glucose concentration, increased acidity) tumor cells initiate angiogenesis. The newly formed tumor vasculature (tumor neovasculature) promotes further tumor growth and cancer cell metastasis to distant organs, but it is not effective in meeting the metabolic demand of the tumor, as discussed below. Furthermore, compression of the tumor cells collapses some portions of the vasculature, modifying or regionally shutting down the tumor blood supply. In consequence, triggers of angiogenesis remain and VEGF concentration is chronically elevated in tumors [50]. VEGF gradients are random or

lacking in tumors, resulting in loss of directionality and organization in vessel growth [51]. Besides inducing angiogenesis, VEGF increases capillary wall permeability by several factors [52] by enlarging the pores on, and loosening the junctions between the endothelial cells that line the capillary wall [53–55].

Tumor neovasculature significantly differs from healthy vasculature in function and structure. Tumor vessels are tortuous, dilated and saccular [40]. Due to increased vessel tortuosity and vessel length, geometric resistance of the vasculature could be 1-2 orders of magnitude higher [56], and blood flow velocity an order of magnitude smaller than in normal tissues [7]. Microvessel diameters are variable within a tumor, and they are significantly larger than those of the host tissue capillaries (7–30 μm [6, 7, 33] vs. 5–10 μm). The vessel network may also have dead-ends (sprouts) and loops, which are inefficient structures for blood circulation. Intercapillary distances in tumors is generally larger than in normal tissues [40], and microvessel density is higher in some regions of the tumor, and lower in others [50]. See Figure 2.3 for variations in tumor microvessel density, avascular regions (star), dead-ends (circles), and changes in vessel diameter (arrows) in tumor vasculatures. Tumor vessels are leaky due to their abnormal capillary wall structure. Tumor capillaries have 40-60 nm fenestrations [10, 57] and compared to normal capillaries they have loose interendothelial junctions. Interendothelial gaps in tumor vessels could be 100-780 nm [10, 58] and up to a few micrometers [59] in contrast to 1-20 nm [27, 43] in normal continuous and fenestrated capillaries and 150 nm in normal sinusoidal capillaries [60]. As discussed in Section 1.2, a direct consequence of hyper-permeable tumor vasculature is elevated interstitial fluid pressure. Altogether, abnormal properties of the tumor vasculature results in hindered and heterogeneous blood flow, large hypoxic regions and inefficient drug delivery – all of which are undesired conditions for treatment of tumors [18, 50].

2.1.2. The Architecture of Tumor Vascular Networks

Understanding the topology of tumor vessel networks is important in developing drug delivery strategies, since it determines the spatial distribution of blood flow, and in turn, of nutrient and drug supply. Tumor vascular networks exhibit disorganized

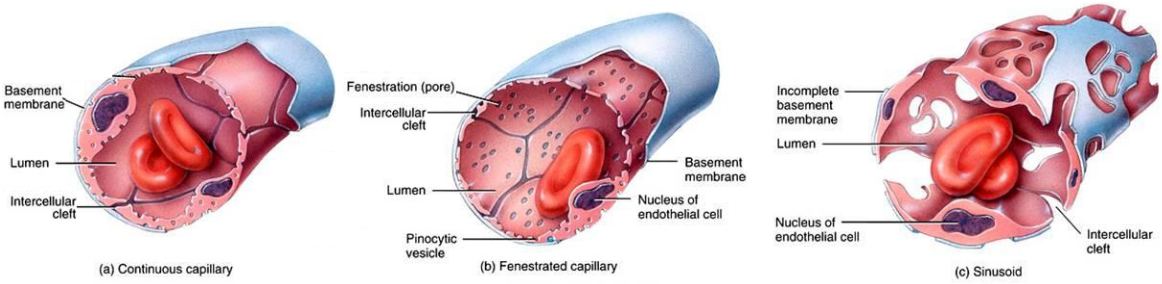

Figure 2.2. Wall structure of (A) continuous, (B) fenestrated and (C) sinusoidal capillaries. Reproduced from Martini *et al.* [4].

branching patterns and they lack the hierarchy found in healthy vascular networks (e.g., decreasing vessel diameter with increasing vessel order). One consequence of this is the loss of the correlation between vessel diameter and blood flow velocity in tumor vessels (See Figure 2.4). Because angiogenic factor gradients in tumors are random or lacking, in some regions within tumors, vessels grow disorderly in random directions [51] (See Figure 2.3d). Vascular casts of several tumors examined by Less *et al.* [17] displayed centrally oriented arterioles peripherally branching into surrounding smaller arterioles and capillaries, and a network large draining venules (200-300 μm) mainly on the periphery of the tumor. However, vascular architecture and organization greatly varies between individual tumors, as well as within each tumor. Generally, organization and density of the vascular network of the tumor periphery significantly differs from that of the center [5, 6, 51]. The peripheral region of the tumor vasculature is termed the "vascular envelope" and often has a higher vessel density.

Quantitative data on the vascular network topology, such as vessel diameter, diameter variability, tortuosity, branching angle and interbraching distance (i.e., vessel segment length), have been of interest, and were shown to be tumor type-specific by Konerding *et al.* for several tumors [5,6]. One method for obtaining these parameters is by infusing a casting polymer into the tumor vasculature, eroding the biological tissue to reveal the polymerized casting, and scanning the cast microstructure via optical microscopy [17], electron microscopy (SEM) [5, 6, 48] or micro-computed tomography (μCT) [46,47]. Using μCT data three-dimensional images and vector-based representations of the vascular network could be constructed. Quantitative information obtained using this technique on several healthy and tumor tissues are listed in Table 2.2. Such

quantitative information could be used in generation virtual tumor vasculature in computer models (i.e., discrete models of angiogenesis).

2.2. Blood Flow

As the heart contracts to drive blood flow, blood pressure in the left ventricule and aorta increases to 120 mmHg. During contraction, blood pressure is maximum in this region, and decreases within the circulatory system in the direction of blood flow and towards veins and the right ventricule, where it maintains a value between 10-20 mmHg. Blood circulation is driven by this pressure difference between the arterial and venal ends, against the viscous drag on the vascular walls. Near the arterial end of the circulation, blood pressure pulsates due to contractions of the heart with an amplitude of 30-40 mmHg. However, these pulses are damped by volumetric expansion of the elastic arteries, and do not reach the microcirculatory level. As a result, blood pressure in capillaries is non-pulsating and blood flow is almost steady [61]. Assuming that blood flow is laminar, Poiseuille's Law could be used to relate blood flow rate, q_{v} (ml/s), and pressure gradient along the vessel, $\nabla \mathrm{P}$:

$$q_{\mathrm{v}} = -\frac{\pi d_{\mathrm{v}}^4}{128\mu} \nabla \mathrm{P}_{\mathrm{v}}, \tag{2.1}$$

where d_{v} is the vessel diameter, μ is the viscosity, and P_{v} is the blood pressure. A homologous relation can be written for a network of blood vessels:

$$q_{\mathrm{v}} = \frac{\Delta \mathrm{P}_{\mathrm{v}}}{\mu Z}, \tag{2.2}$$

where $\Delta \mathrm{P}_{\mathrm{v}}$ is the pressure difference between the arterial and venous ends of the network, and Z is the geometric resistance of the vascular network which is a function of both its global topology and the local variations in vessel diameters. Z could be directly measured in tissue-isolated tumors by perfusing the vasculature at constant

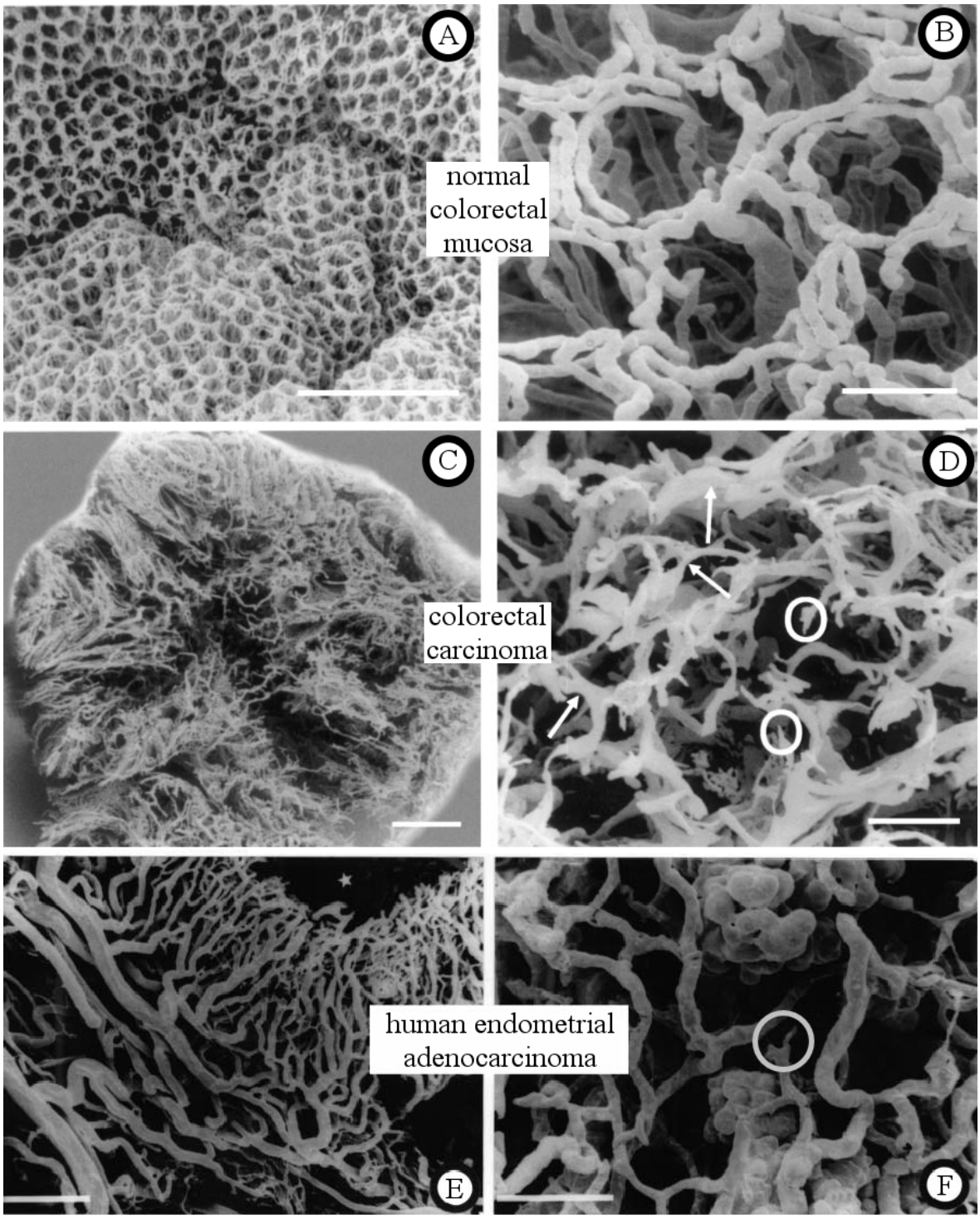

Figure 2.3. SEMs of corrosion casts of the vascular networks in normal and tumor tissues. Right: high-power images. Bars: 1 mm (A, C), 500 μm (E), 100 μm (B, D, F). Images A to D: Konerding *et al.*, 2001 [5]. Images E, F: Konerding *et al.*, 1999 [6].

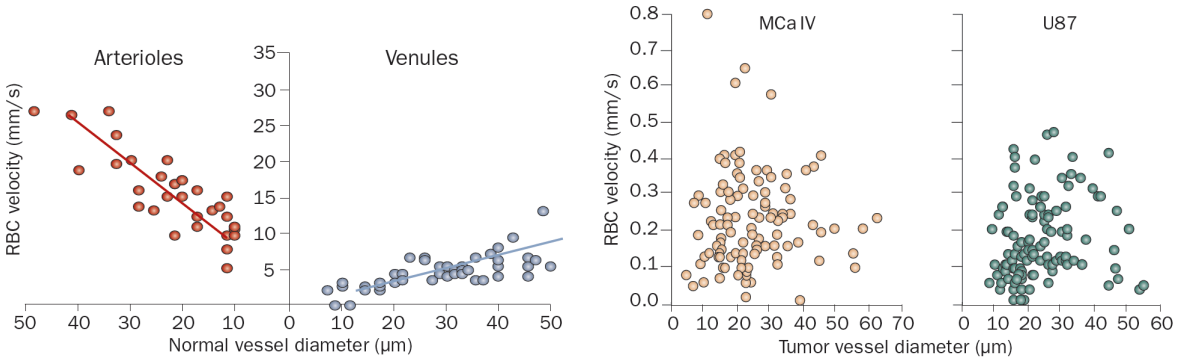

Figure 2.4. Blood flow velocity as a function of vessel diameter in normal tissues (left) and tumors (right). RBC: red blood cell. Reprinted from Yuan *et al.* [7]

arterio-venous pressure difference and measuring the flow rate [56]. In tumor vasculature, geometric resistance could be higher [56], and the mean blood flow velocity lower [7] by 1-2 orders of magnitude compared to normal vasculature (See Figure 2.4).

Having enlarged diameters compared to normal capillaries, tumor capillaries must have a lower local flow resistance according to Equation 2.1. Therefore, global topology of the tumor vascular network must account for the increased geometric resistance (Z). For instance, tumor vessels are tortuous compared to normal vessels (Table 2.2), therefore on average blood flow path lengths should be larger, resulting in greater flow resistance. In a study by Gessner *et al.* [62], the average distance metric (DM)[4] of vessels was 25% higher in tumors than in normal tissues. Second, presence of avascular regions implies that effective number of parallel pathways is smaller in tumors. Finally, diameter fluctuations along individual vessels [6] and between adjoining vessel segments [17,47], should cause head losses due to rapid streamline contraction/expansion, further contributing to the geometric resistance of tumor vasculatures.

It has been observed that besides decreasing IFP, vascular normalization treatment using anti-angiogenic factors decreases vessel diameter, length and tortuosity, and increases blood flow, oxygenation, and extravasation rate of macromolecules in tumors [22–24].

[4]the ratio of the actual path length to the linear distance between the end points of a vessel segment

2.3. Transvascular Fluid Flow

Transport of fluid across the vessel wall may occur through intercellular clefts (the slit-like channels between the endothelial cells) and fenestrations (cylindrical openings within endothelial cells). See Figures 2.2 and 2.5 for illustrations of these vascular structures. The inner surface of the endothelial cell lining is covered with a protein matrix called glycocalyx, which further resists fluid extravasation at the cleft entrance [63], and acts as a molecular filter [64]. Transvascular transport of fluids is mainly passive, and it is driven by the pressure difference across the vessel wall [65]. To relate the transvascular pressure gradient to fluid flux, a coefficient of hydraulic conductivity (L_{p}) could be assigned to the vessel wall which is a function of the distribution and shapes of the fluid channels. Then, transvascular flow is described using $J_{\mathrm{v}} = L_{\mathrm{p}}\mathrm{S}\Delta\mathrm{P}$, where S is the vessel exchange surface area. L_{p} has been measured for the capillaries of different tissues. Measurements of capillary filtration coefficients ($L_{\mathrm{p}}\frac{\mathrm{S}}{\mathrm{V}}$, ml/mmHg/100 gr/s) may provide estimates for L_{p} if vessel surface density ($\frac{\mathrm{S}}{\mathrm{V}}$) is known. Table 2.3 lists some measured and estimated values of hydraulic conductivity for vessels that belong to different types of tissues. According to their permeability properties, capillaries are classified as continuous, fenestrated and sinusoid (See Figure 2.2). Continuous capillaries have uninterrupted endothelia, and transvascular transport is confined to the tight intercellular clefts. Widths of these intercellular clefts (gaps between the endothelial cell) is typically 1-3 nm, and transport pathway of fluid within clefts is restricted by the tight functional strands that connect the adjacent endothelial cells [43] (See Figure 2.5). In contrast, fenestrated and sinusoid capillaries are characterized with a high hydraulic conductivity ($L_{\mathrm{p}} > 10^{-6}$ cm/mmHg/s). In fenestrated capillaries, transport of water and solutes is mainly through the endothelial fenestrations [65], and they are permeable only to small molecules such as water and ions. Sinusoidal capillaries have large gaps between the endothelial cells (100-1000 nm), which are permeable to water, large molecules, and even to some cells [44].

Tumor vessels have dilated fenestrations and loose interendothelial junctions [10, 66]. As a result, they have a higher hydraulic conductivity and molecular permeability, compared to normal vessels. For instance, on tissue isolated tumors, Sevick

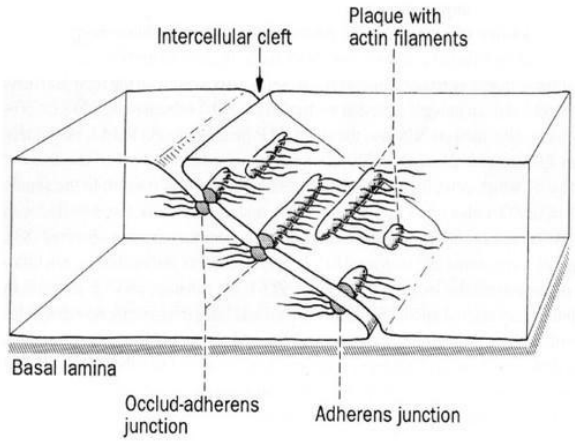

Figure 2.5. Illustration of an intercellular cleft and tight junctions between adjacent endothelial cells. Reprinted from [8].

and Jain [67] have measured capillary filtration coefficients ($L_{\mathrm{p}}\frac{\mathrm{S}}{\mathrm{V}}$) to be 10 to 1000 times higher than normal tissues. As discussed in Section 2.1.1, this leakiness of the tumor vasculature, as well as its other structural abnormalities, is attributed to the overexpression of angiogenic factors [22]. In experiments by Bates and Curry [52], exposure to VEGF increased the hydraulic conductivity of the vessel wall by 8-fold. It is well accepted that VEGF increases vascular diffusional permeability and hydraulic conductivity by loosening the interendothelial junctions and inducing formation of endothelial fenestrations [27, 53–55].

Transport properties of the vessel wall could be accounted for by modeling the fenestrations as cylindrical pores and the intercellular clefts as rectangular slits [65]. Assuming that fluid flow through these flow channels is laminar, one could calculate L_{p} from Poiseuille's law. The contribution to L_{p} by cylindrical pores of a certain size is:

$$L_{\mathrm{p},i} = \frac{n_i \pi r_i^4}{8\mu\Delta x}, \tag{2.3}$$

where n_i is the population density (number per area) of fenestrations which have the radius r_i, μ is the fluid viscosity, and Δx is the pore length. Hydraulic conductivity

due to rectangular slits that represent intercellular clefts, is:

$$L_{\mathrm{p},i} = \frac{\mathrm{L}_i \mathrm{f}_i \mathrm{W}_i^3}{12\mu\Delta x}, \tag{2.4}$$

where L_i is the length density ($\mathrm{cm/cm^2}$) of the intercellular clefts with width W_i, Δx is the intercellular cleft depth, and f_i is the fraction of the cleft length that is open for fluid transport (i.e. fraction of discontinuities on the tight junctions, see Figure 2.5). Total L_p of the vessel wall is calculated by summing the contributions of individual pathways $L_{\mathrm{p},i}$ (i.e. contributions from intercellular clefts and fenestrations of different sizes) weighted by the area of the pathway [65]. It must be noted that the relation (2.4) do not take into account the two dimensional expansion of the fluid pathway in the cleft space, as the fluid passes between the consecutive discontinuities on tight junctions. Therefore Equation 2.4 overestimates the total viscous drag (and underestimates L_p). By solving a model of 2-dimensional flow within the cleft obstructed a discontinuous junction, Philips *et al.* [68] calculated the correction factor due to spreading of the fluid to be 2.7 for a typical intercellular cleft.

Another essential regulator of transvascular flow is the oncotic pressure of the blood plasma. High protein content of the plasma creates an osmotic back-flow according to Starling's law [77]:

$$J_\mathrm{v} = L_\mathrm{p}\mathrm{S}\left(\Delta\mathrm{P} - \sigma_\mathrm{d}\Delta\pi\right), \tag{2.5}$$

where σ_d is the osmotic reflection coefficient, and $\Delta\pi$ is the osmotic pressure difference between the blood serum and interstitium. The osmotic pressure of a solute, π, is related to its concentration, and defined as the hydrostatic pressure difference needed to be applied in order to stop the fluid flow across a semi-permeable membrane. σ_d depends on the relative sizes of solutes and membrane pores, and measures how effectively the membrane maintains the solute concentration difference. $\sigma_\mathrm{d} = 0$ and 1 represents

Table 2.3. Hydraulic conductivities of vessels found in different types of tissues.

Vessel location and type	**Hydraulic conductivity**, L_{p} ($\times 10^{-8}$ cm/mmHg-s)	**Ref.**
mammary adenocarcinoma	60-230[a]	[67]
mammary adenocarcinoma	186	[14]
frog mesenteric capillaries(treated with VEGF)	265	[52]
frog mesenteric capillaries	34	[52]
rat skeletal muscle capillaries	3.6	[69]
frog muscle capillaries	9.8	[70]
frog mesenteric capillaries	34	[71]
cat hindlimb capillaries	1.3	[72]
dog lung capillaries	2.6	[72]
dog small intestine capillaries	153	[72]
rat mesentary post-capillary venules	10.7	[73]
rat mesentary venules	32.6	[74]
dog lung venules	39.4	[75]
rat brain cortex arterioles	1.7 ± 0.57	[76]

[a] estimated from the measurements of $L_{\mathrm{p}}\frac{\mathrm{S}}{\mathrm{V}}$ (0.8–2.8 cm^3/mmHg/100gr/min) by assuming $\frac{\mathrm{S}}{\mathrm{V}} = 200$ cm^{-1}.

a membrane completely permeable, and impermeable to solutes, respectively.

In healthy tissues, the oncotic pressure contribution ($\sigma_{\mathrm{d}}\Delta\pi$) is typically 10-28 mmHg [14]. Albumin ($M_r = 65$ kDa, $r_{\mathrm{H}} = 3.5$ nm), being the most abundant protein in the plasma, constitutes approximately 80% of the oncotic pressure contribution. Therefore the impermeability of the capillary wall to albumin is essential in maintaining the osmotic back-flow. Osmotic reflection coefficient for albumin is between 0.8 and 1 in most tissues. In tumors, capillary pore sizes may be as large as a few micrometers [59]. This results in $\sigma_{\mathrm{d}} \approx 0$ and the osmotic back-flow is lost.

Starling's law could be generalized to account for the flow of multiple-solute solutions across heteroporous membranes [77], as:

$$J_{\mathrm{v}} = \sum_{i=1}^{m} J_{\mathrm{v},i} = \sum_{i=1}^{m} L_{\mathrm{p},i}\mathrm{S}\left(\Delta\mathrm{P} - \sum_{j=1}^{n}\sigma_{i,j}\Delta\pi_j\right), \tag{2.6}$$

where m denotes the number of different pore types, $J_{\mathrm{v},i}$ is the total flux across the pores of type i, $L_{\mathrm{p},i}$ is the fractional contribution to the hydraulic conductivity by the water channels of type i (either pores, or slits of different size), n is the number of solutes, $\Delta\pi_j$ is the oncotic pressure difference of the solute j, and $\sigma_{i,j}$ is the oncotic reflection coefficient associated with the solute j and the channel size i.

2.4. Interstitial Fluid Flow

To estimate the velocity of interstitial fluid within the tissue, Darcy's law could be used:

$$\mathbf{q}_{\mathrm{IF}} = -K\boldsymbol{\nabla}P. \tag{2.7}$$

Here, K is the Darcy coefficient, or the tissue hydraulic conductivity, and q_{IF} is the interstitial fluid flux (IFF, $\mathrm{mm}^3/\mathrm{mm}^2{\cdot}\mathrm{s}$). The actual velocity of the fluid, (i.e., velocity of the fluid seeping through the solid phase) is related to the IFF via $v_{\mathrm{IF}} = \mathbf{q}_{\mathrm{IF}}/\phi_{\mathrm{F}}$, where ϕ_{F} is the volume fraction of the interstitial fluid. Darcy's law is valid for viscous flow ($\mathrm{Re} \ll 1$) through porous media in general, and it has been used to describe groundwater flow (through gravel, sand and soils) for many decades.

Hydraulic conductivity varies greatly in different types of tissues. For instance, lung tissue is a several orders of magnitude more conductive than cartilage (5000 vs. 0.1 $\mu\mathrm{m}^2/\mathrm{mmHg}{\cdot}\mathrm{s}$) [14]. K also depends on the patophysiology of the tissue: tumors are generally more permeable to fluids, compared to normal tissues of same type [78]. For instance, in *in vitro* experiments by Swabb *et al.*, K was measured as five times higher in rat hepatoma than in normal subcutaneous tissue [79]. Table 2.4 lists some measured values of K for different types of tissues.

K is measured *in vitro* in perfusion chambers [79,80] or by confined compression tests [81], and *in vivo* via infusion through a needle [79,82,83]. Experimental techniques for *in vivo*, non-invasive, imaging-based measurements of hydraulic conductivity are

Table 2.4. Hydraulic conductivities of different types of tissues.

Tissue	**Hydraulic conductivity**, K (μm^2/mmHg-s)	**Ref.**
subcutaneous tissue	0.85	[79][a]
rat hepatoma 5123	4.13	[79][a]
subcutaneous tissue	0.59	[79][b]
hepatoma	0.75	[79][b]
colon adenocarcinoma	17–23	[86][b]
cartilage	1–0.1	[87][a]
mesentery, skin	1000–100	[14][a]
lung	5000	[14][a]
MCaIV	248	[78][c]
LS174T	45	[78][c]
U87	65	[78][c]
HSTS 26T	9.2	[78][c]

[a] perfusion chamber, *in vitro*
[b] intratumoral infusion, *in vivo*
[c] confined compression test, *in vitro*

still being established. Examples for such advances are works of Périé *et al.* [84] that used quantitative MRI data, and of Rutkowski and Swartz [85] that involves infusion of tracer molecules. Calibrating tissue- and patient-specific model parameters through *in-vivo*, non-invasive measurements is especially desired in computational medicine to design and guide individualized treatments.

Hydraulic conductivity depends on the viscosity of the interstitial fluid, and chemical and geometric structure of the tissue. K is inversely proportional to fluid viscosity, μ, and could be written as $K = \frac{k}{\mu}$, where the coefficient k depends solely on the geometric structure of the tissue. Deforming effects such as compression, expansion, and excessive perfusion/hydration is known to influence k, by modifying the geometry of water channels within the tissue. In an ideally homogeneous and isotropic medium, tissue hydraulic conductivity and porosity (ϵ) is related by an exponential law as: $k = k_0 \exp(\epsilon - \epsilon_0)$ [78], where the subscript 0 denotes initial values.

Chemical structure of the ECM also influences the hydraulic conductivity of the tissue. The ECM consists of a network of collagen and elastin protein fibers, and a

high-surface-area, negatively charged polysaccharide network of hyaluronic acid (HA) and glycosaminoglycans (GAG). The collagen matrix gives structural support to the ECM, while the GAGs attached to it, govern the tissue permeability for fluid and macromolecules by affecting the fluid pathways and by their surface electric charge. It is well accepted that a denser collagen matrix, as long as it has stable networks of HAs and GAGs attached, has lower water permeability [78,88,89]. In accordance, treating the ECM with matrix-degrading enzymes effectively reduces the tissue hydraulic permeability [78]. In addition to controlling fluid permeability, structure of the ECM also influences penetration of solutes (See Section 2.6).

2.5. Extravasation of Drugs

Once drug molecules reach the capillaries, they may cross the capillary wall mainly via diffusion and convection, and at a much slower rate, by transcytosis. In this section, we discuss the mathematical relations that describe the transvascular transport of drugs via diffusion and convection.

2.5.1. Convective Transport Across the Vessel Wall

Rate of convective transport of drug molecules across the vessel wall is proportional to the local drug concentration (c), and fluid extravasation rate (J_{v}). Fluid extravasation rate, as discussed in Section 2.3, is proportional to vessel surface area, and the difference between the microvascular and interstitial pressures. Convective extravasation rate of solutes, J_{s} (mg/s), is hindered due to size-exclusion on the pore wall and frictional interactions with water:

$$J_{\mathrm{s}} = cJ_{\mathrm{v}}\left(1-\sigma_{\mathrm{f}}\right), \tag{2.8}$$

where J_{v} is the fluid flux across the vessel wall (ml/sec), and σ_{f} the solvent drag reflection coefficient, which is a function of the size of the solute relative to the pore

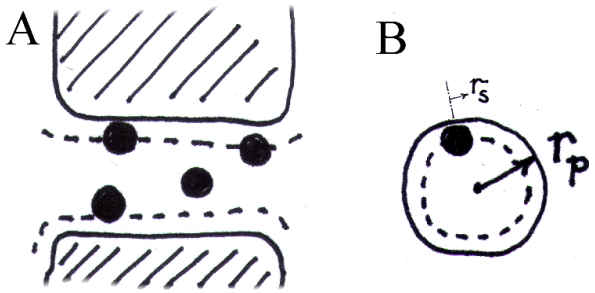

Figure 2.6. Steric hindrance of the solutes due to size exclusion on the pore wall. A: longitudinal cross section of a pore. B: front view of a pore. Dashed lines: boundary of the pore space available to the solutes.

size. An alternative notation seen in the literature uses the convective hindrance factor, $W = 1-\sigma_{\mathrm{f}}$. If $W = 0$, the vessel wall is completely impermeable to the solutes, although fluid may seep through. When $W = 1$, solutes are transported along with the fluid without obstruction.

To calculate σ_{f}, we first introduce the partition coefficient of the solute, ϕ, which is the ratio of the area available to the solute to the actual pore area [65] (See Figure (2.6)). For cylindrical pores,

$$\phi_{\mathrm{pore}} = \frac{\pi \left(r_{\mathrm{p}} - r_{\mathrm{s}}\right)^2}{\pi r_{\mathrm{p}}^2} = \left(1 - \frac{r_{\mathrm{s}}}{r_{\mathrm{p}}}\right)^2, \tag{2.9}$$

where r_{s} is the solute radius and r_{p} is the pore radius. For slit-shaped openings,

$$\phi_{\mathrm{slit}} = \frac{\mathrm{L}\left(\mathrm{W} - 2r_s\right)}{\mathrm{LW}} = 1 - \frac{2r_s}{\mathrm{W}}, \tag{2.10}$$

where L is the length and W is the width of the slit. If the flow is laminar, fluid velocity within the pore, $v(\rho)$, will follow a parabolic profile:

$$v(\rho) = v_{\mathrm{max}} \left[1 - \frac{\rho^2}{r_{\mathrm{p}}^2}\right], \tag{2.11}$$

where ρ is the radial distance, $v_{\max}$ is the fluid velocity at the center line of the pore. Assuming that solutes travel with the local velocity of the fluid, and integrating over the pore area available to solutes, we obtain the convective flux of solutes:

$$J_{\mathrm{s}} = \int_0^{r_{\mathrm{p}}-r_{\mathrm{s}}} \mathrm{d}\rho \; c 2\pi\rho v_{\max}\left[1-\frac{\rho^2}{r_{\mathrm{p}}^2}\right] \tag{2.12}$$

$$= \frac{1}{2}\pi v_{\max} c r_{\mathrm{p}}^2\left[2\phi_{\mathrm{pore}}-\phi_{\mathrm{pore}}^2\right]. \tag{2.13}$$

Dividing the result by $J_{\mathrm{v}} = \int_0^{r_{\mathrm{p}}} \mathrm{d}\rho \; 2\pi\rho v(\rho) = \frac{1}{2}\pi r_{\mathrm{p}}^2 v_{\max}$, and following Equation 2.8, one retrieves σ_{f}:

$$\sigma_{\mathrm{f}} = \left(1-\phi_{\mathrm{pore}}\right)^2. \tag{2.14}$$

Similar calculation for rectangular slits produces:

$$\sigma_{\mathrm{f}} = 1-\frac{3}{2}\phi_{\mathrm{slit}}+\frac{1}{4}\phi_{\mathrm{slit}}^3. \tag{2.15}$$

See Figure 2.8 for a plot of convective hindrance factor, $W = 1-\sigma_{\mathrm{f}}$, with respect to $\frac{r_s}{r_{\mathrm{p}}}$ for cylindrical pores.

Corrections to σ_{f} have been proposed due to frictional interactions of solutes with water molecules. However, Equation 2.14 is a sufficient approximation for the purpose of this thesis. In a study with homophore membranes by Schultz *et al.* [90], σ_{f} was measured for solutes and pores of varying sizes, and compared against Equation 2.14. The study concludes that a non-circular and flexible molecules have a lower reflection coefficient than predicted by Equation 2.14. For modeling the delivery of spherical nanoparticles, Equation 2.14 is expected to yield accurate values as they are sufficiently rigid structures.

It must be noted that in general, solvent drag reflection coefficient (σ_{f}) is distinct from osmotic reflection coefficient (σ_{d}). When solute-solute interactions are negligible (i.e., in dilute solutions), $\sigma_{\mathrm{f}} \cong \sigma_{\mathrm{d}}$ [37]. This assumption is sometimes tacitly made in the literature and a single quantity, the reflection coefficient (σ) is used interchangeably for both concepts.

2.5.2. Diffusive Transport Across the Vessel Wall

In absence of convective fluid flux, transmembrane diffusion rate of drug molecules is proportional to vascular permeability (P_{d}), exchange surface area of the capillary wall (S), and the difference between the plasma and interstitial concentrations, $\Delta c = c_p - c_i$ [15]. Coefficient of vascular permeability depends on the diffusion coefficient of the solute in interstitial fluid (D_0), and the geometry and distribution of openings in the vessel wall. An analysis of these dependencies are given in this section.

We first derive the the equation of diffusion through a porous membrane. In an infinitesimally small exchange area, the problem of membrane diffusion has planar symmetry. In the case of free planar diffusion (without a membrane), Fick's law is:

$$j_0 = -D_0 \frac{\mathrm{d}c}{\mathrm{d}x}, \tag{2.16}$$

where j_0 is the free diffusion flux of solutes (mg/mm^2·s), D_0 is the free diffusion coefficient, and c is the solute concentration (mg/mm^3). If we now place a planar, Δx-thick, porous membrane across the concentration gradient, diffusive flux is restricted to the total available cross sections of the pores:

$$J_{\mathrm{s}} = D_0 \frac{\Delta c}{\Delta x} \mathrm{S} \sum_i n_i \phi_i A_i, \tag{2.17}$$

where J_{s} is the total diffusional flux of solutes across the porous membrane (mg/s), S is

Table 2.5. Vascular permeabilities (L_p) for Albumin and 90 nm Liposomes in different types of tissues.

Agent and tissue	**Vascular Permeability** ($\times 10^{-8}$ cm/s)	**Ref.**
90 nm Liposomes		
colon adenocarcinoma, LS174T	2	[91]
colon adenocarcinoma, LS174T	17–34	[30]
normal tissue	8–9	[30]
Albumin		
Fischer rat, R3230AC	17	[7]
C3H mouse, MCaIV	29	[7]
SCID mouse, MCaIV	19	[7]
SCID mouse, U87	38	[7]
SCID, HGL21	1.1	[7]
normal tissue, carcinoma	7.3, 57.2	[92]

the membrane total cross section area (mm^2), Δc is the concentration difference across the membrane, n_i is the population density (number per area) of vascular openings (either cylindrical pores or slits) which have the area A_i, and ϕ_i is the partition coefficient of the solute within these pores. ϕ introduces the size exclusion effect (i.e., steric hindrance), as discussed in Section 2.5.1. Diffusion of solutes within the pore is further slowed down by the viscous drag on the pore wall, which is called the hydrodynamic hindrance. The fractional reduction in diffusion due to hydrodynamic hindrance (ψ) is calculated by Renkin [93] for diffusion of hard spheres through cylindrical pores, as:

$$\psi_{\text{pore}} = 1 - 2.104\alpha + 2.089\alpha^3 - 0.095\alpha^5 - 1.372\alpha^6, \tag{2.18}$$

and through rectangular slits as:

$$\psi_{\text{slit}} = 1 - 1.004\alpha' + 0.418\left(\alpha'\right)^3 + 0.210\left(\alpha'\right)^4 - 0.170\left(\alpha'\right)^5, \tag{2.19}$$

where α is the ratio of solute radius to pore radius, $\alpha = \frac{r_s}{r_p}$, and α' is the ratio of solute

radius to slit half-width, $\alpha' = \frac{2r_s}{\mathrm{W}}$. Including both steric (ϕ) and hydrodynamic (ψ) effects, we obtain the equation of diffusional flux through a heteroporous membrane:

$$J_{\mathrm{s}} = D_0 \frac{\Delta c}{\Delta x} S \sum_i \psi_i \phi_i n_i A_i. \tag{2.20}$$

Following the membrane diffusion equation,

$$J_{\mathrm{s}} = P_{\mathrm{d}} \mathrm{S} \Delta c, \tag{2.21}$$

one obtains the coefficient of permeability P_{d} (mm/s) for the heteroporous membrane:

$$P_{\mathrm{d}} = \frac{D_0}{\Delta x} \sum_i \psi_i \phi_i n_i A_i. \tag{2.22}$$

Steric (ϕ) and hydrodynamic (ψ) hindrance effects are combined in a single parameter called the diffusive hindrance factor ($H = \phi\psi$), which is a function of only the relative size of the solute with respect to pores. See Figure 2.8 for plots of H and W with respect to $\frac{r_s}{r_{\mathrm{p}}}$. Equation 2.22 could be used to estimate the diffusional permeability of tumor vessels for specific pore size distributions.

2.5.3. The Global Convection-Diffusion Equation

We now want to calculate the total solute flux that results from combination of convective and diffusive transport. We assume that solute concentration along the pore, $c(x)$, varies smoothly from the plasma value (c_p) to the interstitial value (c_i). Note that the concentration profile is not necessarily linear, but it would depend on the fluid flux, J_{v}. Only in pure-diffusion, $c(x)$ would obtain a linearly decreasing profile, whereas for larger J_{v}, the concentration within the pore in overall would shift towards c_p (See Figure 2.7). With these in mind, one must sum the local rates of diffusional and convective

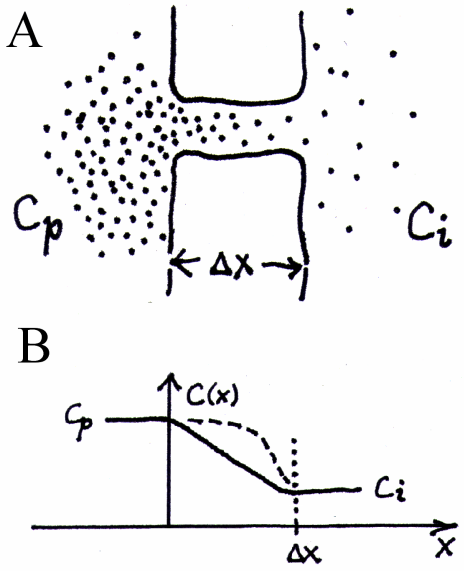

Figure 2.7. Diffusion of solutes along a vascular pore. A: vascular and interstitial concentrations. B: dependence of the concentration profile on the fluid flux. Solid line: pure-diffusion, $Pe = 0$. Dashed line: convection-dominated transport, $Pe \gg 1$.

flux, and integrate across the membrane to derive a correct global convection-diffusion equation [77]. By the Fick's law, local diffusion flux within the pores is:

$$J_{\mathrm{s,d}}(x) = -P_{\mathrm{d}}^{\prime}\mathrm{S}\frac{\mathrm{d}c(x)}{\mathrm{d}x}, \tag{2.23}$$

where $P_{\mathrm{d}}^{\prime}$ is the local coefficient of permeability, $P_{\mathrm{d}}^{\prime} = P_{\mathrm{d}}\,\Delta x$, where P_{d} is given by Equation 2.22. The local rate of convective flux is:

$$J_{\mathrm{s,c}}(x) = c(x)\,J_{\mathrm{v}}\,(1-\sigma_{\mathrm{f}})\,. \tag{2.24}$$

Local transport flux is the sum of the local rates of diffusive and convective flux:

$$J_{\mathrm{s}}(x) = -P_{\mathrm{d}}^{\prime}\mathrm{S}\frac{\mathrm{d}c(x)}{\mathrm{d}x} + c(x)\,J_{\mathrm{v}}\,(1-\sigma_{\mathrm{f}})\,. \tag{2.25}$$

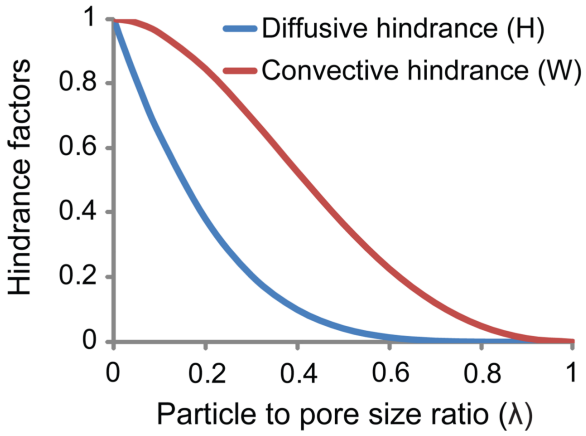

Figure 2.8. Dependence of convective (W) and diffusive (H) hindrance factors on the ratio of solute size to pore size. Reprinted from [9].

We now assume a quasi-steady profile for the solute concentration $c(x)$ along the pore. Then, by $\dot{c} = 0$ and $\dot{c} + \nabla J_s = 0$, we have $J_{\mathrm{s}}(x) = J_{\mathrm{s}} = \text{const}$. Note that this assumption is valid only if concentrations at either side of the membrane changes very slowly. By multiplying Equation 2.25 with the integration factor $\mu(x) = e^{-\frac{J_{\mathrm{v}}(1-\sigma)}{P_{\mathrm{l}}\mathrm{S}}x}$ and integrating across the membrane $\{0, \Delta x\}$, we obtain:

$$-\frac{J_{\mathrm{s}}}{J_{\mathrm{v}}\left(1-\sigma_{\mathrm{f}}\right)}\exp\left[-\frac{J_{\mathrm{v}}\left(1-\sigma_{\mathrm{f}}\right)}{P'_{\mathrm{d}}S}x\right]\Bigg|_{x=0}^{x=\Delta x} = c(x)\exp\left[-\frac{J_{\mathrm{v}}\left(1-\sigma_{\mathrm{f}}\right)}{P'_{\mathrm{d}}S}x\right]\Bigg|_{x=0}^{x=\Delta x} \tag{2.26}$$

Using the boundary conditions $c(0) = c_p$ and $c(\Delta x) = c_i$ for either end of the pore, we obtain the nonlinear global rate of solute flux, which is also known as the Patlak equation:

$$J_{\mathrm{s}} = J_{\mathrm{v}}\left(1-\sigma_{\mathrm{f}}\right)\frac{c_p e^{\mathrm{Pe}} - c_i}{e^{\mathrm{Pe}} - 1}\ , \tag{2.27}$$

where Pe is a modified Peclet number, $\mathrm{Pe} = J_{\mathrm{v}}\left(1-\sigma_{\mathrm{f}}\right)/P_{\mathrm{d}}\mathrm{S}$. Solute flux could be separated into contributions from convection and diffusion;

$$J_{\mathrm{s}} = c_p J_{\mathrm{v}}\left(1-\sigma_{\mathrm{f}}\right) + P_{\mathrm{d}}\mathrm{S}\left(c_p - c_i\right)\frac{\mathrm{Pe}}{e^{\mathrm{Pe}} - 1}. \tag{2.28}$$

Equation 2.28 is called the nonlinear global convection-diffusion equation [77]. Note that for convection-dominated transport (Pe $\gg 1$), the correction term on the second term at right becomes significantly small, to reflect the changing concentration profile along the pore. Therefore the linear convection-diffusion equation for transmembrane transport,

$$J_{\mathrm{s}} = c_p J_{\mathrm{v}} \left(1 - \sigma_{\mathrm{f}}\right) + P_{\mathrm{d}} \mathrm{S} \left(c_p - c_i\right), \tag{2.29}$$

should not be used in convection dominated transport (such as in nanoparticle delivery), as it may overestimate the solute flux.

2.6. Transport of Drugs in the Interstitial Space

Following extravasation, drugs enter the intercellular space. Interstitial space is filled with the interstitial fluid, and includes the extracellular matrix, which is a complex gel of polysaccharides and fibrous proteins (See Figure 1.1). Within this biochemically active, heterogeneous and geometrically tortuous medium, drugs are transported by diffusion and convection. As drugs diffuse through the tissue, they may bind to the components of the ECM, become biologically metabolized, leave the interstitium via lymphatic drainage, or penetrate a host or tumor cell. Due to this continuous removal of free drug molecules, its penetration length beyond the capillary wall is reduced. Assuming a fixed drug concentration in blood, the characteristic length of drug penetration at steady state is $L_c = \sqrt{2c_0/\lambda_c}$, where λ_c is the consumption rate due to the above processes. In accordance, non-specific binding of drug molecules to the ECM and cellular membrane proteins inhibits drug penetration, and higher blood concentrations does not effectively increase the penetration length.

2.6.1. Diffusive Transport in the Interstitial Space

Diffusibility of particles within interstitium decreases with increasing particle size, both due to the reduced free diffusion coefficient (according to the relation $D_0 = \frac{k_B T}{6\pi\mu r}$), and to increased steric hindrance by the ECM. Especially, particles larger than 25-60 nm are not able to effectively penetrate the interstitial space, and they remain localized near blood vessels after extravasation [28,91,94]. In this respect, delivery of large therapeutic agents, such as liposomes, nanospheres and quantum dots is problematic. Permeability also depends on the content and organization of the interstitial space. For instance, permeability is reduced, in tumors with high collagen content. A denser collagen network, by stabilizing GAG and HA strains, increases tissue resistance to macromolecule transport [78]. Diffusion rate of charged particles is lower due to electrostatic interaction with the charged regions of the ECM, such as the negatively-charged GAG chains [10].

Due to physical obstacles, pore connectivity and frictional drag in the interstitium, effective measured diffusion in tissues is slower than free diffusion in water. The effective diffusion coefficient in the tissue (D_{eff}) and the free diffusion coefficient in water (D_0) are related as $D_{\text{eff}} = \frac{1}{\tau^2} D_0$, where the factor τ, is called the tortuosity of the medium. τ is separated into the geometric contribution (i.e., physical obstructions of the cells) τ_{g} and the viscous contribution (i.e., frictional drag due to the ECM) τ_{v}, as $\tau = \tau_{\text{g}}\tau_v$. For smaller particles, viscous drag is negligibly small, and interstitial space geometry imposed by the organization of the cells govern the diffusion rate i.e., $\tau \backsimeq \tau_{\text{g}}$. For instance, in human glioblastoma grown in dorsal chamber in mice, geometric tortuosity, τ_{g}, was determined as 1.19. High tumor cell density is known to hinder the penetration of cytotoxic drugs [51,95,96], presumably due to the increased geometric tortuosity. For particles having sizes comparable to interstitial flow channels (e.g., collagen fiber spacing: 75-130 nm), diffusion rate is significantly reduced by the frictional drag on the ECM [94]. For reference, Table 2.6 and Figure 2.9 give the diffusion coefficients of macromolecules and nanoparticles in various sizes and in several types of tissues. Diffusion coefficients of macromolecules in tumors is generally higher than in normal tissues. This may due to the greater fraction of the interstitial

Table 2.6. Diffusion coefficients of several macromolecules in tissue and water.

Agent	M_r (kDa)	r_H (nm)	**Medium**	**Diffusion coefficient** ($\times 10^{-7}$ cm^2/s)	**Ref.**
90 nm liposomes	-	90	water glioma	0.6 0.04	[94]
2M dextran	2000	20	water glioma melanoma	1.5 0.1 0.01	[94]
150k dextran	150	-	normal tumor	0.0067 0.22	[92]
IgG protein	150	4.7	various tumors	0.96–1.97	[78]
BSA	68	3.5	various tumors	3.5	[78]
doxorubicin	0.54	1	normal tumor	15.8 34.0	[11,79]
cisplatin[a]	0.30	0.5	normal, tumor	22 64	[11]
glucose	0.18	-	various tissues	2.3–6.7	[88,98]
oxygen	0.032	-	various tissues	100	[11]

[a] values are of sodium fluoride (NaF, $M_r = 376$, $r_H = 0.48$ nm), as representative of Cisplatin

space in tumors (0.2–0.6) compared to that in normal tissues [11]. Also, it has been shown that lower tumor cell density results in better drug penetration, presumably due to increased fraction of interstitial space and/or reduced tortuosity (i.e., decreased τ_g) [95,97].

2.6.2. Convective Transport in the Interstitial Space

Convective transport of drugs occurs via the interstitial fluid flow, and it may significantly alter the spatial distribution of drugs. For instance, an outward interstitial fluid velocity (0.1–4 μm/s) is generally observed at the boundaries of solid tumors, which sweeps the drug molecules towards the surrounding healthy tissue [2,13,14,99]. Convective flux of solutes in tissue, j_s (mg/mm^2·s), is described by:

$$\mathbf{j}_s = \mathbf{q}_{IF} r_f c, \tag{2.30}$$

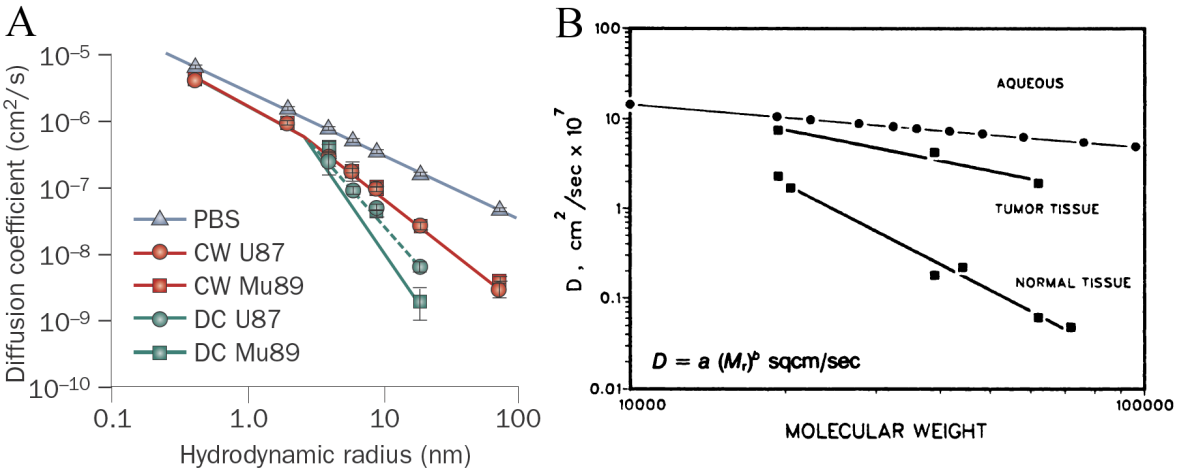

Figure 2.9. Diffusion coefficients for various hydrodynamic radii in PBS and in various tumors (left, from Jain and Stylianopoulos [10]). Dependence of dextran diffusion coefficients on molecular weight and tissue type (right, from Nugent and Jain [11]).

where q_{IF} is the interstitial fluid flux (mm/s), r_f is the retardation factor (or interstitial convective hindrance), c is the solute concentration (mg/ml). The retardation factor, r_f, is the ratio of solute convective flow velocity to interstitial fluid velocity. It is a measure of solute convective drag that occurs due to mechanical hindrance and charge interactions with the ECM, therefore, is a function of the particle size and structure and content of the ECM [79,100]. Reddy *et al.* have measured r_f in mouse tail, for 3, 40, 71, 2000 kDa dextrans and 40 nm nanospheres [100] as 1.9, 2.5, 7, 1.9, 0.7, respectively. Interestingly, due to a size exclusion effect, r_f could be larger than 1. Particles are excluded from narrow fluid channels (where water velocity is slower), and they are preferentially convected through wider ones (where water velocity is larger), resulting in a larger particle velocity than the average fluid velocity. This effect increases with particle size, but after a certain size, hindrance effects dominate and r_f decreases. r_f also decreases with increasing GAG and HA content of the tissue [79].

2.7. Lymphatic Clearance of Interstitial Fluid and Drug Particles

In healthy tissues, lymph vessels drain excess interstitial fluid to maintain the interstitial fluid balance [10]. Fluid drained at the blind-ended lymph capillaries is drawn through the lymph channels, and reenters the systemic circulation at the subclavan veins. The lymphatic system lacks an active pressure head such as in the blood

circulation. Fluid flow into the initial lymph capillaries is mainly driven by IFP, while the transport in the collecting lymph channels relies on rhythmic contractions of the channels that push the fluid through series of one-way valves [101]. Hydrostatic fluid pressure inside lymph capillaries (P_{l}) is around 5 mmHg [102, 103]. Because lymph protein concentration is higher than interstitial protein concentration [104], the oncotic pressure contribution and supports fluid drainage, and also results in an effective lymphatic pressure of close to zero, $\mathrm{P_{l,eff}} = \mathrm{P_l} - \sigma_{\mathrm{l}}\Delta\pi_{\mathrm{l}} \approx 0$. We therefore assume that the rate to fluid flow into lymphatics is proportional to IFP. Lymph vessels, forming a dense regular network in normal tissues with intervascular distance of 200-300 μm [12, 105], could be considered as a continuous sink in modeling of interstitial fluid flow. Then, by Starling's law, the macroscopic rate of fluid loss to lymph vessels (Γ_{Fl}) is:

$$\Gamma_{\mathrm{Fl}} = -\lambda_{\mathrm{Fl}}\mathrm{P}, \tag{2.31}$$

where λ_{Fl} is the lymphatic filtration coefficient, related to lymph vessel surface density ($\frac{S_{\mathrm{l}}}{V}$) and lymph vessel wall hydraulic conductivity (L_{pl}) by $\lambda_{\mathrm{Fl}} = \frac{\mathrm{S_l}}{\mathrm{V}} L_{pl}$. Due to compression of the cancer cells, lymph vessels within the tumor collapse and functional lymphatics are only observed outside of the tumor [12, 106] (See Figure 2.10). Therefore we take $\lambda_{\mathrm{Fl}} = 0$ inside the tumor. In the host tissue, λ_{Fl} is in the order of 10^{-6} – 10^{-4} $\mathrm{mmHg^{-1}{\cdot}s^{-1}}$ [83, 107]. Note that in normal tissues, the range of λ_{Fl} is 1-2 orders of magnitude higher than that of λ_{Fb} (See Table 3.1). This difference, along with the high osmotic pressure contribution across the blood and lymph capillaries, helps maintain an IFP (P) of close to zero in healthy tissues.

Both through re-absorption by the venules and by lymphatic drainage, drug molecules are removed from the interstitium. Smaller molecules (r_H: 3–5 nm) are rapidly cleared from the tissue by these routes, while larger particles (r_H>10 nm) could be retained within the interstitial space for several days [28]. Fluid is drained into the lymph capillaries through the loose interendothelial gaps on the capillary wall.

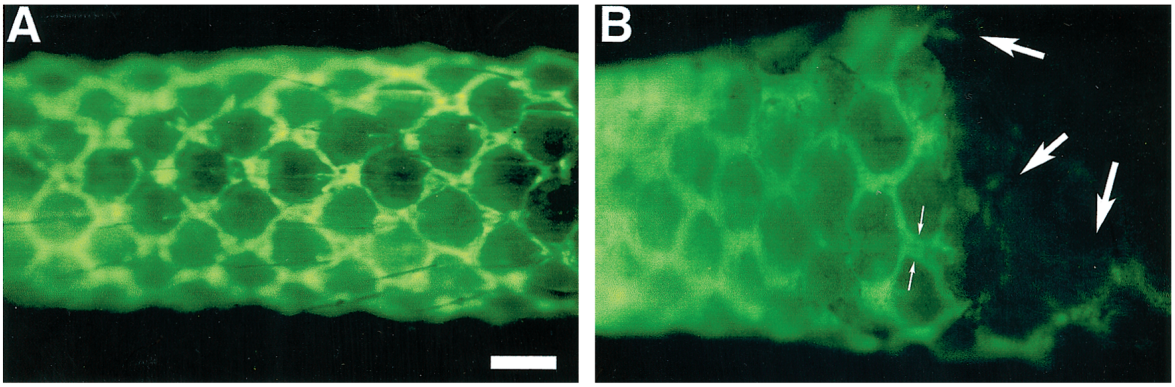

Figure 2.10. Functional lymph vessels of a normal (A) and tumor-implanted (B) mouse tail. Green: fluorescent stained lymph vessels. Large arrows: attenuated vessels possibly inside tumor. Bar: 400 μm. Reprinted from Leu *et al.*, 2000 [12].

It can be assumed that while drug particles cross the lymph capillary wall via convection, they do not undergo hindrance (i.e., $\sigma_{\mathrm{d}} \approx 0$). Then, by Equation 2.8, clearance rate of drugs near a lymph capillary, J_{s} (mg/s), is:

$$J_{\mathrm{s}} = -L_{\mathrm{pl}} S_l \mathrm{P} c, \tag{2.32}$$

where L_{pl} is the hydraulic conductivity and $\mathrm{S_l}$ is surface area of the capillary wall; P is the interstitial fluid pressure and c is the drug concentration near the capillary.

3. A CONTINUUM MODEL OF DRUG DELIVERY

3.1. Introduction

Delivery of drugs to solid tumors is impaired by the physical and physiological properties of the tumor environment. Structural irregularities in tumor vasculature lead to heterogeneous blood perfusion and drug distribution [10, 18, 22, 28, 91]. In addition, leakiness of tumor vessels and absence of functional lymphatics result in elevated levels of interstitial fluid pressure (IFP) within tumors [2]. Elevated IFP poses a barrier to drug delivery by means of reduced convective transvascular transport of drug molecules [13,15]. Convective transport of drug molecules within interstitial space is also impaired, because typically, IFP is elevated uniformly within tumors [2, 19]. Elevated IFP is accompanied by an outward flux of interstitial fluid at the tumor boundary, which might wash out the drug molecules towards health tissue [13, 14]. It has been argued that drug delivery could benefit from restoring the hydrostatic pressure gradients within tumors.

In the recent years, treatment of tumors with several anti-angiogenic agents was shown to decrease vessel diameter, increase blood flow and oxygenation, reduce vascular permeability, reduce IFP and restore transvascular pressure gradients, in a transient manner after administration [22, 23, 108]. The rationale is to provide the tumor vasculature with structure and function of normal vessels (normalization) by restoring the balance between pro- and anti-angiogenic factors in the tumor environment [18]. In several studies with mouse models normalization therapy improved the delivery and efficacy of chemotherapeutic agents [24,108–113]. Also, in a study by [23], normalization using a VEGF-receptor-2 antibody significantly improved the penetration of bovine serum albumin into tumor tissue. In recent clinical trials, anti-angiogenic therapy in combination with standard chemotherapy improved the outcome of patients with gastrointestinal cancer [114–116], non-small cell lung cancer [117,118], ovarian cancer [119] and breast cancer [120–122].

There is growing evidence that normalization therapy could also improve the delivery of large-molecule therapeutics, such as nanospheres and liposomes [9, 23, 123, 124]. Using nanoparticles for treatment and detection of solid tumors is especially desirable because of the enhanced permeability and retention (EPR) effect. Tumor vessels, having larger pores (100-780 nm, [58]) compared with normal vessels (2-6 nm), allow for targeted delivery of nanoparticles larger than 10 nm. Since transport of such large particles depends heavily on convection, removing the interstitial pressure barrier might improve the selective delivery of nanoparticles into solid tumors [10].

It is not clear whether, and in what conditions, changes induced by vascular normalization therapy might improve delivery of nanoparticles. In this study, we use a mathematical model to investigate how normalization therapy influences the transport of interstitial fluid and 100-nm liposomes. We determine the changes in the total tumor exposure and homogeneity of spatial distribution, which are major determinants for efficiency of anti-tumor drugs.

3.2. Mathematical Model

Previous mathematical models [14, 21] and experimental measurements [2] have shown that IFP is elevated in solid tumors. In this study, we model the transvascular and interstitial transport, and lymphatic drainage of the interstitial fluid.

3.2.1. Transport of Interstitial Fluid

Considering that the typical value for inter-capillary distance in tumors is 300 μm [42], considerably smaller than the tumors modeled in this study ($>$ 1 mm), we assume that blood and lymph vessels are uniformly distributed sources and sinks of fluid. The interstitial space is saturated by the interstitial fluid, and we denote its volume fraction by ϕ_F. The mass balance equation for interstitial fluid is:

$$\boldsymbol{\nabla} \cdot (\phi_F \mathbf{v}_{\mathrm{IF}}) = \Gamma_{Fb} - \Gamma_{Fl} \tag{3.1}$$

where Γ_{Fb} (1/s) represents the supply of fluid from blood vessels to the interstitial space, and Γ_{Fl} (1/s) represents the drainage of fluid from interstitial space into lymph vessels. We use Starling's law to determine these quantities:

$$\Gamma_{\mathrm{Fb}} = \lambda_{\mathrm{Fb}} \left[\mathrm{P_v} - \mathrm{P} - \sigma(\pi_c - \pi_i)\right] \tag{3.2}$$

$$\Gamma_{\mathrm{Fl}} = \lambda_{\mathrm{Fl}}\mathrm{P} \tag{3.3}$$

where λ_{Fb} and λ_{Fl} are hydraulic conductivities of blood and lymph vessel networks (1/mmHg·s), $\mathrm{P_v}$ is the vascular fluid pressure (mmHg), P is the interstitial fluid pressure (IFP, mmHg), σ is the osmotic reflection coefficient, and π_c and π_i are the capillary and interstitial oncotic pressures (mmHg), respectively. Hydraulic conductivities of blood and lymph vessel networks, are related to their vessel wall hydraulic conductivities (L_{p}) and vessel surface densities ($\frac{S}{V}$) by $\lambda_{\mathrm{Fb,Fl}} = L_{\mathrm{p}}\frac{\mathrm{S}}{\mathrm{V}}$. Because lymph vessels are highly permeable, we neglected the osmotic pressure contribution in the relation for lymphatic drainage (3.3). We also assumed that lymph vessel pressure is 0 mmHg [125].

We use Darcy's law to describe the flow of interstitial fluid within the tissue:

$$\mathbf{q}_{\mathrm{IF}} = -K\boldsymbol{\nabla}\mathrm{P}, \tag{3.4}$$

where $\mathbf{q}_{\mathrm{IF}}$ is the interstitial fluid flux (IFF, mm/s) and K is the hydraulic conductivity of the tissue (cm^2/s·mmHg). IFF is related to velocity of the interstitial fluid ($\mathbf{v}_F$) by $\mathbf{q}_{\mathrm{IF}} = \phi_{\mathrm{F}}\mathbf{v}_{\mathrm{IF}}$. Substituting Equations 3.2, 3.3 and 3.4 into the mass balance equation (Equation 3.1), we obtain:

$$\boldsymbol{\nabla}\cdot(-K\boldsymbol{\nabla}\mathrm{P}) = \lambda_{Fb}\left[\mathrm{P_v} - \mathrm{P} - \sigma\Delta\pi\right] - \lambda_{Fl}\mathrm{P}. \tag{3.5}$$

Table 3.1. Interstitial fluid transport parameters.

Parameter	**Value in tumor**	**Value in normal tissue**	**Unit**
L_{p}	1.86×10^{-6} [a]	3.6×10^{-8} [a]	cm/mmHg-s
$\frac{\mathrm{S}}{\mathrm{V}}$	200 [b]	70 [b]	$\mathrm{cm}^2/\mathrm{cm}^3$
λ_{F}	3.72×10^{-4} [c]	2.52×10^{-6} [c]	1/mmHg-s
λ_{Fl}	0 [d]	6.66×10^{-4} [e]	1/mmHg-s
$\mathrm{P_v}$	15 [a]		mmHg
$\sigma\Delta\pi$	2.2×10^{-4} [a]	9.1 [a]	mmHg
$\mathrm{P_{eff}}$ [f]	15	5.9	mmHg
K	2.5×10^{-7} [a]	2.5×10^{-7} [a]	cm^2/mmHg-s

[a] [14]
[b] [37]
[c] calculated from $L_P\frac{S}{V}$, assuming vessels as continuously distributed sources
[d] [12, 106]
[e] [107]
[f] $\mathrm{P}_{eff} = \mathrm{P_v} - \sigma\Delta\pi$, effective vascular pressure

3.2.2. Transport of Drug Molecules

Drug molecules reach the tumor tissue through blood and extravasate from blood vessels by diffusion and by convection within interstitial fluid. After this stage, they have to travel within the interstitial space in order to reach tumor cells. Molecules are then removed from the interstitial space, either by biological decay or by being drained to lymph vessels with the interstitial fluid. We model the transport of liposomes using a reaction-diffusion-advection equation:

$$\frac{\partial c}{\partial t} + \boldsymbol{\nabla}\cdot(-D\boldsymbol{\nabla}c) + \boldsymbol{\nabla}\cdot(\mathbf{q}_{\mathrm{F}}\mathrm{r_f}c) = \Gamma_{Fb}(1-\sigma)c_p + \lambda_d\left(c_p - c\right)\frac{\mathrm{Pe}}{e^{\mathrm{Pe}}-1} - \Gamma_{Fl}c - \lambda_r c, \quad (3.6)$$

where c and c_p are the tissue and plasma drug concentrations ($1/\mathrm{mm}^3$), D is the diffusion coefficient in the tissue (cm^2/s), $\mathrm{r_f}$ is the retardation coefficient for interstitial convection, σ is the solvent drag reflection coefficient for transvascular convection, λ_d is the transvascular diffusion coefficient ($1/\mathrm{s}$), Pe is the Peclet number, equal to $\Gamma_{Fb}\left(1-\sigma_{\mathrm{f}}\right)/\lambda_d$, and λ_{r} is the decay rate of drug molecules ($1/\mathrm{s}$). The terms on the right hand side of Equation 3.6, describe extravasation of drug molecules by convection and by diffusion, clearance by the lymphatic network, and biological decay, respectively.

Transvascular diffusion coefficient, λ_{d}, is calculated using $P_{\mathrm{d}}\frac{S}{V}$, where P_{d} is the vascular permeability for liposomes. Experimentally measured values of P_{d} are "effective" values that represent both convective and diffusive transport. Since convection dominates the liposome transport, we assumed that actual diffusional permeability for liposomes is 5% of the effective permeability measured in [30]. Table 3.2 lists the values used in this model for the parameters relevant to transport of liposomes.

We assume that the vascular network is continuously distributed and intercapillary drug concentration is not influenced by the extravasation of drug molecules. We introduce a bolus drug injection through a single exponential decay function for time-dependent plasma drug concentration:

$$c_p(t) = c_0 e^{-\ln(2)t/t_{1/2}} \qquad t \geqslant 0\,, \tag{3.7}$$

where c_0 is the peak plasma concentration of the drug after injection and $t_{1/2}$ is the plasma half-life of the drug.

In many clinical and experimental studies, it was observed that drugs are heterogeneously distributed within solid tumors [126]. As a result of this, some of the tumor cells are not exposed to drugs in sufficient amounts and they may survive the treatment and continue proliferating afterwards. Uniformity of drug distribution is therefore a determinant for the efficiency of an anti-tumor treatment, as well as the total dose that reaches cancer cells. Accordingly, we define dimensionless quantities that measure total tumor exposure (Φ_e) and heterogeneity of drug distribution (Φ_h), in order to compare the efficiency of drug delivery with and without vascular normalization:

$$\Phi_e = \frac{1}{t_T c_0}\int_0^{t_T} \mathrm{d}t\, \langle c \rangle_{\Omega_T}\ , \tag{3.8}$$

Table 3.2. Parameters related to transport of 100 nm liposomes

Parameter	**Value in tumor**	**Value in normal tissue**	**Unit**
D	2.5×10^{-9} [a]		cm^2/s
k_{E}	0.35 [b]		-
$1-\sigma$	0.87 [c]	0	-
P_d	$5\%\times3.42\times10^{-7}$ [d]	$5\%\times0.88\times10^{-7}$ [d]	cm/s
λ_d	4×10^{-6} [e]	1.4×10^{-7} [e]	1/s
λ_r	1/135 [f]		1/hours
$t_{1/2}$	45.2 [g]		hours

[a] [94]

[b] estimated from [100]

[c] estimated using $\sigma = \left(1-(1-\alpha)^2\right)^2$ with ratio of drug to pore radius, α = 100 nm/500 nm. [127]

[d] diffusional permeabilities taken to be %5 of the effective permeabilities measured in [30]

[e] calculated using $P_d\frac{S}{V}$.

[f] [128]

[g] [129]

and

$$\Phi_h = \frac{1}{t_T c_0}\int_0^{t_T} \mathrm{d}t \left\langle \left(c - \langle c\rangle_{\Omega_T}\right)^2 \right\rangle_{\Omega_T}^{1/2}, \tag{3.9}$$

where $\langle\,\cdot\,\rangle_{\Omega_T} = \frac{1}{\mathrm{V_T}}\int_{\Omega_\mathrm{T}} \mathrm{d}^3\mathbf{r}\,(\,\cdot\,)$ denotes averaging over the tumor domain, $\mathrm{V_T}$ is the tumor volume and t_T is the time interval for which the efficiency of the therapy is evaluated. Typical administration interval of liposome-based anti-cancer drugs is 2-4 weeks, also in our simulations over 99% of the drug was cleared from the interstitial space after 2 weeks; therefore, we set t_T = 2 weeks. Total tumor exposure (Φ_e) is the dimensionless concentration averaged over tumor tissue and therapy interval. Φ_h is the time-averaged sum of deviation of concentration from its mean tissue level, therefore measures the spatial heterogeneity of the drug distribution. According to these measures, higher values of Φ_e and lower values of Φ_h represent a more effective drug delivery.

3.2.3. Vascular Normalization

We model the effects of vascular normalization therapy by introducing a 50% percent decrease in the tumor vessel surface density ($\frac{S}{V}$; [130, 131]), 80% percent decrease in tumor vessel hydraulic conductivity (L_p; [14]), 60% percent decrease in tumor vascular network permeability ($P_{\mathrm{d}}\frac{S}{V}$; [132]) as the cited studies suggest. Osmotic reflection factor (σ) for homophore membranes could be approximated using $\sigma = \left(1-(1-\alpha)^2\right)^2$, where α is the ratio of solute radius to pore radius [127]. Assuming an effective pore size of 5 nm for normal and 450 nm for tumor vessels, we calculate the value of σ as 1 and 0.13, respectively, for 100 nm liposomes. We assumed that vessels in normal tissue was not affected by normalization.

3.2.4. Problem Domain and Boundary Conditions

In this study, we consider a spherically symmetric tumor embedded in normal tissue. Problem parameters assume uniform but separate values within the sub-domains of tumor (Ω_T) and normal (Ω_N) tissue. We denote the tumor radius with R_0. At the boundary between the tumor and normal tissue, we have the mass continuity relations for the interstitial fluid:

$$\left[-K\frac{\partial P}{\partial r}\right]_{r=R_0} = 0, \tag{3.10}$$

$$\left[-D\frac{\partial c}{\partial r} - K\frac{\partial P}{\partial r}(1-\sigma)\,c\right]_{r=R_0} = 0. \tag{3.11}$$

Symmetry boundary conditions are applied at the tumor center and far field:

$$\left.\frac{\partial P}{\partial r}\right|_{r=R_0,R^\infty} = 0, \tag{3.12}$$

$$\left.\frac{\partial c}{\partial r}\right|_{r=R_0,R^\infty} = 0. \tag{3.13}$$

3.3. Results and Discussion

We solved the model equations numerically and analyzed the influence of vascular normalization (as described in section (3.2.3)) on the tumor exposure (Φ_e) and heterogeneity of distribution (Φ_h) of the drug. Simulations showed that depending on the size of the tumor, vascular normalization may increase the total tumor exposure of the drug and homogenize its distribution within the tumor. We categorized the tumor spheroids modeled in the study according to their sizes as small ($R_0 = 1$ mm), medium-sized (2 mm $\geq R_0 \geq$ 10 mm), and large ($R_0 \geq 11$ mm). In small tumors, neither of Φ_e and Φ_h varied significantly between normalized vasculature and untreated vasculature. In medium-sized tumors with normalized vasculature, Φ_e was significantly higher, and Φ_h significantly lower in comparison to medium-sized tumors with untreated vasculature.

In our simulations, vascular normalization effectively decreased IFP in small tumors (by 9 mmHg, in tumor center), and significantly recovered transvascular pressure gradients (See Figure3.1a, $R_0 = 1$ mm). However, suppressed hydraulic conductivity of the normalized vasculature precluded the benefits of enhancing the transvascular pressure gradients. In consequence, extravasation rate of interstitial fluid and drugs were in fact lower, in comparison to untreated vasculature (See Figure 3.1b, $R_0 = 1$ mm). Outward convective flux near tumor boundary was considerably lower for normalized vasculature, due to decreased IFP. The overall effect was that total tumor exposure was not significantly influenced by normalization therapy (See Figures 3.2a and 3.1c, $R_0 = 1$ mm). These results suggest that beneficial effects of normalization on nanoparticle delivery in small tumors, if any, would rely on factors other than reduction of IFP, such as improvement of blood perfusion, and decrease of hypoxia, as suggested by [10, 18, 28, 91].

In medium-sized and large tumors with untreated vasculature, IFP was elevated to vascular pressure levels throughout the inner regions of tumors (See Figure 3.1a, $R_0 =$ 2–15 mm, untreated vasculature). In these regions, convective extravasation of drugs was nearly completely inhibited (See Figures 3.1b, $R_0 =$ 2–15 mm, untreated vas-

culature) and transvascular transport solely depended on diffusion, which is typically slow for nanoparticles. In addition, rapid convective extravasation occurred near tumor boundary, resulting in spatially heterogeneous drug distribution (Φ_h as high as 0.33, See Figure 3.2b, $R_0 = 2$–15 mm, untreated vasculature). In contrast, in medium-sized tumors with normalized vasculature, convective extravasation occurred throughout the tumor, and total exposure was up to 33% higher, and spatial heterogeneity was nearly 3 fold lower, compared to tumors with untreated vasculature (See Figure 3.2, $R_0 = 2$–8 mm). In terms of increasing Φ_e and decreasing Φ_h, normalization treatment was beneficial only in medium-sized tumors ($2 \text{ mm} \leq R_0 \leq 8$ mm).

Normalization in large tumors decreased IFP and improved convective extravasation only on the outer regions of tumors (See Figure 3.1b, $R_0 = 15$ mm). Therefore, although total exposure was slightly higher, spatial heterogeneity of distribution was not reduced. (See Figure 3.2, $R_0 = 15$ mm).

At the tumor boundary, IFP sharply decreases to its near-zero level resulting in outward interstitial fluid flow [13, 14]. This flow sweeps drug particles towards surrounding tissue. In a study by [13], fluorescent tracing molecules are concentrated at tumor boundary while they are absent in the inner parts of the tumors 24 hrs after IV administration. In addition, outward interstitial fluid flux was observed at the tumor boundary. Simulations suggest that via normalization, such convective washout of drug particles could be decreased by almost 50%.

This model investigates how interstitial fluid transport influences the spatial distribution of drugs in the macroscopic scale. However, besides elevated IFP, heterogeneous blood flow and presence of high-permeability regions in the vasculature also contribute to heterogeneous distribution of nanoparticles and macromolecules in tumors [30, 91]. In addition, due to their size, nanoparticles and macromolecules might not be able to penetrate the tumor tissue, and remain close to blood vessels after extravasation [28, 91]. Assuming a continuous vessel distribution, this model does not account for such effects at the microscopic scale. Tissue penetration length of individual drug particles could be investigated using the discrete model that we will present

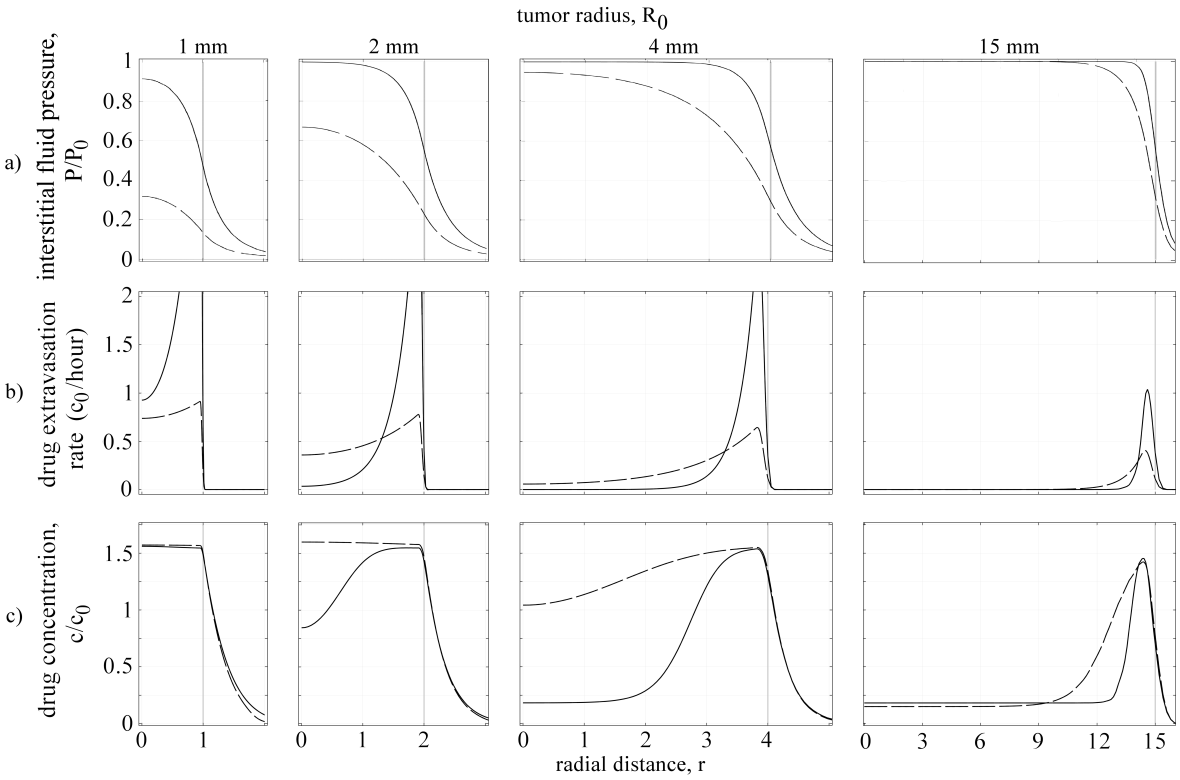

Figure 3.1. Comparison of IFP (a), convective extravasation rate (b), and drug concentration (c) for tumors of various sizes with normalized (dashed lines) and untreated (solid lines) vasculature. Fields plotted at $t = 24$ hours after injection.

in Chapter 4.

Several clinical trials [114–122] and laboratory experiments [23, 24, 108–113] have shown that vascular normalization treatment may improve drug delivery in some types of cancers. However, mechanisms behind such improvement are not yet fully understood. It is known that some improvement is via increased blood flow and reduced hypoxia [24–26] Our results suggest that two well known effects of vascular normalization, reduced vascular hydraulic conductivity and reduced surface density of tumor vessels, may improve the delivery of slow-diffusing therapeutic agents, such as liposomes. For the values of transport parameters used in this study (Tables 3.1 and 3.2) this range was calculated to be $2\text{ mm} \leq R_0 \leq 8\text{ mm}$. We note that for tumors of different types and at different vascularization stages, this range should vary.

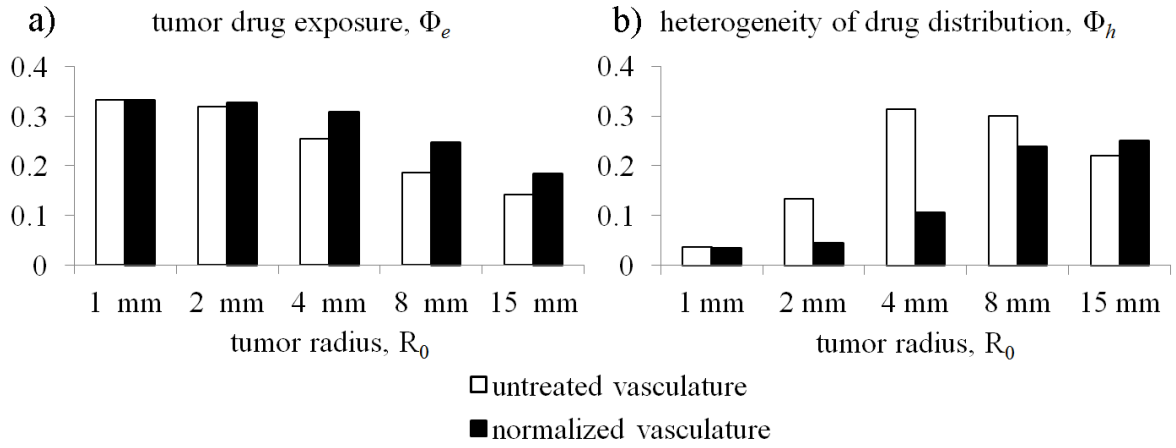

Figure 3.2. Influence of vascular normalization therapy on (a) total tumor drug exposure, Φ_e and (b) spatial heterogeneity of drug distribution, Φ_h, in various sizes of tumors.

4. A DISCRETE MODEL OF DRUG DELIVERY

Representative value of the drug delivery model introduced in Chapter 3, is limited by the assumptions that (i) vascular network acts as a continuously distributed source of interstitial fluid and drugs, (ii) tumor blood supply is homogeneous and (iii) extravasation of drug molecules does not reduce the drug concentration in the blood. As discussed in Section 2.7, the first assumption does not hold in tumors whose dimensions are comparable to intercapillary distances (~300 μm). In addition, as large molecular weight drugs remain localized in the vicinity of blood vessels after extravasation [28,30,91], the continuum model may underestimate the local drug concentration near vessel walls, and overestimate the concentration in the interstitium. The second assumption is not generally correct for tumors: tumor blood supply is often heterogeneous and this affects drug delivery [15]. The third assumption may not hold for drugs with very high microvascular permeability or within the capillaries in which the blood flow is stagnant. In such cases, as viewed from the material frame of the blood, a large portion of the drug particles would have enough time to extravasate, and plasma drug concentration would decrease considerably.

To overcome the above problems and obtain a more accurate picture of drug delivery, we have developed a discrete model that calculates the blood flow in individual vessel segments in coupling with the interstitial fluid flow.

4.1. Coupling Blood Flow and Interstitial Flow

In tumors, blood flow is strongly coupled to the interstitial flow via exchange of fluid across the vessels. We model the blood flow within vessels as laminar pipe flow. According to Poiseuille's law, the local rate of blood flow ($\mathbf{q}_{\mathrm{v}}$) is related to the pressure gradient along the vessel wall. We write Equation 4.1 as,

$$\mathbf{q}_{\mathrm{v}}(s) = -K_{\mathrm{v}} \frac{\partial \mathrm{P}_{\mathrm{v}}}{\partial s} \hat{\mathbf{s}}, \tag{4.1}$$

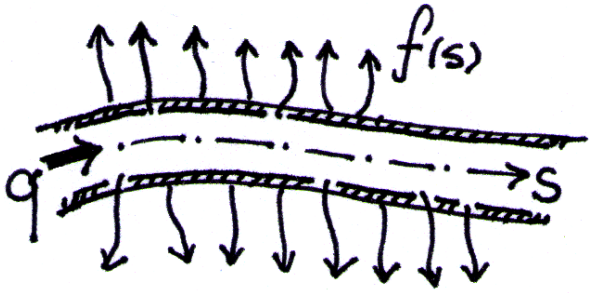

Figure 4.1. Mathematical representation of the vascular space and blood flow.

where K_{v} is the local flow conductivity, equal to

$$K_{\mathrm{v}} = \frac{\pi d_{\mathrm{v}}^4}{128\mu}. \tag{4.2}$$

Here, d_{v} is the vessel diameter (mm), and μ is the blood viscosity (mmHg·s). Here, the s is the curvilinear coordinate of the 1-dimensional vascular space. Fluid is lost from the vascular space by extravasation (See Section 2.3). The mass balance equation for the fluid in the vessels is:

$$-\boldsymbol{\nabla} \cdot \mathbf{q}_{\mathrm{v}}(s) = f(s)\,, \tag{4.3}$$

where $f(s)$ is the rate of fluid loss to the interstitial space through the vessel walls, measured per length of vessel ($\mathrm{mm}^3/\mathrm{mm}\cdot\mathrm{s}$). See Figure 4.1 for a visual description of the variables s, $\mathbf{q}_{\mathrm{v}}(s)$ and $f(s)$. By Starling's law, we can estimate $f(s)$ as:

$$f(s) = L_{\mathrm{p}} C \left(\mathrm{P}_{\mathrm{v}} - \mathrm{P}_{\mathrm{IF}}\right), \tag{4.4}$$

where L_{p} is the vessel hydraulic conductivity, C is the vessel wall circumference, and P_{v} and P_{IF} are the effective vascular and interstitial fluid pressures. Mass balance

equation for IF is, again,

$$\boldsymbol{\nabla} \cdot (-K_{\mathrm{IF}} \boldsymbol{\nabla} \mathrm{P}_{\mathrm{IF}}) = \Gamma_F - \Gamma_{Fl}. \tag{4.5}$$

However, the source term for the seeping blood serum (Γ_F) must be modified to account for the vessels being 1-dimensional (line) sources:

$$\Gamma_F(\mathbf{x}) = \sum_{\mathrm{v}_i} \int_{\Omega_{\mathrm{v}_i}} \mathrm{d}\mathbf{s}\, \delta(\mathbf{s} - \mathbf{x})\, f_i(s)\,. \tag{4.6}$$

Here, δ is the Dirac delta function, and $\mathbf{s} \in \Omega_{\mathrm{v}_i}$ is a position vector within the 1-dimensional vascular space of the i^{th} vessel segment. Here, we define a "vessel segment" as a non-interrupted piece of vessel that links two consecutive branching points. We will use v_i to denote such vessel segments. Substituting Equation 4.6 into the mass balance equation for IF, we obtain the mass balance equation for the interstitial fluid, fed by a network of vessels:

$$\boldsymbol{\nabla} \cdot (-K_{\mathrm{IF}} \boldsymbol{\nabla} \mathrm{P}_{\mathrm{IF}}) = \sum_{\mathrm{v}_i} \int_{\Omega_{\mathrm{v}_i}} \mathrm{d}\mathbf{s}\, \delta(\mathbf{s} - \mathbf{x})\, L_{\mathrm{p}} C\, (\mathrm{P}_{\mathrm{v}} - \mathrm{P}_{\mathrm{IF}}) - \lambda_{Fl} \mathrm{P}_{\mathrm{IF}}. \tag{4.7}$$

4.2. The Finite Difference Discretization

The 3D domain of the problem is partitioned using a uniform mesh as $\mathbf{x}_i \in \Omega$. Step size for the spatial mesh, i.e., the distance between adjacent mesh points, is chosen as $h = 20$ μm for all directions. This step size was chosen in order to resolve the intercapillary distance (100–300 μm). This allows us to calculate local outward flux of interstitial fluid around the vessel walls, which may help the extravasated drug particles to leave the vicinity of the vessels and penetrate the tissue. The vascular space is discretized on the same spatial mesh. We will call the mesh points that vessels

pass through as "vessel nodes", and denote them with $\mathbf{x}_s \in \Omega_{\mathrm{v}}$. Lying on this mesh structure, vessels are allowed to make only 90° turns, form branches, and may terminate at nodes, forming "sprout tips". Branching of the vessels are only allowed to occur at mesh points, and we will call these points, "branching nodes". The remainder of the vessel nodes will be called "segment nodes".

The discretized versions of variables and parameters will be denoted with subscripts. Integer subscripts are the indices of the mesh points at which the variables are evaluated. For instance, $\mathrm{P}_i^{\mathrm{IF}} = \mathrm{P}^{\mathrm{IF}}(\mathbf{x}_i)$ denotes the IFP at the i^{th} mesh point of the 3-dimensional interstitial space. Subscripts such as $i \to j$ signify that the variable refers to the interval between the subsequent mesh points $\mathbf{x}_i$ and $\mathbf{x}_j$. For instance, $K_{s\to r}^{\mathrm{ves}}$ is flow conductivity of the vessel that lies between the adjacent vessel nodes $\mathbf{x}_s$ and $\mathbf{x}_r$. Finally, $\odot i$ denotes the set of mesh points that are adjacent to the point $\mathbf{x}_i$, either within the interstitial space or the vascular space.

4.2.1. Discretization of the Equations for Interstitial Flow

Using the discretized form of the Darcy law,

$$q_{i\to j}^{\mathrm{IF}} = -K_{i\to j}^{\mathrm{IF}} \frac{\mathrm{P}_j^{\mathrm{IF}} - \mathrm{P}_i^{\mathrm{IF}}}{h}, \tag{4.8}$$

we write the centered finite difference approximation for the mass balance equation of the interstitial fluid, Equation 4.5:

$$\frac{1}{h^2}\left[-\sum_{j\odot i} K_{i\to j}^{\mathrm{IF}} \mathrm{P}_j^{\mathrm{IF}} + \sum_{j\odot i} K_{i\to j}^{\mathrm{IF}} \mathrm{P}_i^{\mathrm{IF}}\right] = \Gamma_i^F - \Gamma_i^{Fl}, \tag{4.9}$$

which is accurate to $\mathcal{O}(h^2)$. If we assume that interstitial space is homogeneous and isotropic ($K^{\mathrm{IF}}_{i\to j} = K^{\mathrm{IF}}$), we obtain:

$$\frac{1}{h^2}\left[-K^{\mathrm{IF}}\sum_{j\odot i}\mathrm{P}^{\mathrm{IF}}_j + 6K^{\mathrm{IF}}\mathrm{P}^{\mathrm{IF}}_i\right] = \Gamma^F_i - \Gamma^{Fl}_i. \tag{4.10}$$

Since we assume lymph vessels as continuously distributed sinks, the form of Γ^{Fl}_i is simply:

$$\Gamma^{\mathrm{Fl}}_i = \lambda^{\mathrm{Fl}}_i \mathrm{P}^{\mathrm{IF}}_i, \tag{4.11}$$

such that λ^{Fl}_i will be set to zero inside the tumor, $\mathbf{x}_i \in \Omega_T$, to account for the absence of functional lymph vessels, as discussed in Section 2.7.

To discretize Γ_{F}, we first write its Taylor expansion near the mesh point $\mathbf{x}_i$:

$$\Gamma_{\mathrm{F}}(\mathbf{x}_i + \Delta\mathbf{x}) = \Gamma_{\mathrm{F}}(\mathbf{x}_i) + \boldsymbol{\nabla}\Gamma_{\mathrm{F}}|_{\mathbf{x}_i}\cdot\Delta\mathbf{x} + \mathcal{O}\left(\Delta x^2\right). \tag{4.12}$$

Then, we calculate the integral of Γ_{F} over the cubic space of dimensions $h\times h\times h$, that contains the mesh point $\mathbf{x}_i$ at center:

$$\int_{\Omega_i} \mathrm{d}^3\mathbf{x}\ \Gamma_{\mathrm{F}}\left(\mathbf{x}\right) = \Gamma_{\mathrm{F}}(\mathbf{x}_i)\ h^3 + \mathcal{O}\left(h^5\right). \tag{4.13}$$

We denote this space by Ω_i (See Figure 4.2). Dividing by h^3, we obtain an approxima-

tion for the average of $\Gamma_{\mathrm{F}}(\mathbf{x})$ on Ω_i;

$$\frac{1}{h^3}\int_{\Omega_i} \mathrm{d}^3\mathbf{x}\ \Gamma_{\mathrm{F}}(\mathbf{x}) = \Gamma_i^{\mathrm{F}} + \mathcal{O}\big(h^2\big)\,. \tag{4.14}$$

Here, substituting Equation 4.6 for $\Gamma_{\mathrm{F}}(\mathbf{x})$, we get:

$$\begin{aligned}\frac{1}{h^3}\sum_{\mathrm{v}_j}\int_{\Omega_{\mathrm{v}_j}} \mathrm{d}\mathbf{s}\, f_{\mathrm{v}_j}(s)\int_{\Omega_i} \mathrm{d}^3\mathbf{x}\ \delta(\mathbf{s}-\mathbf{x}) &= \Gamma_i^{\mathrm{F}} + \mathcal{O}\big(h^2\big)\,, &(4.15)\\ \frac{1}{h^3}\sum_{\mathrm{v}_j}\int_{\Omega_{\mathrm{v}_j}} \mathrm{d}\mathbf{s}\, f_{\mathrm{v}_j}(s)\,\mathbf{1}_{\mathbf{s}\in\Omega_i} &= \Gamma_i^{\mathrm{F}} + \mathcal{O}\big(h^2\big)\,, &(4.16)\end{aligned}$$

where $\mathbf{1}_{\mathbf{s}\in\Omega_i}$ is 1 if $\mathbf{s}\in\Omega_i$, and 0 otherwise. Rearranging, we have;

$$\Gamma_i^{\mathrm{F}} = \frac{1}{h^3}\sum_{\mathrm{v}_j}\int_{\Omega_{\mathrm{v}_j}\cap\Omega_i} \mathrm{d}\mathbf{s}\, f_{\mathrm{v}_j}(s) + \mathcal{O}\big(h^2\big)\,. \tag{4.17}$$

Note that the integral at the right, is a line integral on vessels that are contained within the cubic space, Ω_i. Since the vessels are restricted to lie on mesh points, the portions of individual vessels contained within Ω_i could only be of length $h/2$ (See Figure 4.2). We use N_i to denote the number of vessels meeting at the node i and consider three different vascular configurations around the vessel node $\mathbf{x}_i$. Case (i), there is no branching: a single vessel passes through $\mathbf{x}_i$, with a total length equal to h ($N_i = 2$). Case (ii): the number of vessels meeting at $\mathbf{x}_i$ is greater than two (for instance, the number is three in Figure 4.2), so $\mathbf{x}_i$ is a "branching node" ($N_i > 2$). Case (iii): a single vessel terminates at $\mathbf{x}_i$, forming a "sprout tip" ($N_i = 1$). For the time being, we will assume that second order variations in$f$ within Ω_i is small, and use a

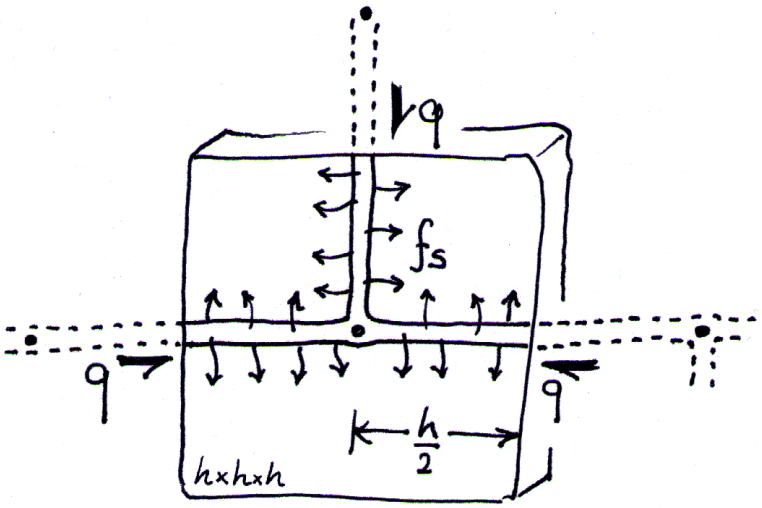

Figure 4.2. Discretization of Γ_i^{F} involves an integral on the vessels contained within the cubic space Ω_i of dimensions $h \times h \times h$.

zeroth order (rectangle) approximation for the integral in Equation 4.17:

$$\sum_{\mathrm{v}_j} \int_{\Omega_{\mathrm{v}_j} \cap \Omega_i} \mathrm{d}\mathbf{s}\, f_{\mathrm{v}_j}(s) \cong N_i \frac{h}{2} f_i. \tag{4.18}$$

In Section 4.2.4, we will assess the error introduced in this step for the simulations of physiologically realistic cases, and provide higher order approximations to the integral. With this approximation, the interstitial fluid source term becomes:

$$\Gamma_i^{\mathrm{F}} = N_i \frac{1}{2h^2} f_i. \tag{4.19}$$

Fluid extravasation rates, f_i, are discretized as:

$$f_i = L_{\mathrm{p},i} C_i \left(\mathrm{P}_i^{\mathrm{v}} - \mathrm{P}_i^{\mathrm{IF}} \right), \tag{4.20}$$

where $L_{\mathrm{p},i}$ and C_i are the hydraulic conductivity and circumference of the vessel piece(s) at node i. Substituting the above relations to Equation 4.10, we obtain a finite differ-

ence approximation to the interstitial fluid mass balance equation:

$$\frac{1}{h^2}\left[-K^{\mathrm{IF}}\sum_{j\odot i}\mathrm{P}_j^{\mathrm{IF}}+6K^{\mathrm{IF}}\mathrm{P}_i^{\mathrm{IF}}\right]=\frac{N_i}{2h^2}L_iC_i\left(\mathrm{P}_i^{\mathrm{v}}-\mathrm{P}_i^{IF}\right)-\lambda_i^{Fl}\mathrm{P}_i^{IF}. \tag{4.21}$$

4.2.2. Discretization of the Equations for Blood Flow

The net amount of blood that flows into a vascular network must balance with total fluid loss through the vessel walls. We need a mass balance for blood flow in terms of the nodal vascular pressures $\mathrm{P}_s^{\mathrm{v}}$ and the corresponding nodal interstitial pressures $\mathrm{P}_s^{\mathrm{IF}}$. First we integrate the differential mass balance equation (Equation 4.3) over the vascular space Ω_{v} within the cubic space Ω_s of the node $\mathbf{x}_s$:

$$-\int\limits_{\Omega_{\mathrm{v}}\cap\Omega_s}\mathrm{d}\mathbf{s}\,\boldsymbol{\nabla}\cdot\mathbf{q}_{\mathrm{v}}(\mathbf{s}) \;=\; \int\limits_{\Omega_{\mathrm{v}}\cap\Omega_s}\mathrm{d}\mathbf{s}\,f(\mathbf{s})\,, \tag{4.22}$$

$$-\sum_{r\odot s}q_{s\to r} \;=\; \sum_{\mathrm{v}_r}\int\limits_{\Omega_{\mathrm{v}_r}\cap\Omega_s}\mathrm{d}\mathbf{s}\,f_{\mathrm{v}_r}(s)\,, \tag{4.23}$$

$$\sum_{r\odot s}q_{r\to s} \;=\; \sum_{\mathrm{v}_r}\int\limits_{\Omega_{\mathrm{v}_r}\cap\Omega_s}\mathrm{d}\mathbf{s}\,f_{\mathrm{v}_r}(s)\,, \tag{4.24}$$

where $q_{r\to s}$ is the rate of blood flow from the neighboring vessel node r, to the central node s, calculated at the boundary of the cubic space, Ω_s (See Figure (4.2)). We discretize Equation 4.1 to approximate q:

$$q_{r\to s}=-K_{r\to s}^{\mathrm{v}}\frac{\mathrm{P}_s^{\mathrm{v}}-\mathrm{P}_r^{\mathrm{v}}}{h}. \tag{4.25}$$

Since boundary of Ω_s is at the midway between the nodes s and r, this is a centered approximation, and accurate to $\mathcal{O}(h^2)$. Using the 0^{th} order approximation[1] for the integral on vascular space, and substituting the above approximation for $q_{r\to s}$, we obtain the mass balance equation for blood serum:

$$\sum_{r\odot s} K^{\text{v}}_{r\to s}\frac{\text{P}^{\text{v}}_r-\text{P}^{\text{v}}_s}{h}=N_s\frac{h}{2}L_{\text{p},s}C_s\left(\text{P}^{\text{v}}_s-\text{P}^{\text{IF}}_s\right), \tag{4.26}$$

where $r\odot s$ indicates the set of the vessel nodes that is connected to the central node s, and N_s is the number of vessels meeting at the node s. For instance, applying the above equation to a non-branching vessel node by letting $\odot s=\{s-1,\,s+1\}$ and assuming constant flow conductivity we have:

$$\frac{K^{\text{v}}}{h}\left[\text{P}^{\text{v}}_{s-1}-2\text{P}^{\text{v}}_s+\text{P}^{\text{v}}_{s+1}\right]=hL_{\text{p},s}C_s\left(\text{P}^{\text{v}}_s-\text{P}^{IF}_s\right). \tag{4.27}$$

For the sprout tips, we have:

$$\frac{K^{\text{v}}}{h}\left[\text{P}^{\text{v}}_{s-1}-\text{P}^{\text{v}}_s\right]=\frac{h}{2}L_{\text{p},s}C_s\left(\text{P}^{\text{v}}_s-\text{P}^{\text{IF}}_s\right). \tag{4.28}$$

4.2.3. Obtaining a Numerical Solution

The finite difference form of the problem consists of mass balance equations for interstitial flow. To solve for the unknown variables P^{IF}_i and P^{v}_s, we cast the problem

[1] Given in Equation 4.18. Inspecting the Taylor expansion of $f(s)$ one notices that it is correct to $\mathcal{O}\left(h^3\right)$.

into a linear matrix equation:

$$\mathbf{A} \cdot \mathbf{x}_u = \mathbf{b}. \tag{4.29}$$

Here, $\mathbf{x}_u$ is the vector of unknowns:

$$\mathbf{x}_u = \left\{ \begin{array}{c} \mathrm{P}_0^{\mathrm{IF}} \\ \vdots \\ \mathrm{P}_i^{\mathrm{IF}} \\ \vdots \\ \mathrm{P}_{n-1}^{\mathrm{IF}} \\ \hline \mathrm{P}_0^{\mathrm{v}} \\ \vdots \\ \mathrm{P}_s^{\mathrm{v}} \\ \vdots \\ \mathrm{P}_{m-1}^{\mathrm{v}} \end{array} \right\}, \tag{4.30}$$

where, n is the number of nodes in the interstitial space, and m is the number of vessel nodes. The matrix $\mathbf{A}$ contains the coefficients of the unknown variables, arranged such that the product $\mathbf{A} \cdot \mathbf{x}_u$ produces the equations for interstitial pressures (Equation 4.10) in the top n rows, and for the vascular pressures (Equation 4.26) in the remaining m

rows. To satisfy this structure, $\mathbf{A}$ should have the form:

$$\mathbf{A} = \left[\begin{array}{ccccc|ccccc} C^{\mathrm{IF}}_{0,0} & \cdots & & & & & & & & . \\ & \ddots & & & & & . & & & \\ & \cdots & C^{\mathrm{IF}}_{i,i} & C^{\mathrm{IF}}_{i,j} & \cdots & & & C^{\mathrm{IF}}_{i,s} & & \\ & & & \ddots & & . & & . & & \\ & & & \cdots & C^{\mathrm{IF}}_{n-1,n-1} & & & & & \\ \hline & & & . & & C^{\mathrm{v}}_{0,0} & \cdots & & & \\ & . & & & & & \ddots & & & \\ & & C^{\mathrm{v}}_{s,i} & . & & & \cdots & C^{\mathrm{v}}_{s,s} & C^{\mathrm{v}}_{s,r} & \cdots \\ & & & & & & & & \ddots & \\ & . & & & & & & & \cdots & C^{\mathrm{v}}_{m-1,m-1} \end{array}\right], \quad (4.31)$$

where $C^{\mathrm{IF}}_{i,j}$'s denote the coefficients of $\mathrm{P}^{\mathrm{IF}}_j$'s in the equation for $\mathrm{P}^{\mathrm{IF}}_i$, such that $j \in \odot i$. Similarly, $C^{\mathrm{v}}_{s,r}$'s denote the coefficients of $\mathrm{P}^{\mathrm{v}}_r$'s in the equation for $\mathrm{P}^{\mathrm{v}}_s$, such that $r \in \odot s$. By inspecting $\mathbf{A}$, we see that interstitial flow and vascular flow problems are represented by the top-left $n \times n$, and bottom-right $m \times m$ portions of $\mathbf{A}$, and the coefficients $C^{\mathrm{v}}_{s,i}$'s and $C^{\mathrm{IF}}_{i,s}$'s couple these two problems. These coupling coefficients depend on the hydraulic conductivities of vessel walls. The coefficients in the equations for interstitial pressures (Equation 4.21) are:

$$C^{\mathrm{IF}}_{i,i} = \frac{6K^{\mathrm{IF}}}{h^2} + \frac{N_s}{2h^2} L_{\mathrm{p},s} C_s + \lambda^{Fl}_i \quad (4.32)$$

$$C^{\mathrm{IF}}_{i,j} = -\frac{K^{\mathrm{IF}}}{h^2} \quad (4.33)$$

$$C^{\mathrm{IF}}_{i,s} = -\frac{N_s}{2h^2} L_{\mathrm{p},s} C_s \quad (4.34)$$

where $j \in \odot i$ and s is the vessel node that lies on the interstitial node i. From Equation 4.26, we read off the coefficients for vascular pressures:

$$C^{\mathrm{v}}_{s,s} = \sum_{r \odot s} \frac{K^{\mathrm{v}}_{r \to s}}{h^2} + \frac{N_s}{2} L_{\mathrm{p},s} C_s \tag{4.35}$$

$$C^{\mathrm{v}}_{s,r} = -\frac{K^{\mathrm{v}}_{r \to s}}{h^2} \tag{4.36}$$

$$C^{\mathrm{v}}_{s,i} = -\frac{N_s}{2} L_{\mathrm{p},s} C_s \tag{4.37}$$

where $r \in \odot s$ and i is the interstitial node that is coincident with the vessel node i.

Dirichlet boundary conditions are imposed at the arterial and venal ends of the vasculature and on the boundaries of the interstitial space. Pressure variables at the boundaries, therefore, are not included in the vector of unknowns $\mathbf{x}_u$. Equation terms that contain the imposed (known) pressures, are passed to the right hand side of the equations and they make up the vector, $\mathbf{b}$. For instance, let's consider a interstitial space node, i, that is adjacent to the interstitial boundary node, b. On the boundary, the Diricihlet boundary condition, $\mathrm{P}^{\mathrm{IF}}_b = 0$, is imposed[2]. The equation for pressure at this node, $\mathrm{P}^{\mathrm{IF}}_i$ is:

$$C^{\mathrm{IF}}_{i,i} \mathrm{P}^{\mathrm{IF}}_i + \sum_{j \odot i} C^{\mathrm{IF}}_{i,j} \mathrm{P}^{\mathrm{IF}}_j + C^{\mathrm{IF}}_{i,s} \mathrm{P}^{\mathrm{v}}_s = 0. \tag{4.38}$$

We pass the term $C^{\mathrm{IF}}_{i,b} \mathrm{P}^{\mathrm{IF}}_b$ to the right hand side:

$$C^{\mathrm{IF}}_{i,i} \mathrm{P}^{\mathrm{IF}}_i + \sum_{j \odot i \neq b} C^{\mathrm{IF}}_{i,j} \mathrm{P}^{\mathrm{IF}}_j + C^{\mathrm{IF}}_{i,s} \mathrm{P}^{\mathrm{v}}_{s_i} = -C^{\mathrm{IF}}_{i,b} \mathrm{P}^{\mathrm{IF}}_b, \tag{4.39}$$

so that it belongs to the row i of the vector $\mathbf{b}$, i.e., $b_i = -C^{\mathrm{IF}}_{i,b} \mathrm{P}^{\mathrm{IF}}_b$.

[2] in accordance with the measurements of IFP in normal tissues. See Table (1.2).

Similarly, at the arterial and venous ends of the vessel network, we impose $\mathrm{P}_b^{\mathrm{v}} = \mathrm{P}^{\mathrm{art}}$ or $\mathrm{P}_b^{\mathrm{v}} = \mathrm{P}^{\mathrm{ven}}$. Then, the equation for vascular pressure at the vessel node s, that is adjacent to the boundary vessel node b is:

$$C_{s,s}^{\mathrm{v}}\mathrm{P}_s^{\mathrm{v}} + \sum_{r \odot s \neq b} C_{s,r}^{\mathrm{v}}\mathrm{P}_r^{\mathrm{v}} + C_{s,i}^{\mathrm{v}} = -C_{s,b}^{\mathrm{v}}\mathrm{P}_b^{\mathrm{v}}. \tag{4.40}$$

Finite difference formulation of the problem is thus complete. Pressure field within the interstitial space and vessel network is obtained by solving for the vector of unknowns:

$$\mathbf{x}_u = \mathbf{A}^{-1} \cdot \mathbf{b}. \tag{4.41}$$

Blood flow ($\mathbf{q}_{\mathrm{v}}$) and interstitial fluid flow ($\mathbf{q}_{\mathrm{IF}}$) could then be calculated using Equations 4.25 and (4.8), respectively.

In this study, size of the problem domain was chosen as 5 mm $\times$ 5 mm $\times$ 0.25 mm to contain a slice of a vascularized tumor spheroid. Using a mesh resolution $h = 25$ μm, the number of degrees of freedom (DOF) is $\approx$400000 and the number of elements in the matrix $\mathbf{A}$ is $\approx 16 \times 10^{10}$. Inspecting Equations 4.10 and 4.26, one notices that at most 8 coefficients in each row of $\mathbf{A}$ are non-zero. Therefore, we handle $\mathbf{A}$ as a sparse-matrix to save computer memory, and significantly speed up the matrix inverse operation.

4.2.4. Accuracy of the Rectangle Approximation for the Integral of f

On the vascular regions where there is excessive branching or excessive fluid extravasation, we would expect the 2^{nd} derivative of f to be large. In that case, using the rectangle approximation (Equation 4.18) for the integral of f by may lead to large

errors, and higher order approximations for this integral may be more suitable.

For the case of a non-branching, continuous vessel passing through the node $\mathbf{x}_i$ (case i), a centered parabolic approximation can be used:

$$\int_{s=-h/2}^{s=h/2} \mathrm{d}s\, f(s) \;=\; \frac{h}{24}\left(f_{i-1} + 22 f_i + f_{i+1}\right) + \mathcal{O}\left(h^5\right), \tag{4.42}$$

where f_i, f_{i-1} and f_{i+1} are the values on the central, and the neighboring vessel nodes. For the case of a branching node (case ii), contributions from individual vessel portions are summed up. The integrals along these $\frac{h}{2}$-long vessel portions can be calculated using one-sided trapezoidal or parabolic approximations:

$$\int_{s=0}^{s=h/2} \mathrm{d}s\, f(s) \;=\; \frac{h}{8}\left(3 f_i + f_{i+1}\right) + \mathcal{O}\left(h^3\right), \tag{4.43}$$

$$\int_{s=0}^{s=h/2} \mathrm{d}s\, f(s) \;=\; \frac{h}{24}\left(8 f_i + 5 f_{i+1} - f_{i+2}\right) + \mathcal{O}\left(h^4\right), \tag{4.44}$$

where f_i, f_{i+1} and f_{i+2} refer to the values on the central node, and the subsequent vessel nodes along a branch (at $s = h$ and $s = 2h$). These two approximations should be used also for the sprout tips (case iii), such that i is the node at the sprout tip, and $i + 1$ and $i + 2$ are the nodes before it.

As presented in the following sections, we ran drug delivery simulations using physiologically realistic parameters. Analyzing all of the numerical solutions obtained, we have calculated that rectangle approximations differed from parabolic approximations by less than 1.3%. Largest errors occurred on the vessels near the tumor boundary, and in larger tumors rather than small ones.

4.3. Modeling of Drug Transport

Having obtained the the blood flow, $\mathbf{q}_{\mathrm{v}}(\mathbf{s})$, and interstitial flow, $\mathbf{q}_{\mathrm{IF}}(\mathbf{x})$, the next step is to calculate the distribution of drug particles. For this purpose, in Chapter 3, we set up a reaction-diffusion-advection equation for the drug concentration. Here, we will follow a discrete approach and calculate the positions of individual drug particles in the blood stream and in the tissue. This will enable us to observe and compare the tissue penetration depth of the nanoparticles beyond the vessel wall, which is often limited in tumors [28, 91]. In addition, by opting for the discrete approach, we avoid the numerical instabilities that would arise from a high-Reynolds-number convection equation for the drug transport in the blood stream. The method we present here is general, although we will use it to model the transport of nanoparticles.

4.3.1. Vascular Transport

The local blood velocity within vessels has a parabolic profile:

$$v_b(r) = v_{\max}\left(1 - \frac{r^2}{r_{\mathrm{v}}^2}\right), \tag{4.45}$$

where r is the radial distance to the center line of the blood vessel, r_{v} is the vessel inner radius. Assuming that the solute moves with the local blood velocity and that its lateral position in time is uniformly distributed along the channel cross section, mean velocity of the particle will be equal to the mean fluid velocity:

$$v_{\mathrm{n}} = \tilde{v}_{\mathrm{b}} = \frac{v_{\max}}{2} = \frac{q_{\mathrm{v}}}{\pi r_{\mathrm{v}}^2}. \tag{4.46}$$

Since the dimensions of nanoparticles (0.01–0.1 μm) are much smaller than capillary diameters (~10 μm), we neglect the size exclusion effect ($\phi \approx 1$). At each computation

time step, nanoparticles will be translated by a distance of:

$$\Delta s = \frac{q_{\mathrm{v}}}{\pi r_{\mathrm{v}}^2}\Delta \mathrm{T}, \tag{4.47}$$

along the vessel. Flow rate within the vessel, q_{v}, is calculated using Equation 4.25.

In the case that the nanoparticle encounters a branching point (s), the probability that it will enter any of the connected branches, $P(s \rightarrow \mathrm{v}_i)$, is proportional to the fraction of the fluid flowing into that branch:

$$P(s \rightarrow \mathrm{v}_i) = \frac{|q^{\mathrm{v}}_{s\rightarrow i}|^+}{\sum_{j\odot s}\left|q^{\mathrm{v}}_{s\rightarrow j}\right|^+}, \tag{4.48}$$

where $|\,x\,|^+$ gives x, if $x > 0$, and zero, otherwise. This ensures that the drug particle properly enters into an outward flow channel.

4.3.2. Extravasation

At the end of each computational time step, the algorithm sweeps over each nanoparticle within the vascular network to determine if it has extravasated. This is done according to a probability assigned to each nanoparticle, $P^{\mathrm{ex}}(\Delta \mathrm{T})$, which is "the probability that the nanoparticle has extravasated in the past ΔT period of time". We assume that the lateral position of the particle within the vessel cross section changes in a chaotic manner, and therefore the process of extravasation is without memory, i.e., it is a Poisson process. Considering this, $P^{\mathrm{ex}}(\Delta \mathrm{T})$ can be calculated in relation to Poisson rates of convective ($\lambda^{\mathrm{c}}_{\mathrm{n}}$) and diffusive ($\lambda^{\mathrm{d}}_{\mathrm{n}}$) extravasation, as;

$$P^{\mathrm{ex}}(\Delta \mathrm{T}) = 1 - e^{-(\lambda^{\mathrm{c}}_{\mathrm{n}}+\lambda^{\mathrm{d}}_{\mathrm{n}})\Delta \mathrm{T}}. \tag{4.49}$$

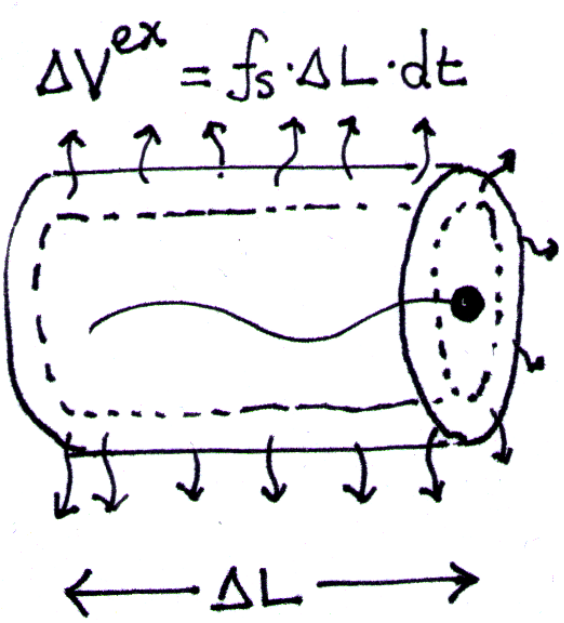

Figure 4.3. Calculation of the rate of convective extravasation: the nanoparticle may extravasate along with the leaking fluid.

To calculate the rate of convective extravasation, $\lambda_{\mathrm{n}}^{\mathrm{c}}$, let's consider a cylindrical block of vascular space through which the particle travels within an infinitesimal time, dt. Within this period of time, some portion of the fluid inside the cylinder will extravasate ($\Delta \mathrm{V}_{\mathrm{ex}}$, see Figure 4.3). The infinitesimal probability that the particle would be within the extravasated volume is equal to the ratio of the extravasated volume ($f\Delta \mathrm{L}\mathrm{d}t$) to the total fluid volume in the cylinder ($\pi r_{\mathrm{v}}^2 \Delta \mathrm{L}$). To take into account the exclusion/sieving effects due the pore walls, we multiply this probability with convective hindrance coefficient W. We now obtain the infinitesimal probability density of convective extravasation:

$$\frac{\mathrm{d}P^{\mathrm{ex}}}{\mathrm{d}t} = W \frac{f \Delta \mathrm{L}}{\pi r_{\mathrm{v}}^2 \Delta \mathrm{L}}, \tag{4.50}$$

which is equivalent to the Poisson rate of convective extravasation for the particle, $\lambda_{\mathrm{n}}^{\mathrm{c}}$. Using the relation for f (Equation 4.4), we have;

$$\lambda_{\mathrm{n}}^{\mathrm{c}} = W \frac{2 L_{\mathrm{p}} \Delta P}{r_{\mathrm{v}}}, \tag{4.51}$$

where ΔP is the effective pressure difference between the blood and the interstitial space. Note that $\lambda_{\mathrm{n}}^{\mathrm{c}}$ properly has the units of $[\frac{1}{\mathrm{T}}]$.

To calculate the rate of diffusive extravasation, $\lambda_{\mathrm{n}}^{\mathrm{d}}$, we again consider an infinitesimal cylinder of vascular space in which the nanoparticle resides. Using $c = \frac{1}{\pi r_{\mathrm{v}}^2 \Delta \mathrm{L}}$ for the concentration of the nanoparticle in the membrane diffusion equation (Equation 2.21), we obtain the rate at which the particle will diffuse from the vessel wall:

$$\lambda_{\mathrm{n}}^{\mathrm{d}} = \frac{1}{\pi r_{\mathrm{v}}^2 \Delta \mathrm{L}} P_{\mathrm{d}} 2\pi r_{\mathrm{v}} \Delta \mathrm{L}. \tag{4.52}$$

Rearranging, we have:

$$\lambda_{\mathrm{n}}^{\mathrm{d}} = \frac{2P_{\mathrm{d}}}{r_{\mathrm{v}}}. \tag{4.53}$$

Substituting the convection and diffusion rates, we obtain the probability of extravasation within one computational time step as:

$$P^{\mathrm{ex}}(\Delta \mathrm{T}) = 1 - e^{-\frac{2}{r_{\mathrm{v}}}(W L_{\mathrm{p}} \Delta P + P_{\mathrm{d}})\Delta \mathrm{T}}. \tag{4.54}$$

4.3.3. Interstitial Transport

In each computation time step, nanoparticles in the interstitial space will undergo (i) a stochastic translation due to diffusion ($\Delta \mathbf{x}_{\mathrm{d}}$), and (ii) a deterministic translation due to convective transport ($\Delta \mathbf{x}_{\mathrm{c}}$). Translation for convective transport is straightforward:

$$\Delta \mathbf{x}_{\mathrm{c}} = -\frac{K}{\phi_{\mathrm{F}}} \boldsymbol{\nabla} P \mathrm{r_f} \Delta \mathrm{T}. \tag{4.55}$$

Where r_f is the retardation coefficient for interstitial convection (See Section (2.6.2)). The probability distribution of the diffusive displacement vector is equivalent to the fundamental solution for the diffusion equation in 3-dimensions:

$$f(\mathbf{x}_d) = (4\pi D\Delta \mathrm{T})^{-3/2} e^{-\frac{x_d^2}{4D\Delta \mathrm{T}}}, \tag{4.56}$$

where D is the effective diffusion coefficient in tissue (See Section (2.6)). Note that $\Delta\mathbf{x}_d$ has a normal distribution with a standard deviation proportional to the diffusion length of the particle, $\sqrt{D\Delta \mathrm{T}}$.

The total displacement of the nanoparticle is the sum of $\Delta\mathbf{x}_c$ and the random vector $\Delta\mathbf{x}_d$.

4.3.4. Lymphatic Clearance and Biological Decay of Nanoparticles

The probability of removal at the end of a computation time step is calculated by assuming that the clearance of the nanoparticle is a Poisson process:

$$P^r = 1 - e^{-\lambda_c \Delta \mathrm{T}}, \tag{4.57}$$

where the removal rate of the nanoparticle is:

$$\lambda_c = \lambda_{Fl} \mathrm{P} + \lambda_r. \tag{4.58}$$

Here, λ_{Fl} is the lymph filtration coefficient, P is the effective interstitial fluid pressure (See Section 2.7), and λ_r is the biological decay rate of the nanoparticle.

5. RESULTS

Using the discrete model presented in Chapter 4, we have studied the blood flow, interstitial flow and drug delivery in a vascularized tumor. A grid-like tumor vascular network, that consists of arterioles, metarterioles, capillaries and venules, was computationally generated. Actual measurements of vessel diameters, inter-branching distances, and branching angles (See Section 2.1) were used to generate the tumor microvasculature. In the first set of experiments, we study how blood flow and interstitial flow differ between tumors and normal tissues. In the next set of experiments, we analyze the influence of vascular permeability on drug delivery in different tumors. Table 5.1 lists the baseline values of the parameters we have used in the simulations.

In our simulations, we distinguished tumors from the normal tissue by the structure of their vascular network, and the lack of draining lymphatics. Consistent with the measurements, tumor capillaries have larger diameters and leakier vessel walls. Interbranching distances are shorter in tumor capillaries than in normal capillaries. This causes the tumor vascular network to be slightly denser compared to normal tissues, which is usually the case for the peripheral vasculature of tumors, as discussed in Section 2.1.

5.1. Computational Domain

In this study, the computational domain consists of a tissue slice with dimensions 5 mm $\times$ 5 mm $\times$ 0.25 mm. We choose a slice, instead of a 3D cube to keep the computational time reasonable, while keeping the mesh dense enough to resolve the inter-vessel distances of ~100 μm. A single layer of grid-like vasculature lies in the middle of the slice. This computer-generated vessel network consists of two arteriole-venule pairs, each linked with 1.25 mm long metarterioles. Metarteriole lengths are chosen according to the measurements of arteriolar-venular path lengths (0.5 – 1.5 mm) by Less *et al.* [17]. Correct to the actual physiology described in Section 2.1, capillaries branch off from the metarterioles, forming the a web that penetrates the tissue. See

Table 5.1. Parameters used in the computer simulations.

Parameter	Value	Ref.
P^{+}_{art}	15 mmHg	-
P^{-}_{art}	10 mmHg	-
P^{+}_{ven}	10 mmHg	-
P^{-}_{ven}	5 mmHg	-
$\sigma\Delta\pi$	5 mmHg	[133]
d_{art}	20 μm	[17]
d_{met}	10–15 μm	[45]
d_{cap} (tumor)	10–18 μm	See Section 2.1
d_{cap} (healthy)	8–12 μm	See Section 2.1
d_{ven}	20 μm	[17]
$L_{p,art}$	1.7×10^{-10} m/mmHg·s	See Table 2.3
$L_{p,cap}$ (tumor)	265×10^{-10} m/mmHg·s	See Table 2.3
$L_{p,cap}$ (normal)	$9.8\text{–}34\ \times10^{-10}$ m/mmHg·s	See Table 2.3
$L_{p,ven}$	34×10^{-10} m/mmHg·s	See Table 2.3
IBD (core)	100μm	[47]
IBD (periphery)	50-100 μm	[47]
IBD (normal)	200 μm	See Section 2.1
θ_B	60°	[46]
L_{met}	1.25 mm	[17]
L_{tumor}	3.75–7.5 mm	-
λ_{Fl} (normal)	1×10^{-4} 1/mmHg·sec	[107]
λ_{Fl} (tumor)	0	See Section 2.7
K	4.13×10^{-12} m^2/mmHg·sec	[79]
μ	3×10^{-5} mmHg·s	[40]
λ_r	1/week	[91]

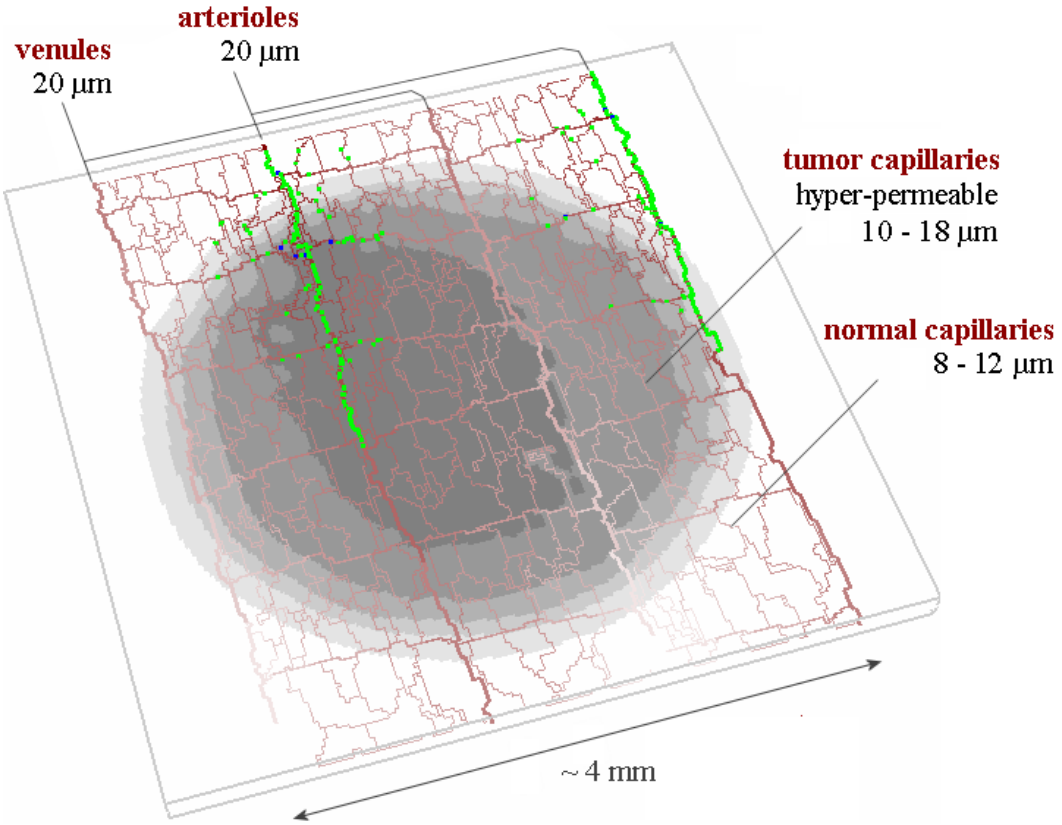

Figure 5.1. Layout of the problem domain. Red shading: vascular network. Greyscale shading: interstitial fluid pressure. Green dots: drug particles within the vessels. Blue dots: drug particles within the tissue.

Figure 5.1 for the layout of the problem domain. On the lateral boundaries, we impose the Dirichlet boundary condition, $\mathrm{P_{IF}} = 0$, consistent with measurements in healthy tissues. On the bottom and top boundaries of the domain, we impose the following boundary conditions:

$$\left.\frac{\partial}{\partial z}\mathrm{P_{IF}}(x,\,y,\,z)\right|_{z_{\mathrm{top}}} = -\left.\frac{\partial}{\partial z}\mathrm{P_{IF}}(L_x - x,\,L_y - y,\,z_{\mathrm{top}})\right|_{z_{\mathrm{top}}}, \tag{5.1}$$

$$\left.\frac{\partial}{\partial z}\mathrm{P_{IF}}(x,\,y,\,z)\right|_{z_{\mathrm{bot}}} = -\left.\frac{\partial}{\partial z}\mathrm{P_{IF}}(L_x - x,\,L_y - y,\,z_{\mathrm{top}})\right|_{z_{\mathrm{bot}}}, \tag{5.2}$$

where L_x and L_y are the dimensions of the domain. With these boundary conditions, the physical system becomes an infinite number of grid-like vessel networks stacked over each other, such that geometry of each network is a point reflection of the one beneath. These reflections avoid the asymmetry that would be caused by the vascular and arteriolar blood flows. When modeling tumor tissues, tumor parameters are assigned to

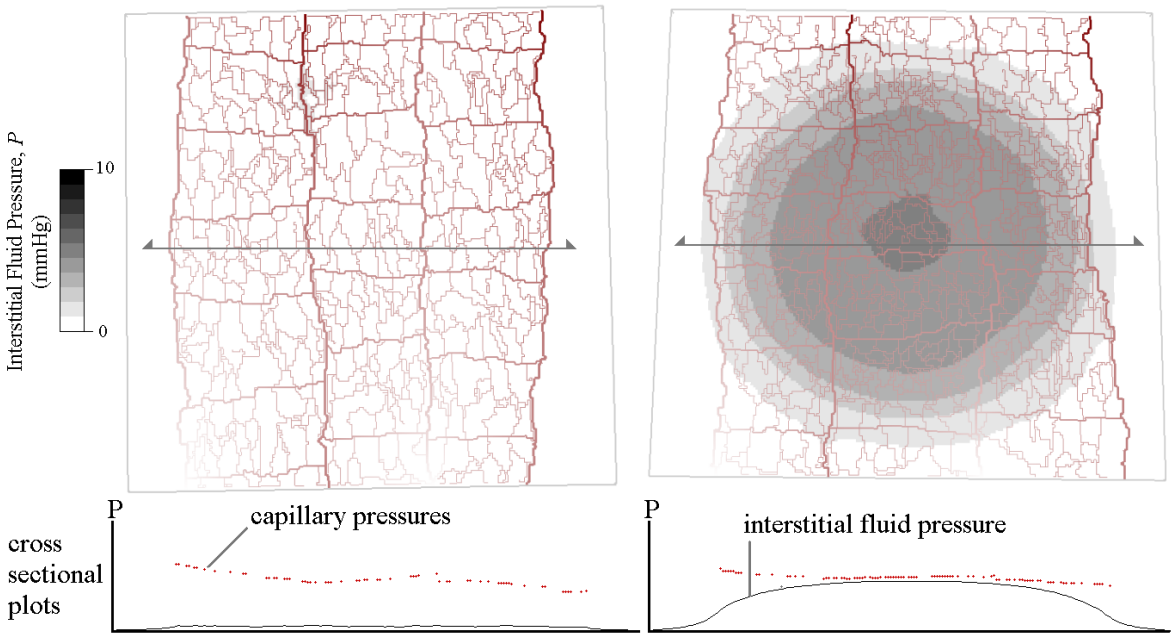

Figure 5.2. Interstitial fluid pressure was elevated in tumors (right), while it was near-zero in normal tissues (left). Bottom panels: plots over tissue cross sections. Solid line: IFP. Red dots: capillary blood pressures.

the central circular region of diameter 3.5 mm. However, because of the Neumann-like boundary conditions, this simulates the properties of a cylindrical tumor, instead of a spherical one.

5.2. Drug Distribution in Tumors vs. Normal Tissues

In agreement with the continuum model in Chapter 3, other theoretical models [21, 133], and clinical and laboratory experiments [2, 14]; our discrete model showed that interstitial fluid pressure was elevated within tumors (See Figures 1.2 and 5.2).

As a result of elevated IFP, fluid convection across the tumor vessel walls were significantly reduced. Figure 5.3 compares the distributions of transvascular pressure differences ($P_v - P_{IF}$) and transvascular convection rates (f) on the individual vessels of a normal tissue and a tumor. In this experiment, the mean values of transvascular convection rates on normal and tumor capillaries were $0.45\mu m^2/sec$ and $0.10\mu m^2/sec$, respectively. Using the method introduced in Section 4.3, we simulated the IV injection of 1000 units of convection-driven drug particles (See Figure 5.4). Due to elevated IFP,

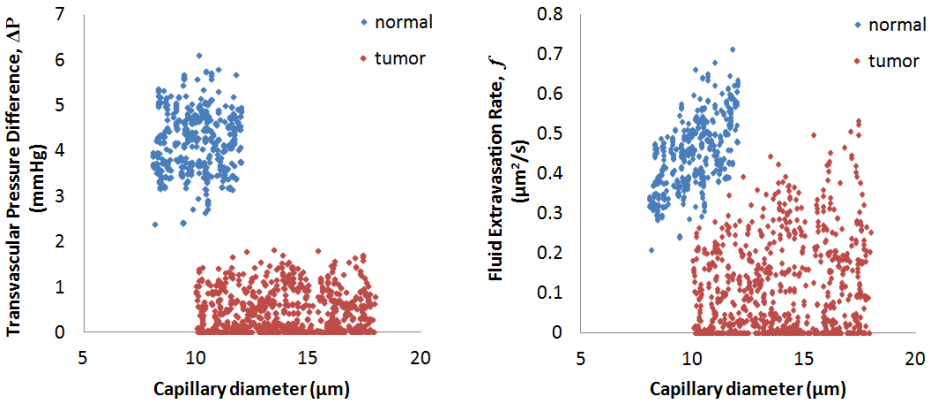

Figure 5.3. Distributions of transvascular pressure differences ($P_{\mathrm{v}} - P_{\mathrm{IF}}$) and convection rates ($f$) on the individual vessels of a normal (blue) and a tumor tissue (red). Mean extravasation rate is significantly lower in tumors (0.10 vs 0.45 $\mu\mathrm{m}^2/\mathrm{s}$).

number of particles found within the inner region of the tumor was significantly smaller than the corresponding region in healthy tissue (n=21 vs. n=62, 66% decrease). The total number of extravasated drug particles was also smaller in the tumor tissue than in the normal tissue (n=135 vs. n=166, 19% decrease). These results are in agreement with the clinical and laboratory observations that elevated IFP inhibits drug delivery in tumors [10, 134]. In particular, by using a non-invasive, in-vivo MRI technique, Hassid *et al.* [13] have simultaneously measured the IFP and the concentration profile of an IV-injected contrast agent in tumors. Our results match their observations of an elevated tumor IFP and reduced intra-tumor concentrations of blood-borne agents (See Figure 5.5). Our discrete model of drug delivery clearly demonstrates a functional link between tumor vessel leakiness, decreased transvascular convection rates and impaired drug delivery.

5.3. Blood Flow in Tumors vs. Normal Tissues

Due to the hyper-permeability of the tumor vessels, interstitial flow and blood flow is strongly coupled to each other. Baish *et al.* [135], have previously studied this phenomenon using a mathematical model of a pair of counter-current vessels embedded in the interstitium. They have proposed a dimensionless parameter, β, equal to the

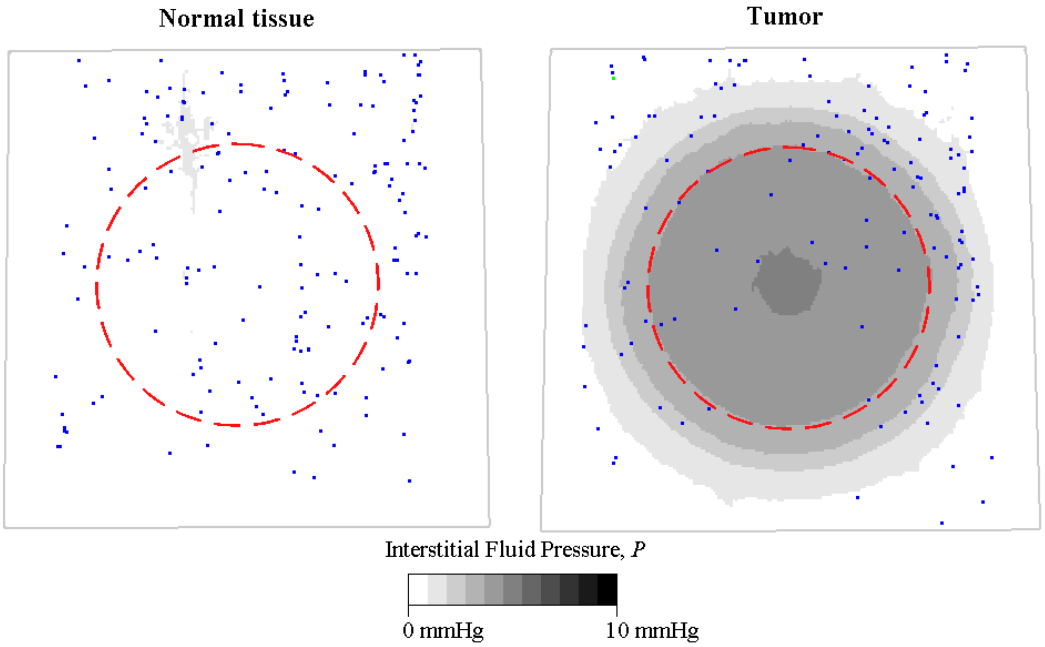

Figure 5.4. Distribution of drug particles in normal and tumor tissues 10 minutes after an IV injection of 1000 units. Red dashed line: inner region of the tumor. Blue dots: extravasated drug particles.

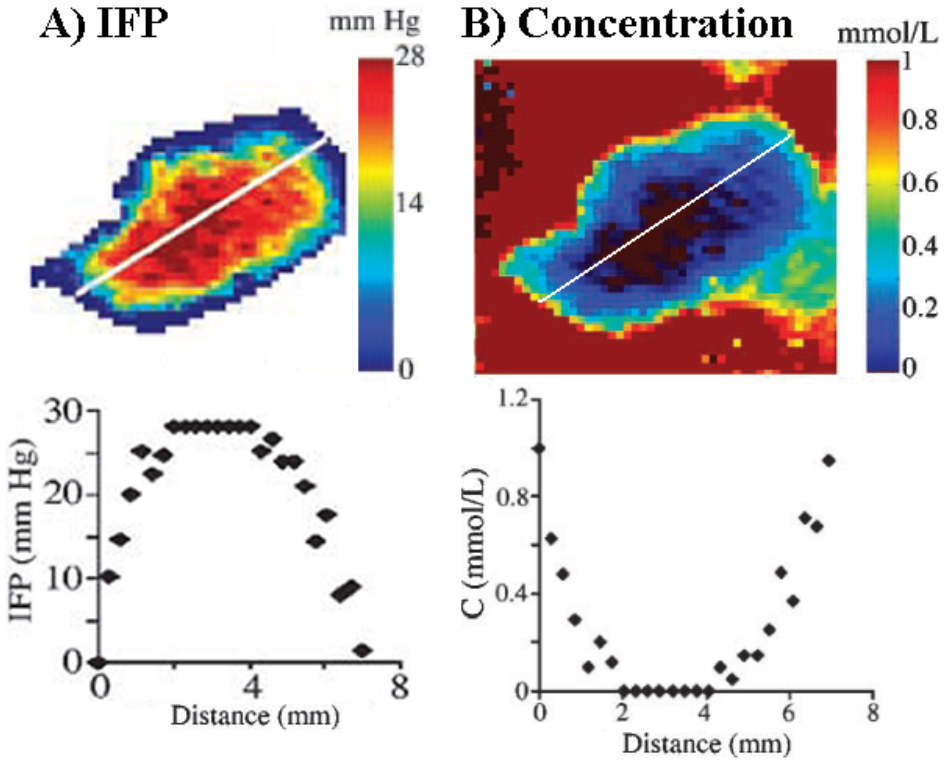

Figure 5.5. Magnetic resonance imaging of IFP and an intravenously-injected contrast agent in a human lung tumor. Reprinted from Hassid *et al.* [13]

ratio of vascular and transvascular flow resistances,

$$\beta = \frac{16\mu L_{\mathrm{p}}\mathrm{L}^2}{r_{\mathrm{v}}^3}, \tag{5.3}$$

which measures how strongly the coupling influences the vascular pressure profile. Here, L is the blood flow path length, which can be interpreted as the tumor diameter. They have shown that for large β, vascular pressure profile diverts from its normal linear shape, and shifts towards the interstitial fluid pressure profile, which is uniform over the tumor. They suggested that such coupling would increase with tumor size and with vessel wall hydraulic conductivity. By using a grid-like vessel network, we studied the blood flow in tissues that have spatial extent, and thus expanded the analysis of Baish *et al.*

We studied the influence of transvascular coupling on the blood flow pattern of a normal tissue and a 7 mm tumor. The corresponding β values for the normal and tumor tissues were 0.13 and 7.09, respectively. We observed that in the central parts of the tumor vasculature, capillary blood pressures had a flatter profile (blood pressure gradients along the vessels were lost) compared to the corresponding capillaries in the normal tissue (See Figure 5.6, top panel). Accordingly, tumor blood flow was reduced in these regions, resulting in a heterogeneous pattern of blood supply throughout the tumor (Observe blank regions in Figure 5.6, bottom-right panel). Such heterogeneity in tumor blood flow was not as pronounced in tumors smaller than 7 mm diameter (data not shown). Transvascular coupling effect is expected to be much weaker in small tumors, considering the functional dependence of β on blood flow path length, L. Our results suggest that tumor vascular hyper-permeability may be one of the reasons behind the limited and heterogeneous blood perfusion of tumors.

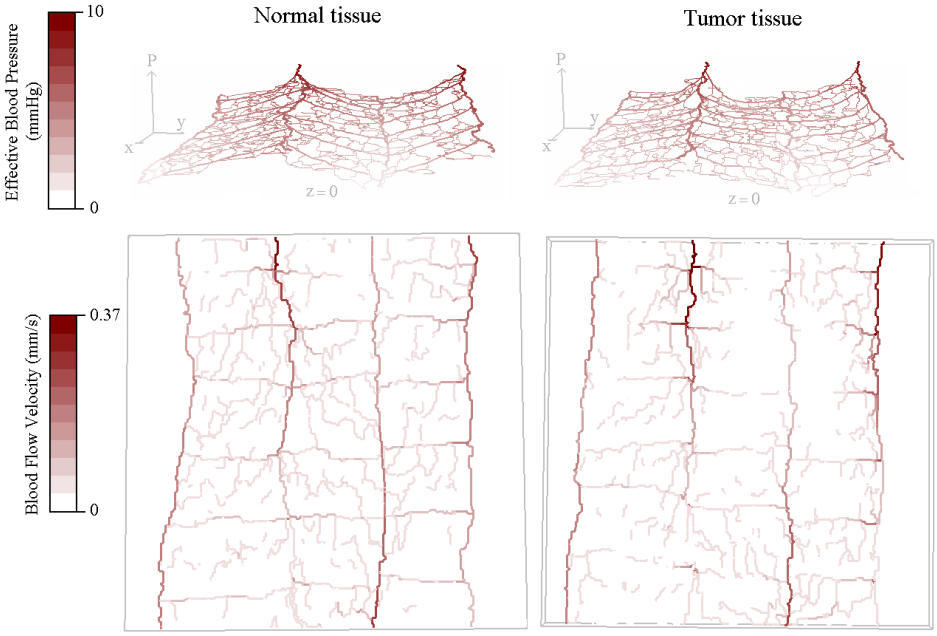

Figure 5.6. Comparison of the blood flow pattern in a tumor and a normal tissue.

5.4. Effect of Transvascular Coupling on Blood Flow and Drug Distribution in Tumors

Finally, we studied how transvascular coupling influences the tumor blood flow pattern and the spatial distribution of drug particles. We modeled the injection of 1000 units of nanoparticles in 7 mm tumors with varying levels of vascular leakiness: L_p =530, 133, 33×10^{-8} cm/mmHg-s. The corresponding β values were 7.09, 1.78, 0.44, respectively, i.e., transvascular coupling was successively decreased. In the case of hyper-permeable vasculature (L_p =530 cm/mmHg-s), drug particles extravasated predominantly near the arterioles, and did not penetrate the capillary networks where blood flow was limited (See Figure 5.7, left column). Our simulations suggest that decreasing the hydraulic conductivity of tumor vessels (L_p) suppresses the transvascular coupling, restores the abnormal tumor blood flow and provides a more uniform drug distribution (Figure 5.7, middle and right columns). In agreement with our results, laboratory experiments have shown that vascular normalization treatment via anti-angiogenic factors improves blood flow in tumors [24, 25]. We suggest that improvement of the blood supply and drug distribution within the tumor may account for the success of vascular normalization on patient outcomes.

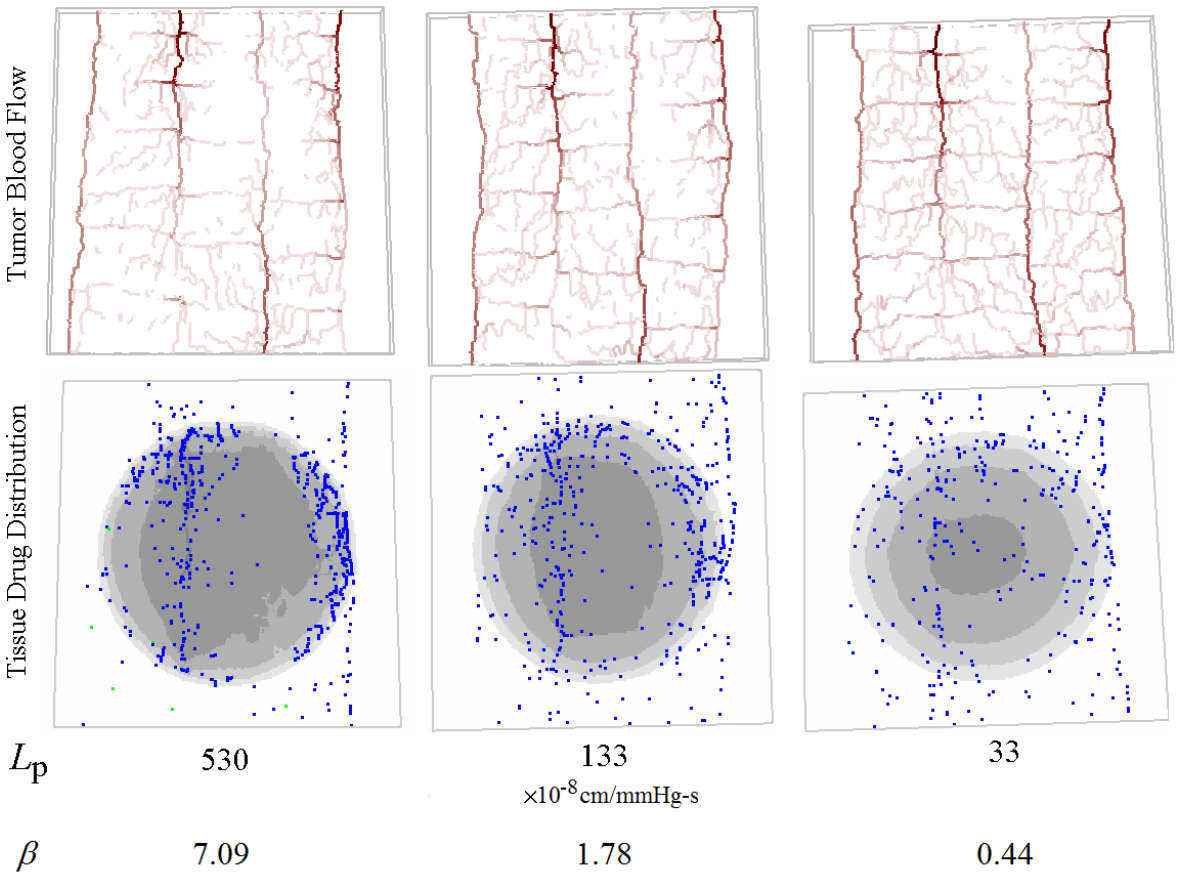

Figure 5.7. Comparison of blood flow patterns and distribution of drug particles in tumors with varying levels of vascular leakiness.

If the drug distribution within the tumor is spatially heterogeneous, during the time interval between consecutive drug injections, tumor cells that were not exposed to the drug, proliferate and replace the dead cells in the drug-exposed areas. Therefore, for an effective treatment, it is crucial that all cancer cells within the tumor are exposed to the drug. As seen in Figure 5.7, the total number of extravasated nanoparticles have decreased (from 186 to 145) with decreasing vascular leakiness. However, since the drug particles are more uniformly distributed throughout the tumor, such decrease in the total drug exposure might not be detrimental to the treatment.

5.5. Concluding Remarks

Beside its genetic properties, progression of a tumor depends also on its physical and biochemical interactions with the host tissue. The biophysical and biochemical properties of the host tissue vary among different patients and also within the same

patient, and this is one of the reasons why an established cancer treatment may be effective in one patient, and may not in another. In the past decade, mathematical models of tumor growth and tumor drug delivery have been increasingly used to study how the physical and biochemical environment of the host tissue influences the progression and treatment of cancer.

In this thesis we have used mathematical modeling to study the problem of drug delivery in solid tumors. It is well known that the leakiness of tumor blood vessels results in elevated interstitial fluid pressure and poses a barrier to drug delivery. We have studied this seemingly paradoxical phenomenon by inspecting the transvascular pressure gradients and extravasation rates in tumor vessels. Interestingly, extravasation rates in tumors are 4-5 times smaller than in normal tissues, although tumor vessels are hyper-permeable.

Several clinical trials [114–122] and laboratory experiments [23, 24, 108–113] have shown that vascular normalization treatment may improve drug delivery in some types of cancers. However, mechanisms behind such improvement are not yet fully understood. In Chapter 3, we have studied how vascular normalization treament may improve drug delivery by modifying the interstitial fluid pressure and interstitial fluid flow. Interestingly, decreasing the vascular hydraulic conductivity or vessel density of tumors (two well known effects of anti-angiogenic factors) may increase the convective extravasation of drugs in the tumor tissue, and also provides a more uniform drug distribution. We have shown that such improvement in drug delivery may depend on tumor size.

It is well known that blood supply is impaired in tumors, and this leads to heterogeneous drug delivery and hypoxia – both undesired conditions for cancer treatment. There are several reasons behind the impaired blood flow of tumors, such as increased geometric resistance and heterogeneous vascularization. By studying the transvascular coupling of blood flow and interstitial fluid flow, we have observed that leakiness of tumor vessels may lead to impaired blood flow and heterogeneous drug delivery in tumors. We have observed that decreasing the hydraulic conductivity of tumor vessels, increased

the blood flow in tumor capillary networks, and provided a more uniform drug distribution. Pre-treatment of patients with anti-angiogenic agents (vascular normalization treatment) is known to decrease hydraulic conductivities of tumor vessels. We suggest that improving the tumor blood flow by supressing the transvascular coupling may be one of the mechanisms behind the success of vascular normalization pre-treatment in chemotherapy patients.

REFERENCES

1. Rutkowski, J. M. and M. A. Swartz, "A Driving Force for Change: Interstitial Flow as a Morphoregulator", *Trends in Cell Biology*, Vol. 17, No. 1, pp. 44–50, 2007.

2. Boucher, Y., L. T. Baxter and R. K. Jain, "Interstitial Pressure Gradients in Tissue-Isolated and Subcutaneous Tumors: Implications for Therapy", *Cancer Research*, Vol. 50, No. 15, pp. 4478–84, 1990.

3. Alexis, F., E. M. Pridgen, R. Langer and O. C. Farokhzad, "Nanoparticle Technologies for Cancer Therapy", *Handbook of Experimental Pharmacology*, Vol. 197, pp. 55–86, 2010.

4. Martini, F., M. J. Timmons and R. B. Tallitsch, *Human Anatomy*, 6th ed., Pearson/Benjamin Cummings, 2006.

5. Konerding, M. A., E. Fait and A. Gaumann, "3D Microvascular Architecture of Pre-Cancerous Lesions and Invasive Carcinomas of the Colon", *British Journal of Cancer*, Vol. 84, No. 10, pp. 1354–62, 2001.

6. Konerding, M. A., W. Malkusch, B. Klapthor, C. Van Ackern, E. Fait, S. A. Hill, C. Parkins, D. J. Chaplin, M. Presta and J. Denekamp, "Evidence for Characteristic Vascular Patterns in Solid Tumours: Quantitative Studies Using Corrosion Casts", *British Journal of Cancer*, Vol. 80, No. 5-6, pp. 724–32, 1999.

7. Yuan, F., H. A. Salehi, Y. Boucher, U. S. Vasthare, R. F. Tuma and R. K. Jain, "Vascular Permeability and Microcirculation of Gliomas and Mammary Carcinomas Transplanted in Rat and Mouse Cranial Windows", *Cancer Research*, Vol. 54, No. 17, pp. 4564–8, 1994.

8. Esper, R. J., R. A. Nordaby, J. O. Vilariño, A. Paragano, J. L. Cacharrón and

R. A. Machado, "Endothelial Dysfunction: a Comprehensive Appraisal", *Cardiovascular Diabetology*, Vol. 5, p. 4, 2006.

9. Chauhan, V. P., T. Stylianopoulos, J. D. Martin, Z. Popović, O. Chen, W. S. Kamoun, M. G. Bawendi, D. Fukumura and R. K. Jain, "Normalization of Tumour Blood Vessels Improves the Delivery of Nanomedicines in a Size-Dependent Manner", *Nature Nanotechnology*, Vol. 7, No. 6, pp. 383–8, 2012.

10. Jain, R. K. and T. Stylianopoulos, "Delivering Nanomedicine to Solid Tumors", *Nature Reviews. Clinical Oncology*, Vol. 7, No. 11, pp. 653–64, 2010.

11. Nugent, L. J. and R. K. Jain, "Extravascular Diffusion in Normal and Neoplastic Tissues", *Cancer Research*, Vol. 44, No. 1, pp. 238–44, 1984.

12. Leu, A. J., D. A. Berk, A. Lymboussaki, K. Alitalo and R. K. Jain, "Absence of Functional Lymphatics Within a Murine Sarcoma: a Molecular and Functional Evaluation", *Cancer Research*, Vol. 60, No. 16, pp. 4324–7, 2000.

13. Hassid, Y., E. Furman-Haran, R. Margalit, R. Eilam and H. Degani, "Noninvasive Magnetic Resonance Imaging of Transport and Interstitial Fluid Pressure in Ectopic Human Lung Tumors", *Cancer Research*, Vol. 66, No. 8, pp. 4159–66, 2006.

14. Jain, R. K., R. T. Tong and L. L. Munn, "Effect of Vascular Normalization by Antiangiogenic Therapy on Interstitial Hypertension, Peritumor Edema, and Lymphatic Metastasis: Insights From a Mathematical Model", *Cancer Research*, Vol. 67, No. 6, pp. 2729–35, 2007.

15. Jain, R. K., "Physiological Barriers to Delivery of Monoclonal Antibodies and Other Macromolecules in Tumors", *Cancer Research*, Vol. 50, No. 3 Suppl, pp. 814S–819S, 1990.

16. Baish, J. W., Y. Gazit, D. A. Berk, M. Nozue, L. T. Baxter and R. K. Jain, "Role

of Tumor Vascular Architecture in Nutrient and Drug Delivery: An Invasion Percolation-Based Network Model", *Microvascular Research*, Vol. 51, No. 3, pp. 327–46, 1996.

17. Less, J. R., T. C. Skalak, E. M. Sevick and R. K. Jain, "Microvascular Architecture in a Mammary Carcinoma: Branching Patterns and Vessel Dimensions", *Cancer Research*, Vol. 51, No. 1, pp. 265–73, 1991.

18. Jain, R. K., "Normalization of Tumor Vasculature: An Emerging Concept in Antiangiogenic Therapy", *Science*, Vol. 307, No. 5706, pp. 58–62, 2005.

19. Boucher, Y. and R. K. Jain, "Microvascular Pressure Is the Principal Driving Force for Interstitial Hypertension in Solid Tumors: Implications for Vascular Collapse", *Cancer Research*, Vol. 52, No. 18, pp. 5110–4, 1992.

20. Dafni, H., T. Israely, Z. M. Bhujwalla, L. E. Benjamin and M. Neeman, "Overexpression of Vascular Endothelial Growth Factor 165 Drives Peritumor Interstitial Convection and Induces Lymphatic Drain: Magnetic Resonance Imaging, Confocal Microscopy, and Histological Tracking of Triple-Labeled Albumin", *Cancer Research*, Vol. 62, No. 22, pp. 6731–6739, 2002.

21. Jain, R. K. and L. T. Baxter, "Mechanisms of Heterogeneous Distribution of Monoclonal Antibodies and Other Macromolecules in Tumors: Significance of Elevated Interstitial Pressure", *Cancer Research*, Vol. 48, No. 24 Pt 1, pp. 7022–32, 1988.

22. Goel, S., D. G. Duda, L. Xu, L. L. Munn, Y. Boucher, D. Fukumura and R. K. Jain, "Normalization of the Vasculature for Treatment of Cancer and Other Diseases", *Physiological Reviews*, Vol. 91, No. 3, pp. 1071–121, 2011.

23. Tong, R. T., Y. Boucher, S. V. Kozin, F. Winkler, D. J. Hicklin and R. K. Jain, "Vascular Normalization by Vascular Endothelial Growth Factor Receptor 2 Blockade Induces a Pressure Gradient Across the Vasculature and Improves Drug

Penetration in Tumors", *Cancer Research*, Vol. 64, No. 11, pp. 3731–6, 2004.

24. Dickson, P. V., J. B. Hamner, T. L. Sims, C. H. Fraga, C. Y. C. Ng, S. Rajasekeran, N. L. Hagedorn, M. B. Mccarville, C. F. Stewart and A. M. Davidoff, "Bevacizumab-Induced Transient Remodeling of the Vasculature in Neuroblastoma Xenografts Results in Improved Delivery and Efficacy of Systemically Administered Chemotherapy", *Clinical Cancer Research*, Vol. 13, No. 13, pp. 3942–50, 2007.

25. Qayum, N., R. J. Muschel, J. H. Im, L. Balathasan, C. J. Koch, S. Patel, W. G. Mckenna and E. J. Bernhard, "Tumor Vascular Changes Mediated by Inhibition of Oncogenic Signaling", *Cancer Research*, Vol. 69, No. 15, pp. 6347–54, 2009.

26. Winkler, F., S. V. Kozin, R. T. Tong, S.-S. Chae, M. F. Booth, I. Garkavtsev, L. Xu, D. J. Hicklin, D. Fukumura, E. Di Tomaso, L. L. Munn and R. K. Jain, "Kinetics of Vascular Normalization by Vegfr2 Blockade Governs Brain Tumor Response to Radiation: Role of Oxygenation, Angiopoietin-1, and Matrix Metalloproteinases", *Cancer Cell*, Vol. 6, No. 6, pp. 553–63, 2004.

27. Sarin, H., "Physiologic Upper Limits of Pore Size of Different Blood Capillary Types and Another Perspective on the Dual Pore Theory of Microvascular Permeability", *Journal of Angiogenesis Research*, Vol. 2, p. 14, 2010.

28. Dreher, M. R., W. Liu, C. R. Michelich, M. W. Dewhirst, F. Yuan and A. Chilkoti, "Tumor Vascular Permeability, Accumulation, and Penetration of Macromolecular Drug Carriers", *Journal of the National Cancer Institute*, Vol. 98, No. 5, pp. 335–44, 2006.

29. Perrault, S. D., C. Walkey, T. Jennings, H. C. Fischer and W. C. W. Chan, "Mediating Tumor Targeting Efficiency of Nanoparticles Through Design", *Nano Letters*, Vol. 9, No. 5, pp. 1909–15, 2009.

30. Wu, N. Z., D. Da, T. L. Rudoll, D. Needham, A. R. Whorton and M. W. Dewhirst,

"Increased Microvascular Permeability Contributes to Preferential Accumulation of Stealth Liposomes in Tumor Tissue", *Cancer Research*, Vol. 53, No. 16, pp. 3765–70, 1993.

31. Sherwood, L., *Human Physiology: From Cells to Systems*, 7th ed., Brooks/Cole, Cengage Learning, 2010.

32. Klein, B., W. Kuschinsky, H. Schröck and F. Vetterlein, "Interdependency of Local Capillary Density, Blood Flow, and Metabolism in Rat Brains", *The American Journal of Physiology*, Vol. 251, No. 6 Pt 2, pp. H1333–40, 1986.

33. Vajkoczy, P., M. Farhadi, A. Gaumann, R. Heidenreich, R. Erber, A. Wunder, J. C. Tonn, M. D. Menger and G. Breier, "Microtumor Growth Initiates Angiogenic Sprouting With Simultaneous Expression of Vegf, Vegf Receptor-2, and Angiopoietin-2", *The Journal of Clinical Investigation*, Vol. 109, No. 6, pp. 777–85, 2002.

34. Eikenberry, S., "A Tumor Cord Model for Doxorubicin Delivery and Dose Optimization in Solid Tumors", *Theoretical Biology & Medical Modelling*, Vol. 6, p. 16, 2009.

35. Mcguire, B. J. and T. W. Secomb, "Estimation of Capillary Density in Human Skeletal Muscle Based on Maximal Oxygen Consumption Rates", *American Journal of Physiology. Heart and Circulatory Physiology*, Vol. 285, No. 6, pp. H2382–91, 2003.

36. Lillioja, S., A. A. Young, C. L. Culter, J. L. Ivy, W. G. Abbott, J. K. Zawadzki, H. Yki-Järvinen, L. Christin, T. W. Secomb and C. Bogardus, "Skeletal Muscle Capillary Density and Fiber Type Are Possible Determinants of in Vivo Insulin Resistance in Man", *The Journal of Clinical Investigation*, Vol. 80, No. 2, pp. 415–24, 1987.

37. Jain, R. K., "Transport of Molecules Across Tumor Vasculature", *Cancer Metas-*

tasis Reviews, Vol. 6, No. 4, pp. 559–93, 1987.

38. Yuan, F., "Time-Dependent Vascular Regression and Permeability Changes in Established Human Tumor Xenografts Induced by An Anti-Vascular Endothelial Growth Factor/vascular Permeability Factor Antibody", *Proceedings of the National Academy of Sciences*, Vol. 93, No. 25, pp. 14765–14770, 1996.

39. Galluzzo, M., S. Pennacchietti, S. Rosano, P. M. Comoglio and P. Michieli, "Prevention of Hypoxia by Myoglobin Expression in Human Tumor Cells Promotes Differentiation and Inhibits Metastasis", *The Journal of Clinical Investigation*, Vol. 119, No. 4, pp. 865–75, 2009.

40. Jain, R. K., "Determinants of Tumor Blood Flow: a Review", *Cancer Research*, Vol. 48, No. 10, pp. 2641–58, 1988.

41. Vogel, A. W., "Vascular Surface Area, Length and Volume/mm3 of Tumor Tissue-Sarcoma 180, 72J Mammary Adenocarcinoma", *Proceedings of American Association for Cancer Research*, Vol. 4, p. 70, 1963.

42. Awwad, H. K., M. El Naggar, N. Mocktar and M. Barsoum, "Intercapillary Distance Measurement as An Indicator of Hypoxia in Carcinoma of the Cervix Uteri", *International Journal of Radiation Oncology, Biology, Physics*, Vol. 12, No. 8, pp. 1329–33, 1986.

43. Tarbell, J. M., "Mass Transport in Arteries and the Localization of Atherosclerosis", *Annual Review of Biomedical Engineering*, Vol. 5, pp. 79–118, 2003.

44. Feher, J. J., *Quantitative Human Physiology: An Introduction*, 1st ed., Elsevier Science, Waltham, MA, 2012.

45. Jr., R. A. F., *Nanomedicine, Volume I: Basic Capabilities*, Landes Bioscience, Georgetown, TX, 1999.

46. Lang, S., B. Müller, M. D. Dominietto, P. C. Cattin, I. Zanette, T. Weitkamp and S. E. Hieber, "Three-Dimensional Quantification of Capillary Networks in Healthy and Cancerous Tissues of Two Mice", *Microvascular Research*, Vol. 84, No. 3, pp. 314–22, 2012.

47. Folarin, A. A., M. A. Konerding, J. Timonen, S. Nagl and R. B. Pedley, "Three-Dimensional Analysis of Tumour Vascular Corrosion Casts Using Stereoimaging and Micro-Computed Tomography", *Microvascular Research*, Vol. 80, No. 1, pp. 89–98, 2010.

48. Ackermann, M., B. A. Morse, V. Delventhal, I. M. Carvajal and M. A. Konerding, "Anti-Vegfr2 and Anti-Igf-1R-Adnectins Inhibit Ewing's Sarcoma A673-Xenograft Growth and Normalize Tumor Vascular Architecture", *Angiogenesis*, Vol. 15, No. 4, pp. 685–95, 2012.

49. Gimbrone, M. A., "Tumor Dormancy in Vivo by Prevention of Neovascularization", *Journal of Experimental Medicine*, Vol. 136, No. 2, pp. 261–276, 1972.

50. Gillies, R. J., P. A. Schornack, T. W. Secomb and N. Raghunand, "Causes and Effects of Heterogeneous Perfusion in Tumors", *Neoplasia*, Vol. 1, No. 3, pp. 197–207, 1999.

51. Narang, A. S. and S. Varia, "Role of Tumor Vascular Architecture in Drug Delivery", *Advanced Drug Delivery Reviews*, Vol. 63, No. 8, pp. 640–58, 2011.

52. Bates, D. O. and F. E. Curry, "Vascular Endothelial Growth Factor Increases Hydraulic Conductivity of Isolated Perfused Microvessels", *The American Journal of Physiology*, Vol. 271, No. 6 Pt 2, pp. H2520–8, 1996.

53. Cogger, V. C., I. M. Arias, A. Warren, A. C. Mcmahon, D. L. Kiss, V. M. Avery and D. G. Le Couteur, "The Response of Fenestrations, Actin, and Caveolin-1 to Vascular Endothelial Growth Factor in Sk Hep1 Cells", *American Journal of Physiology. Gastrointestinal and Liver Physiology*, Vol. 295, No. 1, pp. G137–G145,

2008.

54. Esser, S., "Vascular Endothelial Growth Factor Induces Endothelial Fenestrations in Vitro", *The Journal of Cell Biology*, Vol. 140, No. 4, pp. 947–959, 1998.

55. Esser, S., M. G. Lampugnani, M. Corada, E. Dejana and W. Risau, "Vascular Endothelial Growth Factor Induces Ve-Cadherin Tyrosine Phosphorylation in Endothelial Cells", *Journal of Cell Science*, Vol. 111 (Pt 1, pp. 1853–65, 1998.

56. Less, J. R., M. C. Posner, T. C. Skalak, N. Wolmark and R. K. Jain, "Geometric Resistance and Microvascular Network Architecture of Human Colorectal Carcinoma", *Microcirculation*, Vol. 4, No. 1, pp. 25–33, 1997.

57. Roberts, W. G. and G. E. Palade, "Neovasculature Induced by Vascular Endothelial Growth Factor Is Fenestrated", *Cancer Research*, Vol. 57, No. 4, pp. 765–72, 1997.

58. Hobbs, S. K., W. L. Monsky, F. Yuan, W. G. Roberts, L. Griffith, V. P. Torchilin and R. K. Jain, "Regulation of Transport Pathways in Tumor Vessels: Role of Tumor Type and Microenvironment", *Proceedings of the National Academy of Sciences of the United States of America*, Vol. 95, No. 8, pp. 4607–12, 1998.

59. Hashizume, H., P. Baluk, S. Morikawa, J. W. Mclean, G. Thurston, S. Roberge, R. K. Jain and D. M. Mcdonald, "Openings Between Defective Endothelial Cells Explain Tumor Vessel Leakiness", *The American Journal of Pathology*, Vol. 156, No. 4, pp. 1363–80, 2000.

60. Banker, G. S., J. Siepmann and C. Rhodes, *Modern Pharmaceutics*, 4th ed., Taylor & Francis, 2002.

61. Safar, M. E., "Peripheral Pulse Pressure, Large Arteries, and Microvessels", *Hypertension*, Vol. 44, No. 2, pp. 121–2, 2004.

62. Gessner, R. C., S. R. Aylward and P. A. Dayton, "Mapping Microvasculature With Acoustic Angiography Yields Quantifiable Differences Between Healthy and Tumor-Bearing Tissue Volumes in a Rodent Model", *Radiology*, Vol. 264, No. 3, pp. 733–40, 2012.

63. Drake-Holland, A. J. and M. I. Noble, "The Important New Drug Target in Cardiovascular Medicine–The Vascular Glycocalyx", *Cardiovascular & Hematological Disorders Drug Targets*, Vol. 9, No. 2, pp. 118–23, 2009.

64. Van Den Berg, B. M., M. Nieuwdorp, E. S. G. Stroes and H. Vink, "Glycocalyx and Endothelial (Dys) Function: From Mice to Men", *Pharmacological Reports : Pr*, Vol. 58 Suppl, pp. 75–80, 2006.

65. Michel, C. C. and F. E. Curry, "Microvascular Permeability", *Physiological Reviews*, Vol. 79, No. 3, pp. 703–61, 1999.

66. Yuan, F., M. Dellian, D. Fukumura, M. Leunig, D. A. Berk, V. P. Torchilin and R. K. Jain, "Vascular Permeability in a Human Tumor Xenograft: Molecular Size Dependence and Cutoff Size", *Cancer Research*, Vol. 55, No. 17, pp. 3752–6, 1995.

67. Sevick, E. M. and R. K. Jain, "Measurement of Capillary Filtration Coefficient in a Solid Tumor", *Cancer Research*, Vol. 51, No. 4, pp. 1352–5, 1991.

68. Phillips, C. G., K. H. Parker and W. Wang, "A Model for Flow Through Discontinuities in the Tight Junction of the Endothelial Intercellular Cleft", *Bulletin of Mathematical Biology*, Vol. 56, No. 4, pp. 723–41, 1994.

69. Rippe, B. and B. Haraldsson, "Capillary Permeability in Rat Hindquarters as Determined by Estimations of Capillary Reflection Coefficients", *Acta Physiologica Scandinavica*, Vol. 127, No. 3, pp. 289–303, 1986.

70. Curry, F. E. and J. FrøKjaer-Jensen, "Water Flow Across the Walls of Single Muscle Capillaries in the Frog, Rana Pipiens", *The Journal of Physiology*, Vol.

350, pp. 293–307, 1984.

71. Meyer, D. J. and V. H. Huxley, "Differential Sensitivity of Exchange Vessel Hydraulic Conductivity to Atrial Natriuretic Peptide", *The American Journal of Physiology*, Vol. 258, No. 2 Pt 2, pp. H521–8, 1990.

72. Michel, C. C., "Capillary Permeability and How It May Change", *The Journal of Physiology*, Vol. 404, pp. 1–29, 1988.

73. Victorino, G. P., D. H. Wisner and V. L. Tucker, "Basal Release of Endothelin-1 and the Influence of the Etb Receptor on Single Vessel Hydraulic Permeability", *The Journal of Trauma*, Vol. 49, No. 2, pp. 314–9, 2000.

74. Rumbaut, R. E., J. Wang and V. H. Huxley, "Differential Effects of L-Name on Rat Venular Hydraulic Conductivity", *American Journal of Physiology. Heart and Circulatory Physiology*, Vol. 279, No. 4, pp. H2017–23, 2000.

75. Bhattacharya, J., "Hydraulic Conductivity of Lung Venules Determined by Split-Drop Technique", *Journal of Applied Physiology*, Vol. 64, No. 6, pp. 2562–7, 1988.

76. Kimura, M., H. H. Dietrich, V. H. Huxley, D. R. Reichner and R. G. Dacey, "Measurement of Hydraulic Conductivity in Isolated Arterioles of Rat Brain Cortex", *The American Journal of Physiology*, Vol. 264, No. 6 Pt 2, pp. H1788–97, 1993.

77. Rippe, B. and B. Haraldsson, "Transport of Macromolecules Across Microvascular Walls: the Two-Pore Theory", *Physiological Reviews*, Vol. 74, No. 1, pp. 163–219, 1994.

78. Netti, P. A., D. A. Berk, M. A. Swartz, A. J. Grodzinsky and R. K. Jain, "Role of Extracellular Matrix Assembly in Interstitial Transport in Solid Tumors", *Cancer Research*, Vol. 60, No. 9, pp. 2497–503, 2000.

79. Swabb, E. A., J. Wei and P. M. Gullino, "Diffusion and Convection in Normal

and Neoplastic Tissues", *Cancer Research*, Vol. 34, No. 10, pp. 2814–22, 1974.

80. Fahlgren, A., L. Johansson, U. Edlund and P. Aspenberg, "Direct Ex Vivo Measurement of the Fluid Permeability of Loose Scar Tissue", *Acta of Bioengineering and Biomechanics / Wroclaw University of Technology*, Vol. 14, No. 2, pp. 47–51, 2012.

81. Mow, V. C., S. C. Kuei, W. M. Lai and C. G. Armstrong, "Biphasic Creep and Stress Relaxation of Articular Cartilage in Compression? Theory and Experiments", *Journal of Biomechanical Engineering*, Vol. 102, No. 1, pp. 73–84, 1980.

82. Zhang, X. Y., J. Luck, M. W. Dewhirst and F. Yuan, "Interstitial Hydraulic Conductivity in a Fibrosarcoma", *American Journal of Physiology. Heart and Circulatory Physiology*, Vol. 279, No. 6, pp. H2726–34, 2000.

83. Swartz, M. A., A. Kaipainen, P. A. Netti, C. Brekken, Y. Boucher, A. J. Grodzinsky and R. K. Jain, "Mechanics of Interstitial-Lymphatic Fluid Transport: Theoretical Foundation and Experimental Validation", *Journal of Biomechanics*, Vol. 32, No. 12, pp. 1297–307, 1999.

84. Périé, D., J. C. Iatridis, C. N. Demers, T. Goswami, G. Beaudoin, F. Mwale and J. Antoniou, "Assessment of Compressive Modulus, Hydraulic Permeability and Matrix Content of Trypsin-Treated Nucleus Pulposus Using Quantitative Mri", *Journal of Biomechanics*, Vol. 39, No. 8, pp. 1392–400, 2006.

85. Rutkowski, J. M. and M. A. Swartz, *Molecular and Mechanical Regulators of Lymphatic Biology*, Ph.D. Thesis, ÉCole Polytechnique Fédérale de Lausanne, 2008.

86. Boucher, Y., C. Brekken, P. A. Netti, L. T. Baxter and R. K. Jain, "Intratumoral Infusion of Fluid: Estimation of Hydraulic Conductivity and Implications for the Delivery of Therapeutic Agents", *British Journal of Cancer*, Vol. 78, No. 11, pp. 1442–8, 1998.

87. Levick, J. R., "Flow Through Interstitium and Other Fibrous Matrices", *Quarterly Journal of Experimental Physiology (Cambridge, England)*, Vol. 72, No. 4, pp. 409–37, 1987.

88. Jain, R. K., "Transport of Molecules in the Tumor Interstitium: a Review", *Cancer Research*, Vol. 47, No. 12, pp. 3039–51, 1987.

89. Aukland, K. and R. K. Reed, "Interstitial-Lymphatic Mechanisms in the Control of Extracellular Fluid Volume", *Physiological Reviews*, Vol. 73, No. 1, pp. 1–78, 1993.

90. Schultz, J. S., R. Valentine and C. Y. Choi, "Reflection Coefficients of Homopore Membranes: Effect of Molecular Size and Configuration", *The Journal of General Physiology*, Vol. 73, No. 1, pp. 49–60, 1979.

91. Yuan, F., M. Leunig, S. K. Huang, D. A. Berk, D. Papahadjopoulos and R. K. Jain, "Microvascular Permeability and Interstitial Penetration of Sterically Stabilized (Stealth) Liposomes in a Human Tumor Xenograft", *Cancer Research*, Vol. 54, No. 13, pp. 3352–6, 1994.

92. Gerlowski, L. E. and R. K. Jain, "Microvascular Permeability of Normal and Neoplastic Tissues", *Microvascular Research*, Vol. 31, No. 3, pp. 288–305, 1986.

93. Renkin, E. M., "Filtration, Diffusion, and Molecular Sieving Through Porous Cellulose Membranes", *The Journal of General Physiology*, Vol. 38, No. 2, pp. 225–43, 1954.

94. Pluen, A., Y. Boucher, S. Ramanujan, T. D. Mckee, T. Gohongi, E. Di Tomaso, E. B. Brown, Y. Izumi, R. B. Campbell, D. A. Berk and R. K. Jain, "Role of Tumor-Host Interactions in Interstitial Diffusion of Macromolecules: Cranial Vs. Subcutaneous Tumors", *Proceedings of the National Academy of Sciences of the United States of America*, Vol. 98, No. 8, pp. 4628–33, 2001.

95. Zheng, J. H., C. T. Chen, J. L. Au and M. G. Wientjes, "Time- and Concentration-Dependent Penetration of Doxorubicin in Prostate Tumors", *Aaps Pharmsci*, Vol. 3, No. 2, p. E15, 2001.

96. Saltzman, W., *Drug Delivery: Engineering Principles for Drug Therapy*, Topics in Chemical Engineering, Oxford University Press, 2001.

97. Jang, S. H., M. G. Wientjes, D. Lu and J. L. S. Au, "Drug Delivery and Transport to Solid Tumors", *Pharmaceutical Research*, Vol. 20, No. 9, pp. 1337–50, 2003.

98. Casciari, J. J., S. V. Sotirchos and R. M. Sutherland, "Glucose Diffusivity in Multicellular Tumor Spheroids", *Cancer Research*, Vol. 48, No. 14, pp. 3905–3909, 1988.

99. Chary, S. R., "Direct Measurement of Interstitial Convection and Diffusion of Albumin in Normal and Neoplastic Tissues by Fluorescence Photobleaching", *Proceedings of the National Academy of Sciences*, Vol. 86, No. 14, pp. 5385–5389, 1989.

100. Reddy, S. T., D. A. Berk, R. K. Jain and M. A. Swartz, "A Sensitive in Vivo Model for Quantifying Interstitial Convective Transport of Injected Macromolecules and Nanoparticles", *Journal of Applied Physiology (Bethesda, Md. : 1985)*, Vol. 101, No. 4, pp. 1162–9, 2006.

101. Margaris, K. N. and R. A. Black, "Modelling the Lymphatic System: Challenges and Opportunities", *Journal of the Royal Society*, Vol. 9, No. 69, pp. 601–12, 2012.

102. Zaugg-Vesti, B., J. Dörffler-Melly, M. Spiegel, S. Wen, U. K. Franzeck and A. Bollinger, "Lymphatic Capillary Pressure in Patients With Primary Lymphedema", *Microvascular Research*, Vol. 46, No. 2, pp. 128–134, 1993.

103. Spiegel, M., B. Vesti, A. Shore, U. K. Franzeck, F. Becker and A. Bollinger,

"Pressure of Lymphatic Capillaries in Human Skin", *The American Journal of Physiology*, Vol. 262, No. 4 Pt 2, pp. H1208–10, 1992.

104. Guyton, A. C., A. E. Taylor, R. E. Drake and J. C. Parker, "Dynamics of Subatmospheric Pressure in the Pulmonary Interstitial Fluid", *Ciba Foundation Symposium 38 - Lung Liquids*, pp. 77–100, John Wiley & Sons, Ltd., 2008.

105. Roose, T. and M. A. Swartz, "Multiscale Modeling of Lymphatic Drainage From Tissues Using Homogenization Theory", *Journal of Biomechanics*, Vol. 45, No. 1, pp. 107–15, 2012.

106. Vleugel, M. M., R. Bos, P. Van Der Groep, A. E. Greijer, A. Shvarts, H. V. Stel, E. Van Der Wall and P. J. Van Diest, "Lack of Lymphangiogenesis During Breast Carcinogenesis", *Journal of Clinical Pathology*, Vol. 57, No. 7, pp. 746–51, 2004.

107. Wu, M., H. B. Frieboes, S. R. Mcdougall, M. a. J. Chaplain, V. Cristini and J. Lowengrub, "The Effect of Interstitial Pressure on Tumor Growth: Coupling With the Blood and Lymphatic Vascular Systems", *Journal of Theoretical Biology*, Vol. 320, pp. 131–51, 2013.

108. Dickson, P. V., N. L. Hagedorn, J. B. Hamner, C. H. Fraga, C. Y. C. Ng, C. F. Stewart and A. M. Davidoff, "Interferon Beta-Mediated Vessel Stabilization Improves Delivery and Efficacy of Systemically Administered Topotecan in a Murine Neuroblastoma Model", *Journal of Pediatric Surgery*, Vol. 42, No. 1, pp. 160–5; Discussion 165, 2007.

109. Liu, J., S. Liao, Y. Huang, R. Samuel, T. Shi, K. Naxerova, P. Huang, W. Kamoun, R. K. Jain, D. Fukumura and L. Xu, "Pdgf-D Improves Drug Delivery and Efficacy Via Vascular Normalization, But Promotes Lymphatic Metastasis by Activating Cxcr4 in Breast Cancer", *Clinical Cancer Research*, Vol. 17, No. 11, pp. 3638–48, 2011.

110. Segers, J., V. Di Fazio, R. Ansiaux, P. Martinive, O. Feron, P. Wallemacq and

B. Gallez, "Potentiation of Cyclophosphamide Chemotherapy Using the Anti-Angiogenic Drug Thalidomide: Importance of Optimal Scheduling to Exploit the 'Normalization' Window of the Tumor Vasculature", *Cancer Letters*, Vol. 244, No. 1, pp. 129–35, 2006.

111. Teicher, B. A., N. P. Dupuis, M. F. Robinson, Y. Emi and D. A. Goff, "Antiangiogenic Treatment (Tnp-470/minocycline) Increases Tissue Levels of Anticancer Drugs in Mice Bearing Lewis Lung Carcinoma", *Oncology Research*, Vol. 7, No. 5, pp. 237–43, 1995.

112. Wildiers, H., G. Guetens, G. De Boeck, E. Verbeken, B. Landuyt, W. Landuyt, E. A. De Bruijn and A. T. Van Oosterom, "Effect of Antivascular Endothelial Growth Factor Treatment on the Intratumoral Uptake of Cpt-11", *British Journal of Cancer*, Vol. 88, No. 12, pp. 1979–86, 2003.

113. Zhou, Q. and J. M. Gallo, "Differential Effect of Sunitinib on the Distribution of Temozolomide in An Orthotopic Glioma Model", *Neuro-Oncology*, Vol. 11, No. 3, pp. 301–10, 2009.

114. Saltz, L. B., S. Clarke, E. Díaz-Rubio, W. Scheithauer, A. Figer, R. Wong, S. Koski, M. Lichinitser, T.-S. Yang, F. Rivera, F. Couture, F. Sirzén and J. Cassidy, "Bevacizumab in Combination With Oxaliplatin-Based Chemotherapy as First-Line Therapy in Metastatic Colorectal Cancer: a Randomized Phase Iii Study", *Journal of Clinical Oncology*, Vol. 26, No. 12, pp. 2013–9, 2008.

115. Hurwitz, H., L. Fehrenbacher, W. Novotny, T. Cartwright, J. Hainsworth, W. Heim, J. Berlin, A. Baron, S. Griffing, E. Holmgren, N. Ferrara, G. Fyfe, B. Rogers, R. Ross and F. Kabbinavar, "Bevacizumab Plus Irinotecan, Fluorouracil, and Leucovorin for Metastatic Colorectal Cancer", *The New England Journal of Medicine*, Vol. 350, No. 23, pp. 2335–42, 2004.

116. Tebbutt, N. C., K. Wilson, V. J. Gebski, M. M. Cummins, D. Zannino, G. A. Van Hazel, B. Robinson, A. Broad, V. Ganju, S. P. Ackland, G. Forgeson, D. Cun-

ningham, M. P. Saunders, M. R. Stockler, Y. Chua, J. R. Zalcberg, R. J. Simes and T. J. Price, "Capecitabine, Bevacizumab, and Mitomycin in First-Line Treatment of Metastatic Colorectal Cancer: Results of the Australasian Gastrointestinal Trials Group Randomized Phase Iii Max Study", *Journal of Clinical Oncology*, Vol. 28, No. 19, pp. 3191–8, 2010.

117. Reck, M., J. Von Pawel, P. Zatloukal, R. Ramlau, V. Gorbounova, V. Hirsh, N. Leighl, J. Mezger, V. Archer, N. Moore and C. Manegold, "Phase Iii Trial of Cisplatin Plus Gemcitabine With Either Placebo Or Bevacizumab as First-Line Therapy for Nonsquamous Non-Small-Cell Lung Cancer: Avail", *Journal of Clinical Oncology*, Vol. 27, No. 8, pp. 1227–34, 2009.

118. Sandler, A., R. Gray, M. C. Perry, J. Brahmer, J. H. Schiller, A. Dowlati, R. Lilenbaum and D. H. Johnson, "Paclitaxel-Carboplatin Alone Or With Bevacizumab for Non-Small-Cell Lung Cancer", *The New England Journal of Medicine*, Vol. 355, No. 24, pp. 2542–50, 2006.

119. Perren, T. J., A. M. Swart, J. Pfisterer, J. A. Ledermann, E. Pujade-Lauraine, G. Kristensen, M. S. Carey, P. Beale, A. Cervantes, C. Kurzeder, A. Du Bois, J. Sehouli, R. Kimmig, A. Stähle, F. Collinson, S. Essapen, C. Gourley, A. Lortholary, F. Selle, M. R. Mirza, A. Leminen, M. Plante, D. Stark, W. Qian, M. K. B. Parmar and A. M. Oza, "A Phase 3 Trial of Bevacizumab in Ovarian Cancer", *The New England Journal of Medicine*, Vol. 365, No. 26, pp. 2484–96, 2011.

120. Gray, R., S. Bhattacharya, C. Bowden, K. Miller and R. L. Comis, "Independent Review of E2100: a Phase Iii Trial of Bevacizumab Plus Paclitaxel Versus Paclitaxel in Women With Metastatic Breast Cancer", *Journal of Clinical Oncology*, Vol. 27, No. 30, pp. 4966–72, 2009.

121. Miles, D. W., A. Chan, L. Y. Dirix, J. Cortés, X. Pivot, P. Tomczak, T. Delozier, J. H. Sohn, L. Provencher, F. Puglisi, N. Harbeck, G. G. Steger, A. Schneeweiss, A. M. Wardley, A. Chlistalla and G. Romieu, "Phase Iii Study of Bevacizumab Plus Docetaxel Compared With Placebo Plus Docetaxel for the First-Line Treat-

ment of Human Epidermal Growth Factor Receptor 2-Negative Metastatic Breast Cancer", *Journal of Clinical Oncology*, Vol. 28, No. 20, pp. 3239–47, 2010.

122. Robert, N. J., V. Diéras, J. Glaspy, A. M. Brufsky, I. Bondarenko, O. N. Lipatov, E. A. Perez, D. A. Yardley, S. Y. T. Chan, X. Zhou, S.-C. Phan and J. O'shaughnessy, "Ribbon-1: Randomized, Double-Blind, Placebo-Controlled, Phase Iii Trial of Chemotherapy With Or Without Bevacizumab for First-Line Treatment of Human Epidermal Growth Factor Receptor 2-Negative, Locally Recurrent Or Metastatic Breast Cancer", *Journal of Clinical Oncology*, Vol. 29, No. 10, pp. 1252–60, 2011.

123. Liu, J., S. Liao, B. Diop-Frimpong, W. Chen, S. Goel, K. Naxerova, M. Ancukiewicz, Y. Boucher, R. K. Jain and L. Xu, "Tgf-β Blockade Improves the Distribution and Efficacy of Therapeutics in Breast Carcinoma by Normalizing the Tumor Stroma", *Proceedings of the National Academy of Sciences of the United States of America*, Vol. 109, No. 41, pp. 16618–23, 2012.

124. Huang, K., H. Ma, J. Liu, S. Huo, A. Kumar, T. Wei, X. Zhang, S. Jin, Y. Gan, P. C. Wang, S. He, X. Zhang and X.-J. Liang, "Size-Dependent Localization and Penetration of Ultrasmall Gold Nanoparticles in Cancer Cells, Multicellular Spheroids, and Tumors in Vivo", *Acs Nano*, Vol. 6, No. 5, pp. 4483–93, 2012.

125. Goh, Y. M., H. L. Kong and C. H. Wang, "Simulation of the Delivery of Doxorubicin to Hepatoma", *Pharmaceutical Research*, Vol. 18, No. 6, pp. 761–70, 2001.

126. Trédan, O., C. M. Galmarini, K. Patel and I. F. Tannock, "Drug Resistance and the Solid Tumor Microenvironment", *Journal of the National Cancer Institute*, Vol. 99, No. 19, pp. 1441–54, 2007.

127. Curry, F. E., "Mechanics and Thermodynamics of Transcapillary Exchange", E. M. Renkin and C. C. Michel (Editors), *Handbook of Physiology*, pp. 309–374, American Physiological Society, Bethesda, MD, 1984.

128. Laginha, K. M., S. Verwoert, G. J. R. Charrois and T. M. Allen, "Determination of Doxorubicin Levels in Whole Tumor and Tumor Nuclei in Murine Breast Cancer Tumors", *Clinical Cancer Research*, Vol. 11, No. 19 Pt 1, pp. 6944–9, 2005.

129. Gabizon, A., R. Catane, B. Uziely, B. Kaufman, T. Safra, R. Cohen, F. Martin, A. Huang and Y. Barenholz, "Prolonged Circulation Time and Enhanced Accumulation in Malignant Exudates of Doxorubicin Encapsulated in Polyethylene-Glycol Coated Liposomes", *Cancer Research*, Vol. 54, No. 4, pp. 987–92, 1994.

130. Batchelor, T. T., a. G. Sorensen, E. Di Tomaso, W.-T. Zhang, D. G. Duda, K. S. Cohen, K. R. Kozak, D. P. Cahill, P.-J. Chen, M. Zhu, M. Ancukiewicz, M. M. Mrugala, S. Plotkin, J. Drappatz, D. N. Louis, P. Ivy, D. T. Scadden, T. Benner, J. S. Loeffler, P. Y. Wen and R. K. Jain, "Azd2171, a Pan-Vegf Receptor Tyrosine Kinase Inhibitor, Normalizes Tumor Vasculature and Alleviates Edema in Glioblastoma Patients", *Cancer Cell*, Vol. 11, No. 1, pp. 83–95, 2007.

131. Willett, C. G., Y. Boucher, E. Di Tomaso, D. G. Duda, L. L. Munn, R. T. Tong, D. C. Chung, D. V. Sahani, S. P. Kalva, S. V. Kozin, M. Mino, K. S. Cohen, D. T. Scadden, A. C. Hartford, A. J. Fischman, J. W. Clark, D. P. Ryan, A. X. Zhu, L. S. Blaszkowsky, H. X. Chen, P. C. Shellito, G. Y. Lauwers and R. K. Jain, "Direct Evidence That the Vegf-Specific Antibody Bevacizumab Has Antivascular Effects in Human Rectal Cancer", *Nature Medicine*, Vol. 10, No. 2, pp. 145–7, 2004.

132. Plotkin, S. R., A. O. Stemmer-Rachamimov, F. G. Barker, C. Halpin, T. P. Padera, A. Tyrrell, A. G. Sorensen, R. K. Jain and E. Di Tomaso, "Hearing Improvement After Bevacizumab in Patients With Neurofibromatosis Type 2", *The New England Journal of Medicine*, Vol. 361, No. 4, pp. 358–67, 2009.

133. Zhao, G., J. Wu, S. Xu, M. W. Collins, Q. Long, C. S. König, Y. Jiang, J. Wang and A. R. Padhani, "Numerical Simulation of Blood Flow and Interstitial Fluid Pressure in Solid Tumor Microcirculation Based on Tumor-Induced Angiogenesis", *Acta Mechanica Sinica*, Vol. 23, No. 5, pp. 477–483, 2007.

134. Heldin, C.-H., K. Rubin, K. Pietras and A. Ostman, "High Interstitial Fluid Pressure - An Obstacle in Cancer Therapy", *Nature Reviews. Cancer*, Vol. 4, No. 10, pp. 806–13, 2004.

135. Baish, J. W., P. A. Netti and R. K. Jain, "Transmural Coupling of Fluid Flow in Microcirculatory Network and Interstitium in Tumors", *Microvascular Research*, Vol. 53, No. 2, pp. 128–41, 1997.